THE EVOLUTION OF MODELED CORONAL MASS EJECTIONS IN THE LOWER CORONA: EFFECTS OF THE HEATING AND ACCELERATION OF THE SOLAR WIND

by

Rebekah Minnel Evans Frolov

A Dissertation
Submitted to the
Graduate Faculty
of
George Mason University
in Partial Fulfillment of
The Requirements for the Degree
of
Doctor of Philosophy
Physics

Committee:

Dr. Merav Opher, Dissertation Director

Dr. Maria Kuznetsova, Committee Member

Dr. Arthur Poland, Committee Member

Dr. Michael Summers, Committee Member

Dr. Angelos Vourlidas, Committee Member

Dr. Jie Zhang, Committee Member

Dr. Michael Summers, Department Chairperson

Dr. Timothy Born, Associate Dean for Academic and Student Affairs, College of Science

Dr. Vikas Chandhoke Dean, College of Science

Date: 7/28/11

Summer Semester 2011
George Mason University
Fairfax, VA

The Evolution of Modeled Coronal Mass Ejection in the Lower Corona: Effects of the Heating and Acceleration of the Solar Wind

A dissertation submitted in partial fulfillment of the requirements for the degree of Doctor of Philosophy at George Mason University

By

Rebekah Minnel Evans Frolov
Master of Science
George Mason University, 2008
Bachelor of Science
University of Delaware, 2006

Director: Dr. Merav Opher, Professor
Department of Physics and Astronomy

Summer Semester 2011
George Mason University
Fairfax, VA

Dedication

I dedicate this dissertation to us.

Acknowledgments

First, thanks to my advisor, Merav Opher, for introducing me to this facinating research that I absolutely love. Thanks for taking me by the hand at the beginning, and then pushing me to try on my own. Thanks for always having a million ideas for projects, and for declaring in almost every meeting: *We should write a paper on this!* Someday, we will publish our *Evans & Opher* or *Opher & Evans*.

I would like to thank my committee members for all of their support over the years, and their endless patience with me over the last few months. I have learned something different from each of you, and I am so much better for it.

There are so many people who have been a part of this journey with me. From professors, to classmates, to officemates, to collaborators, to friends - I appreciate you all so much. In no particular order, thank you to: Rona Oran, Cris Loesch, Aline Vidotto, Vera Jatenco-Pereira, Sukbum Hong, Joe Weingartner, Joe Lieb, Paul So, Christy Henderson, Oscar Olmedo, Devin Vega, Yong Liu, Elena Provornikova, Christina Prested, Christina Kay, Bart van der Holst, Chip Manchester, Kamen Kozarev, Karl Unruh, Margaret Williams, Devon Stewart and Kerrin Brinkman.

I want to thank my entire family for all of the support over the years. Thanks to my brother and sister for making me tough. To my mom, thanks for making me believe that I could do anything. You are an amazing woman and I am proud to be your daughter. To my dad, thanks for teaching me to love math and science. I wish that you could be here to share this with me.

Finally, I want to thank a person who started out as just a classmate in Quantum Mechanics II. My husband, thank you for everything. I am so happy that we were able to share this journey together.

Table of Contents

List of Tables

List of Figures

Abstract

THE EVOLUTION OF MODELED CORONAL MASS EJECTION IN THE LOWER CORONA: EFFECTS OF THE HEATING AND ACCELERATION OF THE SOLAR WIND

Rebekah Minnel Evans Frolov, PhD

George Mason University, 2011

Dissertation Director: Dr. Merav Opher

Coronal mass ejections (CMEs) and their associated shocks are major sources of space weather. In order to forecast their impact at Earth, it is crucial to accurately model their propagation in interplanetary space. The only tool capable of treating the large scales of CME evolution is global magnetohydrodynamics (MHD) modeling. However, this approach cannot resolve the small scales on which important processes occur (such as the acceleration of the solar wind and coronal heating). The solar wind solution depends on which method is utilized to mimic these processes. And because the evolution of a CME depends crucially on its interaction with the solar wind, the CME evolution will also be connected to the heating mechanisms and drivers utilized in an MHD model.

In the first part of the thesis, we show that the ad hoc approaches to coronal heating used in global MHD models leads to unphysical conditions for CME-driven shock formation in the lower corona (1-10 solar radii). We present this argument in two steps. First, we present a CME simulation in which the solar wind was accelerated and heated by reducing the value of the polytropic index (to less than the adiabatic value) in the lower corona.

As it is not well understood, we do not model the CME initiation process - we utilize an out-of-equilibrium Titov-Demoulin flux rope to begin the eruption. We analyze several aspects of the CME, such as its kinematics and energy evolution, the shock formation and evolution, the plasma flows in the CME-sheath and their connection to the CME magnetic field vector, and the plasma pile-up at the front of the CME. We find that some characteristics are inconsistent with the observed properties of CMEs, and we connect these to the ad hoc treatment of the solar wind heating. Second, we use data of CME shock-accelerated solar energetic particle events to constrain the profile of the Alfvén speed in the lower corona. We show that the Alfvén speed profile from global MHD models with ad hoc heating is not aligned with these observations, but that local (one dimensional) models with physically-motivated Alfvén wave dissipation as a heating mechanism were in agreement.

In the second part of the thesis, we study the resonant absorption of surface Alfvén waves (SAW), a process which heats the solar wind. It is driven by a transverse gradient in the local Alfvén speed (in relation to the magnetic field direction). In the solar corona, we expect this mechanism to occur at the boundaries of open and closed magnetic fields. We make the first estimation of SAW energy dissipation in the solar corona and find that it is comparable to the ad hoc heating a polytropic model at the boundary of open and closed magnetic fields and in subpolar open field regions. Next, we implemented the SAW damping mechanism into the new solar corona component of the Space Weather Modeling Framework, in which Alfvén wave energy transport is self-consistently coupled to the MHD equations. The model already included wave dissipation along open magnetic field lines, mimicking turbulence. We demonstrate that including SAW dissipation in the model improved agreement with observations of coronal temperature both near the Sun and in the inner heliosphere by comparing with data from Ulysses and the Solar Terrestrial Relations Observatory (STEREO). Also, the inclusion of SAW dissipation steepened the Alfvén speed profile in the lower corona, aligning the Alfvén profile better with observational constraints of shock formation.

In the final part of the thesis, we modeled a CME in this newly developed solar wind background, and studied the interaction between the CME and the wind. We generate the eruption with a flux rope. We constrain the parameters of the flux rope with data from the 13 May 2005 eruption, including H-alpha images of the pre-eruption magnetic field, coronagraph images of the CME's shape and velocity. Because the flux rope traveled faster than the local magnetosonic speed, it acted as a piston and drove a shock wave ahead of it. The CME-driven shock had a strong impact on the solar wind environment through which it propagates: it altered the wave energy by concentrating it in the sheath through advection, and also increasing its value through momentum transfer. This simulation demonstrated how Alfvén waves are focused into the sheaths of ICMEs. The wave energy is then dissipated at the shock due to SAW damping. The shock heating accounted for 10% of the total change in thermal energy of the CME. The resulting temperature distribution of the CME is more aligned with observations than from a CME modeled in a polytropic solar wind.

This thesis has improved our understanding of the interaction between a CME and the solar wind through which it propagates. Our picture of CME-evolution in the lower corona will be tested by future missions Solar Probe (which will sample this region directly) and the Solar Orbiter.

Chapter 1: Introduction

The goal of this thesis is to better understand the evolution of Coronal Mass Ejections (CMEs) in the lower corona (1-10 $R_\odot$). The formation and evolution of shocks, and the associated particle acceleration depends crucially on how the solar wind is characterized. We will study two solar wind models, one which uses an ad hoc heating method, and one which includes the effect of Alfvén wave energy. We study how a CME evolves in each of these models. We do not model the initiation of the CME, but use an out of equilibrium flux rope to launch the eruption. We use data from spacecraft such as Ulysses, STEREO and LASCO to constrain the free parameters in the models we use and to validate their solutions.

1.1 Motivation

Space weather is the study of the near Earth environment's response to phenomenon originating at the Sun, such as flares, coronal mass ejections, corotating interaction regions (CIRs), and the general conditions in the local interplanetary medium. CMEs and CIRs can interact with the Earth's magnetic field and drive geomagnetic storms. Observations indicate that CMEs can drive strong shocks low in the corona (below 3 $R_\odot$), which accelerate particles to high energies [Haggerty and Roelof, 2002, Tylka et al., 2005].

Understanding and predicting space weather events has become imperative due to society's dependence on technology. Energetic particles can damage satellites, disrupt radio communication and affect global satellite positioning. Geomagnetic storms can cause surging electric currents on the Earth's surface, which can corrode lines and blow out transformers: for example, a 6-hour blackout in Canada in March 1989 associated with a CME affected six million people. There are also dangers to passengers and crews on polar flights due to enhanced radiation doses. The need to estimate the exposure of astronauts to radiation outside the magnetosphere makes understanding these events crucial to manned space exploration. These issues make space weather a field of interest for NASA, the military, and the department of energy, to name a few.

1.2 The Sun

Although the Sun has been studied by astronomers for centuries, three important properties of the Sun and its atmosphere were discovered in the last eighty years. First, spectroscopic measurements deduced that the temperature of the solar atmosphere was over one million Kelvin (compared to 5800 K at the photosphere). Twenty years later, Biermann was studying comets and noticed that a gas part of the tail aways pointed away from the Sun, as if being pushed out by a stream of ionized particles [Biermann, 1951]. In 1958, Eugene Parker connected these two ideas and published a theoretical work predicting a flow of ionized gas in the solar system, termed the solar wind. By a simple consideration of an expanding, spherically symmetric, isothermal atmosphere (with no magnetic field), Parker derived the solution for a supersonic solar wind with a terminal velocity of 300 km/s [Parker, 1958]. The solar wind was first observed directly in 1959 by the Soviet satellite Luna 1. In Neugebauer and Snyder [1962], the first measurements by the United States from Mariner 2 were presented. In addition to the hot and expanding corona, the third recent discovery which changed the way we view the Sun was the Coronal Mass Ejection (CME), which will be discussed in the next section.

The typical properties of the solar wind observed near the Earth are shown in Table 1 [Gombosi, 1998]. The solar wind is bimodal, as shown in Figure 1.1 [McComas et al., 2000]. The radial distance in the plot gives the solar wind velocity: for all latitudes 30° or more away from the equator, a faster, relatively uniform plasma is present. Near the equator, a slower and less smooth wind is present (see the larger variations in the speed near the equator in Figure 1.1). The streamer regions (and slow solar wind) is denser than the fast

Table 1.1: Average near-Earth Solar Wind Properties [Gombosi, 1998]

Quantity	Value
Flow Speed	450 km/s
Proton Temperature	0.12 MK
Electron Temperature	0.14 MK
Magnetic Field Strength	7 nT
Collisional time	40.5 days
Travel time to 1 AU	4 days

solar wind.

In the Parker solar wind solution, the solar wind speed begins as a subsonic flow, but accelerates until it becomes supersonic [Parker, 1958]. It then reaches terminal velocity as it propagates through interplanetary space. At a contact discontinuity called the heliopause, the solar wind meets another type of wind: the interstellar wind. Before arriving at the heliopause, the supersonic solar wind must decelerate and pass through a shock called the termination shock. The Voyager spacecraft have both passed the termination shock, although not at the same time [Stone et al., 2005, 2008]. Since then, the Voyager spacecraft are traveling towards the heliopause. Recently, the radial component of the solar wind flow measured by Voyager I has become very weak, which indicates that the heliopause is nearby [Stone, 2010].

The Sun's magnetic field structure varies on a cycle, in which it goes from an organized dipole-like field to a field with higher order terms. In the time of minimum activity, the magnetic field structure is closed around the equator, forming streamer structures, as seen in Figure 1.1. Above the streamers, the two magnetic field polarities are separated by the heliospheric current sheet (HCS). Since the Sun rotates, the structure of the extended HCS takes the shape of a ballerina skirt. Another result of solar rotation is the formation of CIRs. These form when high speed solar wind streams are located at a latitude near a slow stream. The fast stream can catch up, compressing the plasma in the slower stream and enhancing magnetic fields. CIRs can be geoeffective because they contain enhanced magnetic field regions.

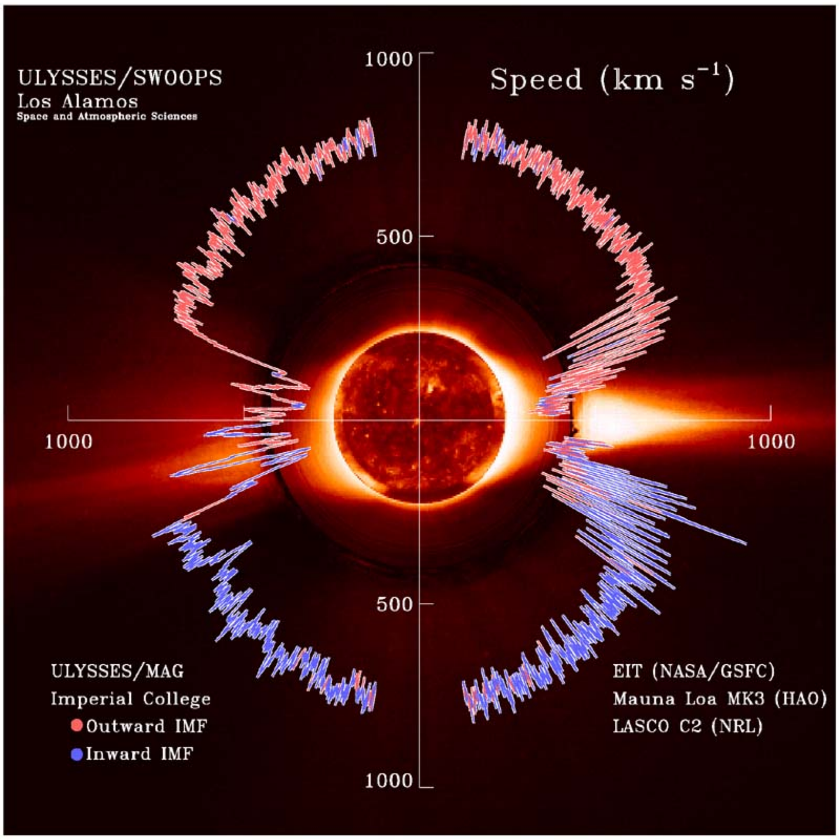

Figure 1.1: The solar wind speed is plotted as a function of latitude during the first *Ulysses* fast latitude scan (1996). The colors indicate the radial direction of the magnetic field at that location (red being radially outward and blue being inward). See text for more details. [McComas et al., 2000]

1.3 Coronal Heating and Solar Wind Acceleration

It is known from observations that the acceleration of the solar wind occurs predominantly within a few solar radii of the surface [Grall et al., 1996, Hartmann and MacGregor, 1980]. Additionally, Solar and Heliospheric Observatory (SOHO) observations have shown that ions are heated below 4 $R_{\odot}$ [Esser et al., 1999, Kohl et al., 1998]. Grall et al. [1996] suggested that because the locations for the heating of the corona and the acceleration of the solar wind are the same, it is possible that the same mechanism could contribute to both.

The first MHD solar wind simulation to include open and closed magnetic fields was done by Pneuman and Kopp [1971]. Thermal heating alone is not sufficient to bring models into agreement with observations of the lower corona and at Earth [Usmanov and Goldstein, 2003]. If one uses ideal MHD without some sort of additional momentum, the ratio of the density of the solar wind at the Earth to the coronal density is too high. As a result, when one matches the density at either the inner boundary or near Earth to observations, the density at the other boundary will be innaccurate. To solve this problem and produce a fast wind of relatively low density while preserving agreement with the plasma density observed at the coronal base, an additional source of momentum must be incorporated into the models. Some ad hoc approaches to achieving coronal heating and wind acceleration include: 1) utilizing an empirical heating function or non-uniform polytropic index distribution [Cohen et al., 2007, Groth et al., 2000, Mikić et al., 1999, Roussev et al., 2003]; 2) including Alfvén wave energy without damping [Lionello et al., 2009]; and 3) including Alfvén wave energy with an empirical damping length [Ofman, 2004, Usmanov and Goldstein, 2006]. These models are benchmarked with observations in the inner heliosphere (for example with *Ulysses* or *ACE*).

However, we would like to understand the physical processes responsible for coronal heating and solar wind acceleration. The proposed sources are numerous, but can generally be divided into two categories. The first is the fast solar wind, which originates from open coronal holes [Hassler et al., 1999]. The Alfvén wave pressure gradient has been suggested as a force to explain the acceleration of the fast solar wind upwards of 700 km/s. These same waves can heat the corona through wave dissipation [Belcher, 1971, Parker, 1965]. The second category is the slow solar wind, thought to originate in streamer cusps and the boundary of streamers and active regions [Brooks and Warren, 2011, Edmondson, 2011]. Magnetic reconnection in nanoflares [Klimchuk, 2006, Parker, 1988] could play a dominant role in the heating of the slow solar wind. Additionally, the dissipation of Alfvén waves could also be a source of heating along closed loops [Ionson, 1978, Rappazzo et al., 2007].

The theory of Alfvén wave dissipation is supported by observationals which support the presence of waves both close to the Sun and in the heliosphere. Alfvén waves have been

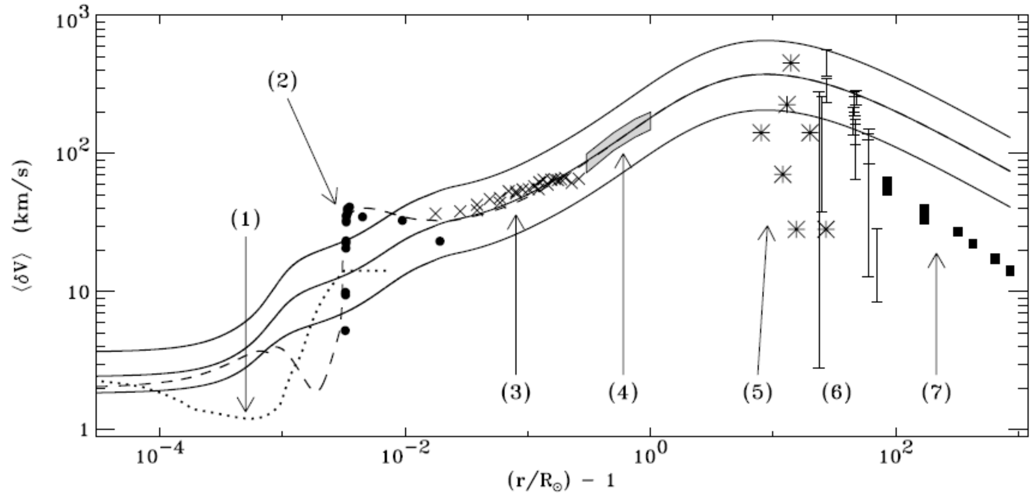

Figure 1.2: Frequency-integrated velocity fluctuations derived from modeling and in situ data (see text for details) [Cranmer and van Ballegooijen, 2005].

detected in the lower layers of the solar atmosphere using both ground-based observations [Jess et al., 2009] and the Hinode spacecraft [Cirtain et al., 2007, De Pontieu et al., 2007, Okamoto et al., 2007] with periods 2-4 minutes ($4.2 - 8.3 \times 10^{-3}$ Hz). Ground based observations indicate the presence of Alfvén waves in the corona with periods of five minutes (3.3×10^{-3} Hz) [Tomczyk and McIntosh, 2009, Tomczyk et al., 2007]. At 1 AU, the dominant wave power is in waves with periods of 1-3 hours (9.2×10^{-5} to 2.8×10^{-4} Hz) [Belcher and Davis, 1971], suggesting that higher frequencies have been dissipated.

The first efforts to include the effects of Alfvén wave energy in global MHD models was done in the low frequency, short wavelength approximation (WKB). In these models, a particular damping mechanism was not specified. Usmanov and Goldstein [2006] and Ofman and Davila [1998] chose the dissipation length to benchmark with Ulysses and Helios data. Other works included the wave energy and momentum without damping [Lionello et al., 2009], who matched SOHO Extreme Ultraviolet and Yohkoh soft X-ray observations. Local (one-dimensional) models such as Cranmer and van Ballegooijen [2005], Cranmer et al.

[2007], Verdini and Velli [2007] can model the nonlinear interaction of ingoing and outgoing waves in the Elssaser variable formalism. In Figure 1.2, the theoretically predicted frequency-integrated velocity amplitude is shown as a function of height, with observational data overlapped [Cranmer and van Ballegooijen, 2005]: (1) The dotted line shows a best-fit height dependence for the microturbulence needed to match photospheric and chromospheric line widths in the semiempirical models; (2) The filled circles show nonthermal linebroadening velocities measured (on the solar disk) in the transition region and low corona by the SUMER (Solar Ultraviolet Measurements of Emitted Radiation) instrument on SOHO; (3) The crosses show nonthermal velocities inferred by SUMER measurements made above the solar limb; (4) The gray region shows lower and upper limits on the nonthermal velocity as computed from off-limb measurements made by the UVCS (Ultraviolet Coronagraph Spectrometer) instrument on SOHO; (5) The stars show early measurements of the random wavelike component of the solar wind velocity from interplanetary scintillation observations of radio signals passing through the corona; (6) The error bars show amore recent determination of velocity fluctuationsspecifically transverse to the radial direction from radio scintillations in the fast solar wind; and (7) The Helios and Ulysses probes measured time-averaged Elsasser amplitudes that were converted to a representative velocity amplitude. The data are lower than the simulation results, which the authors explain with wave dissipation in the corona and heliosphere. Figure 1.2 is an example of the complex calculations that can be done with local models. However, the Cranmer and van Ballegooijen [2005] simulation assumed the magnetic field and density of the solar wind a priori (unlike the global MHD models). There is a lack of connecting a physically motivated damping mechanism (seen in 1D models) to the self-consistent solution of the plasma quantities (which result from a global MHD wave-driven model).

The possible damping mechanisms for Alfvén waves from the photosphere to lower corona are numerous and include nonlinear damping [Wentzel, 1989], turbulent cascade [Hollweg, 1986, Matthaeus et al., 1999], phase mixing [Heyvaerts and Priest, 1983, Parker, 1991], Landau damping [Hollweg, 1971], neutral collisional [De Pontieu et al., 2001, Leake

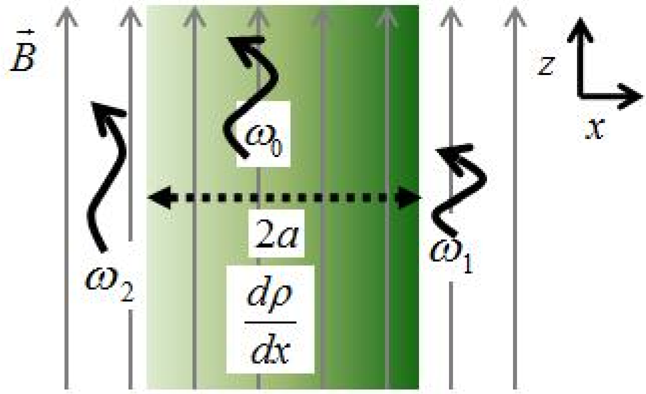

Figure 1.3: Schematic of the generation and dissipation of surface Alfvén wave by resonant absorption [Evans et al., 2011b].

et al., 2005], ion-cyclotron damping [Isenberg et al., 2001], and surface Alfvén wave damping [Ionson, 1978]. In the chromosphere, Alfvén waves with frequencies above 0.6 Hz are damped by ion-neutral collisional damping while frequencies below 10^{-2} Hz were unaffected [Cranmer and van Ballegooijen, 2005, De Pontieu et al., 2001, Leake et al., 2005]. Cranmer and van Ballegooijen [2005] found that nonlinear damping occurred over the extended corona. Verdini and Velli [2007] found that waves with frequencies $10^{-6} - 10^{-4}$ Hz were reflected by a gradient in the background Alfvén profile, and that they dissipated not in the lower layers of the solar atmosphere, but over a distance of a few solar radii. In the corona, the ion-cyclotron frequency is 10^{4-6} Hz, so cyclotron resonance damping is not relevant for low frequency waves. Therefore, of the numerous possible mechanisms for damping Alfvén waves, we expect that nonlinear turbulent damping, phase mixing, surface Alfvén wave damping to be important for low frequency waves.

Surface Alfvén waves form on a magnetic interface - a finite thickness boundary separating two regions of plasma with a strong inhomogeneity in magnetic field and/or density. Consider a region of plasma in which a gradient in the local Alfvén speed exists which is perpendicular to the direction of the magnetic field. We provide a schematic of this scenario in Fig. 1.3. The magnetic field is in the Z direction, and the density varies linearly in the

X direction over a distance a. Two Alfvén waves (with frequencies ω_1 and ω_2; assumed to be launched by convective motions shaking the footpoints of the magnetic field) traveling in regions 1 and 2 will give rise to a surface mode wave (with frequency ω_0). This wave can then dissipate in a resonant layer. The damping can be categorized as strong if $ka << 1$ (k is the wavenumber). Ionson [1978] first utilized surface Alfvén waves and resonant absorption as a mechanism to heat coronal loops. The transfer of MHD wave energy by resonant absorption was also studied in Hollweg [1987] and Wentzel [1979]. An alternative dissipation mechanism for surface Alfvén waves is nonlinear wave steepening [Ruderman, 1992]. These and other efforts, e.g. [Lee and Roberts, 1986] have resulted in damping lengths which depend on the frequency of the waves, the nature of the magnetic interface, and the local plasma parameters (density, magnetic field and velocity).

Utilizing these relations, the profile of the damping length in the wind has been estimated [Jatenco-Pereira and Opher, 1989, Narain and Sharma, 1998]. All previous studies made assumptions about the wind. For example, [Narain and Sharma, 1998] calculated nonlinear viscous damping of surface Alfvén waves in polar coronal holes. They assumed two values of the superradial expansion of the magnetic field lines, profiles for density (based on observations), and a single frequency (0.01 Hz). They obtained one profile, and concluded that the nonlinear damping of the surface Alfvén waves in regions of strong magnetic field expansion should contribute significantly to the heating in the solar wind. Using a combination of three damping mechanisms (nonlinear damping, surface Alfvén wave damping, and phase mixing), Jatenco-Pereira and Opher [1989] were able to match observations of mass loss rates and terminal velocities for cool, giant stars. They applied their model to the Sun and were able to obtain coronal heating and to match wind velocity and Alfvén wave power density observations with a 1D simulation [Jatenco-Pereira et al., 1994].

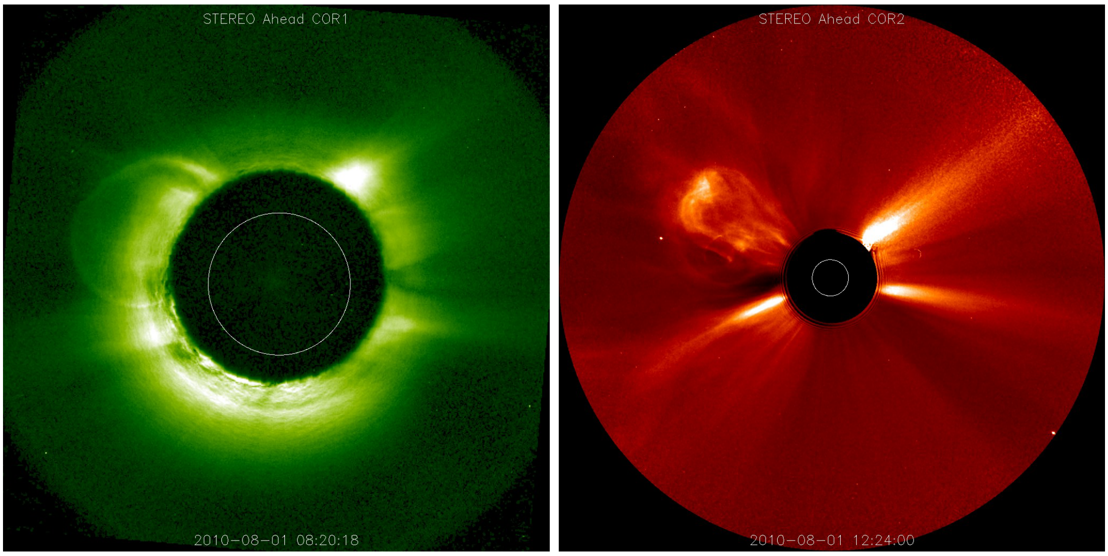

Figure 1.4: Images of the 2010 August 1 Coronal Mass Ejection by STEREO SECCHI in the low (left) and high (right) corona.

1.4 Coronal Mass Ejections

A CME is a large-scale release of plasma and magnetic field with energy on the order 10^{32} ergs. Since the first observations [Gosling et al., 1974], CMEs have been extensively studied with ground and space based instruments. The result is a rich variety of data sets spanning several solar cycles, such as white light imaging, X-ray imaging, H-alpha imaging, spectral data, radio wave data, interplanetary scintillation, and in situ plasma sampling. These different types of observations can be combined to get the most global picture of the CME's evolution. Fig. 1.4 shows a CME in the lower corona, as imaged in white light by the Solar Terrestrial Relations Observatory (STEREO)'s Sun Earth Connection Coronal and Heliospheric Investigation (SECCHI) low in the corona (in COR1) and higher in the corona (COR2).

In white light imaging, CMEs often show a three-part structure: a bright front, dark cavity and bright, dense core. The mass of the ejection has been estimated using coronagraph images of Thompson-scattered white light [Colaninno and Vourlidas, 2009, Vourlidas et al., 2010]. The masses obtained close to the Sun compared to masses estimated in interplanetary space can vary by an order of magnitude or more for the same event [Bisi et al., 2010a]. Typical values are in the range of 10^{14-16} grams. The speeds range from 100-3,000 km/s and the main acceleration phase seems to occur very close to the Sun (typically a few hundred m/s^2) [Yashiro et al., 2004, Zhang and Dere, 2006]. For events associated with a flare, the CME acceleration profile has been well correlated with the flare soft X-ray flux profile [Zhang and Dere, 2006]. CMEs which erupt with fast speeds slow down during propagation to 1 AU, due to some drag force [Poomvises et al., 2010]. In the heliosphere, CMEs propagate with nearly constant speed, except when they interact with each other [Lugaz et al., 2005], or with structures (such as coronal holes) in the solar wind [Byrne et al., 2010, Lugaz et al., 2011]. An effort to characterize CME velocity evolution during propagation from Sun to Earth concluded that the initial CME velocity is a crucial factor in determining its velocity at 1 AU [Case et al., 2008, Gopalswamy et al., 2000]. Therefore, it can be said that the two factors which most determine the evolution of a CME are the initial conditions of the eruption, and the characteristics of the solar wind through which it propagates.

If the speed of a CME exceeds the local magnetosonic speed, it can act as a piston and drive a shock wave. Observations indicate that CMEs can drive shocks at distances from the low corona (heights of 1-3 $R_\odot$) to 1 AU and beyond. The shocks accelerate electrons, which excite radio waves that are observed at Earth (type II radio burst, [Cliver et al., 1999, Gopalswamy and Kaiser, 2002]). These shocks can also accelerate particles to GeV/nucleon energies in ground based events [Tylka et al., 2003], and produce radiation which is hazardous to astronauts. The first CME shock wave directly observed in coronagraph images was also shown to interact with coronal streamers [Vourlidas et al., 2003]. Later, Ontiveros and Vourlidas [2009] tracked CME-driven shocks in white light LASCO images, and estimated that fast CMEs ($v > 1,500 km/s$) were driving relatively weak shocks (density compression ratios of 1.2-2.8 for heights less than 10 $R_\odot$) [1]. In the very low corona

[1]However, in interplanetary space, fast ICMEs can produce interplanetary shocks [Sheeley et al., 1985],

(below 2 $R_\odot$) [Kozarev et al., 2011] analyzed two shock waves with AIA data and estimated a lower limit of the shock compression ratio of 1.12-1.18.

Besides radio emission and white light imaging, spectroscopy has also been used to constrain the properties of CMEs in the lower corona. The UVCS ultraviolet coronagraph spectrometer on SOHO has been used to study CMEs and their shock waves. For example, Lee et al. [2009] studied the 2001 December 13 CME event and found that the CME must be heated after eruption as it propagates in order to obtain a match between the temperature extracted from the UVCS data and a modeled flux rope. They found that 75 % of the flux rope's magnetic energy must be dissipated and converted to heat to match the observations. Also, Landi et al. [2010] constrained the thermal energy to be larger than the kinetic energy of a CME in the first few solar radii of propagation. In this thesis, we will show that the dissipation of Alfvén waves in the solar wind can supply this heating as well.

Even with the large amount of data covering CMEs, there are still many unanswered questions about CME initation. Forbes [2000] estimated the available energy sources in a CME eruption, and determined that kinetic, thermal and gravitational energy were orders of magnitude smaller than the available free magnetic energy in the coronal field. The magnetic energy must be the source of the eruption; however how it is released is still debated. Several analytic CME eruption models have been proposed [Antiochos et al., 1999, Chen, 1989, Titov and Démoulin, 1999]. Some begin with a flux rope (a tube of twisted magnetic field), while others produce a flux rope during liftoff. The main differences between the models are the geometry of the magnetic field and the liftoff-trigger (such as reconnection, magnetic flux emergence, or torus instability). Fang et al. [2010] has simulated emerging flux from below the photosphere as a first effort in a self-consistent eruption.

The first model of a disturbance from the Sun to 1 AU was calculated in a one-dimension hydrodynamics code [Hundhausen and Gentry, 1969]. The initiation process can be circumvented by driving eruptions by imposing unstable initial conditions. Increasingly complex simulations in two and three-dimensions have been developed, for example Dryer et al.

which can drive space weather events when they interact with the Earth's magnetosphere.

[1979], Linker et al. [2003], Lynch et al. [2004, 2008], Manchester et al. [2004], Roussev et al. [2003b]. These simulations have aided in the interpretation of observational data such as coronagraph images, especially when there is a complex eruption [Lugaz et al., 2008, Manchester et al., 2008]. The rotation [Cohen et al., 2010, Evans et al., 2011a, Lynch et al., 2009] and deflection [Lugaz et al., 2011] of CMEs in the lower corona has been studied. Analysis of the modeled shock and sheath structures has also shed light on shock acceleration in the lower corona Das et al. [2011], Manchester et al. [2005]. As discussed earlier, the background solar wind through which these modeled CMEs are propagating employ ad hoc coronal heating methods [Cohen et al., 2007, Groth et al., 2000, Mikić et al., 1999, Roussev et al., 2003]. As steady state, solar wind models, they compare favorably with in situ solar wind data from Ulysses, Yohkoh, Helios and Advanced Composition Explorer data. However, there is an important question which has not been seriously raised: how does the physics (or lack thereof) in the treatment of the solar wind affect the evolution of a modeled CME? This thesis explores this issue by studying CME evolution in two solar wind models.

1.5 Organization of Thesis

This thesis aims to study the heating and acceleration of the solar wind and its effect on the evolution of a CME. We begin with the modeling of a CME in a polytropic solar wind background. We introduce the numerical tools used throughout the thesis. We study several aspects of CME evolution, such as: the role of the ejecta magnetic field on the evolution of a CME and CME-driven shocks in the lower corona [Evans et al., 2011a], the piling up of sheath material in front of the ejecta [Das et al., 2011], and the thermal interaction between the CME and the solar wind [Loesch et al., 2011]. Next, we survey the solar wind from several MHD models [Evans et al., 2008]. We compare the Alfvén speed profile resulting from each model. We focus on the implications for shock formation in the lower corona. From this work, we conclude that wave-driven modeling with physical dissipation mechanisms was required to comply with observational constraints. Next, we focus on one such mechanism, the dissipation of surface Alfvén waves (SAWs), which is driven by transverse gradients in density. We first estimate the impact of SAW damping in the solar corona, and find that it could be a dominant mechanism at the boundary of open and closed magnetic field lines [Evans et al., 2009]. Next, we implement SAW damping in a wave-driven solar wind model, and found that it improves the model's agreement with temperature observations both near the Sun and in the heliosphere. In the final chapter, we simulate a CME in this wave-driven background, and show that the solution is dramatically improved over the CME simulation presented in the beginning of the thesis.

Chapter 2: Evolution of a CME in a Polytropic Solar Wind

2.1 Introduction

In this chapter we present simulations of coronal mass ejections (CMEs) in a solar wind background which heats the corona and accelerates the solar wind by reducing the polytropic index value near the Sun below the adiabatic value. We first present a description of the numerical tool, and then provide the details of the polytropic model. Next, we describe the flux rope model used in this chapter and Chapter 5 to drive the eruption. Then, we present the results of three works [Das et al., 2011, Evans et al., 2011a, Loesch et al., 2011] in which we studied different aspects of CME evolution.

2.2 Description of Tool

We model the solar environment with the Space Weather Modeling Framework (SWMF) [Toth et al., 2011]. This 3D global magnetohydrodynamics (MHD) model has the Block Adaptive Tree Solar-Wind Roe-Type Upwind Scheme (BATS-R-US) at its core to solve the ideal MHD equations. The code is massively parallel and includes adaptive mesh refinement. This makes it ideal to study the problems of space physics, in which the temporal and spatial scales can vary by tens of orders of magnitude. A specific region of the simulation can be focused on with high resolution, while the rest of the grid remains coarse, and the refinement can be adapted as the simulation runs.

The grid structure of BATS-R-US can be selected as Cartesian (as used in this thesis) or generalized coordinates, and is broken into blocks. Each block contains $n_x \times n_y \times n_z$ number of grid cells. In this thesis, each block contains $4^3 = 64$ cells. Each block is surrounded by ghost cells (usually $n_g = 2$, which act to pass the physical quantities and other information

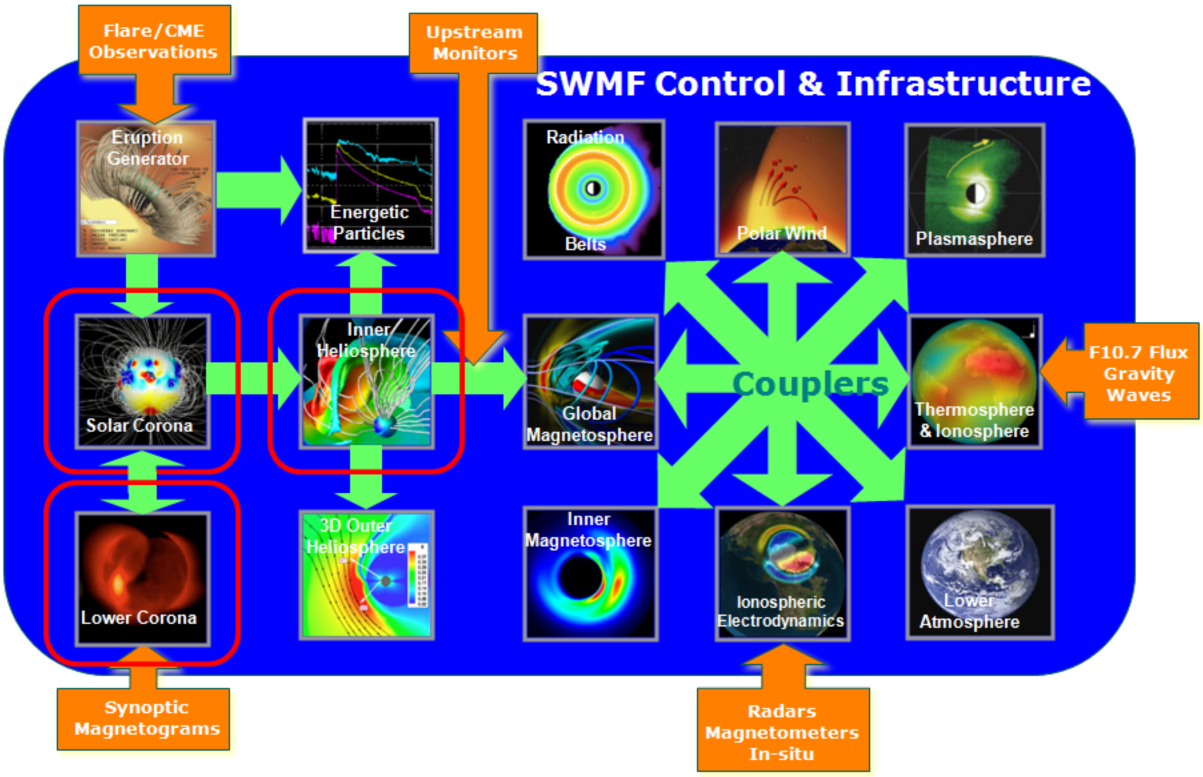

Figure 2.1: The components and coupling within the Space Weather Modeling Framework [Toth et al., 2011].

between blocks. Refinement of grid cells is performed by refining (or coarsening) each cell in a block by a factor of two. Therefore, when a region is refined by just one level, the number of cells in the region increases by a factor of eight. There are several numerical schemes in BATS-R-US, each of which is useful for a specific problem: explicit time stepping with fixed or local time steps, partially steady-state evolution, point-implicit, semi-implicit, explicit/implicit, and fully implicit numerical schemes. In local time stepping, all temporal derivatives are ignored in the differential equations. For example, when running a steady-state solar wind solution, the explicit local time steps allows for fast convergence to steady state solution (less than two hours of walltime on NASA Ames supercomputer).

The framework has different components to model different regions of the solar system: Lower Corona (LC), Solar Corona (SC), Inner Heliosphere (IH), Outer Heliosphere (OH), Global Magnetosphere (GM), Earth's Ionosphere (IE), and more - see Figure 2.1. Each component can have multiple versions, and some models are physics-based while others are empirical. The components are compiled into libraries, which all link back to the framework core. The user compiles the framework with his or her specific user file, and a single executable is produced. This executable can be run on supercomputer platforms such as NASA Ames Pleiades and Columbia (as used in this simulation), and others [Toth et al., 2011]. Different groups of blocks are distributed over the processors, and communication between processors occurs over the Message Passing Interface (MPI).

Each component can be run separately to study a local problem, and can also be coupled together through inner and outer boundary conditions to study large-scale problems in space physics. For example, the propagation of a CME to Earth can now be achieved by coupling the LC to the SC to the IH component. The SC model and its coupling to the IH component has been successfully benchmarked with Advanced Composition Explorer (ACE) data at 1 AU for many Carrington Rotations (CR) for two different approaches to coronal heating: the polytropic model, to be described in the next section [Cohen et al., 2008], and the wave-driven model, presented in Chapter 4 [van der Holst et al., 2010].

In each component model, the physics of the problem is cast into the form:

$$\frac{d\mathbf{U}}{dt} + \nabla \cdot \mathbf{F}\left(\mathbf{U}\right) = \mathbf{S}, \tag{2.1}$$

where $\mathbf{U}$ is a vector of state variables, $\mathbf{F}$ is the flux vector, and $\mathbf{S}$ represents source terms that are not a part of a conservative form equation. [1].

2.3 Polytropic Solar Wind Model

In this solar corona model, the solar wind is treated as a single conducting fluid. The ideal MHD equations are solved in the following conservative form (neglecting gravity):

[1] The dissipation of surface Alfvén waves will be treated as a source term

$$\frac{\partial \rho}{\partial t} + \nabla \cdot (\rho \mathbf{u}) = 0, \tag{2.2}$$

$$\frac{\partial (\rho \mathbf{u})}{\partial t} + \nabla \cdot \left(\rho \mathbf{u}\mathbf{u} - \frac{\mathbf{B}\mathbf{B}}{4\pi} + \left(p + \frac{B^2}{8\pi} \right) \mathbf{I} \right) = 0, \tag{2.3}$$

$$\frac{\partial \mathbf{B}}{\partial t} + \nabla \cdot (\mathbf{u}\mathbf{B} - \mathbf{B}\mathbf{u}) = 0 \tag{2.4}$$

$$\nabla \cdot \left[\mathbf{u} \left(\frac{\Gamma p}{\Gamma - 1} + \frac{\rho u^2}{2} + \frac{B^2}{4\pi} \right) - \frac{(\mathbf{u} \cdot \mathbf{B}) \mathbf{B}}{4\pi} \right] = 0. \tag{2.5}$$

The coronal heating is modeled by a spatially varying polytropic index Γ, seen in the MHD energy equation [Cohen et al., 2007, Roussev et al., 2003]. The initial distribution on the inner boundary (as a function of latitude and longitude) is obtained with the conservation of energy along an open field line,

$$\frac{u_{WSA}^2}{2} = \frac{\Gamma_0}{\Gamma_0 - 1} \frac{p_0}{\rho_0} - \frac{GM_\odot}{R_\odot} \tag{2.6}$$

where u_{WSA} is the solar wind speed at 1 AU, generated with the empirical model of Wang-Sheeley-Arge (WSA; in which the speed is derived from expansion of magnetic field lines using the photospheric magnetic field and the PFSS model [Altschuler and Newkirk, 1969]). A value is applied to closed field regions. Figure 2.2 shows the distribution of Γ in the plane of the sky on 1996 August 17. The inner boundary condition for the radial magnetic field was taken from a synoptic magnetogram, corresponding to Carrington Rotation (CR) 1912. Other free parameters of the model include the temperature and density on the inner boundary (1.0 $R_\odot$. A typical steady state solar wind can be achieved in 12,000 to 24,000 iterations using local time stepping.

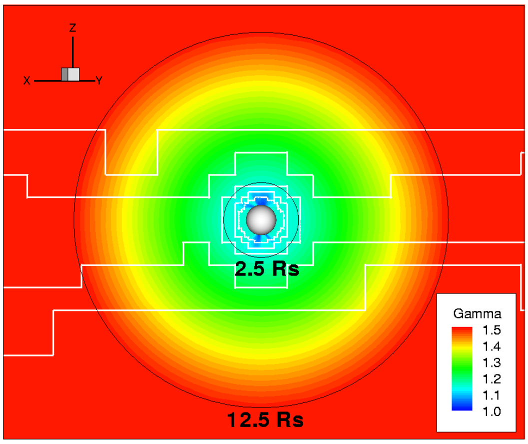

Figure 2.2: The distribution of Γ, the effective polytropic index, in the plane of the sky on 1996 August 17. Γ is specified on the solar surface (shown as white sphere) using the Bernoulli integral, and is interpolated to 1.1 at 2.5 $R_\odot$ (inner black circle). Above 2.5 $R_\odot$, Γ varies linearly until 12.5 $R_\odot$ (outer black circle), above which it has the value 1.5. The white lines show the boundaries of grid refinement. [Evans et al., 2009].

In this chapter, a background solar wind is set up for May 1997 (solar minimum). The photospheric value of the line of sight magnetic field, calculated from the Zeeman effect with the Michelson Doppler Imager magnetogram data is used an as inner boundary condition for the radial component of the magnetic field. Next, the initial conditions for the magnetic field are constructed with the the Potential Field Source Surface (PFSS) model [Altschuler and Newkirk, 1969], which assumes zero current below some radius (here set to 2.5 $R_\odot$) and purely radial field above. The field inside the potential surface is the solution to the Laplace equation, which can be expanded as a series of spherical harmonics.

2.4 Modeling a CME as a Flux Rope

As discussed in the Introduction, the initiation mechanism for CMEs is not well understood. Several analytic CME initiation solutions have been proposed (e.g. Antiochos et al. [1999], Chen [1989], Dryer et al. [1979], Gibson and Low [1998], Titov and Démoulin [1999]). Some of these have been incorporated into numerical models of CME propagation (e.g. Linker et al. [2003], Lynch et al. [2004], Manchester et al. [2004], Roussev et al. [2003b]). The main differences between the models are the geometry of the magnetic field and the physics of the trigger mechanism, such as reconnection, flux emergence, and shear flows [Forbes et al., 2006]. This thesis will not attempt to validate any initiation mechanism, or model the initiation process. Instead we use a modified Titov-Demoulin (TD) flux rope [Roussev et al., 2003b] as a tool to study CME propagation in the lower corona (see Appendix A).

One goal of this chapter is to understand the role of the CME magnetic field and the evolution of the ejection. Therefore, we set up three orientations of the flux rope fields and run three simulations. Cartoons showing the respective magnetic field orientations between the ejecta field, active region field, and global coronal field can be see in Figure 2.3a-c, and in Figure 2.3d, we show the simulation set up. The flux rope configuration in panel b was used in the works of Das et al. [2011] and Loesch et al. [2011].

The TD flux ropes are inserted out of equilibrium into NOAA AR8038. This active region was the source region for the 1997 May 12 CME, which was Earth-directed [Thompson et al., 1998]. As we have configured the TD flux rope, including only the torus line current I, the ejecta field is poloidal. A small axial component is due to the superposition of the poloidal field with the overlying active region arcade (see Figure 2.3d). The parameters of the flux rope model are: a torus radius of 0.14 $R_\odot$, cross section radius 0.03 $R_\odot$, mass 4.5 $\times$ 10^{12} g, and torus line current 5 $\times$ 10^{11} A (no subphotospheric magnetic charges or line current are included).

We set initial magnetic field orientations of the TD flux ropes by changing the location and direction of the torus line current. The cases can be identified by the quantity β, which we have defined to be the angle between the poloidal field (B_{ejecta}) and the coronal field (B_{cor}). The global coronal field is in -Z axis, the Active Region (AR) field is in +Y axis, ICME propagation is in +X axis. The angle β for Case A is 90°, for Case B is 180° and for Case C is 0° (Figure 2.3(a)-(c)). We define another angle γ measured between B_{ejecta} and the active region field B_{ar}, which is 180° for Case A, -90° for Case B and 90° for Case C. All three CMEs contain the same initial free energy (2 $\times$ 10^{32} ergs).

After the steady-state solution is achieved, a high resolution box containing cells of size

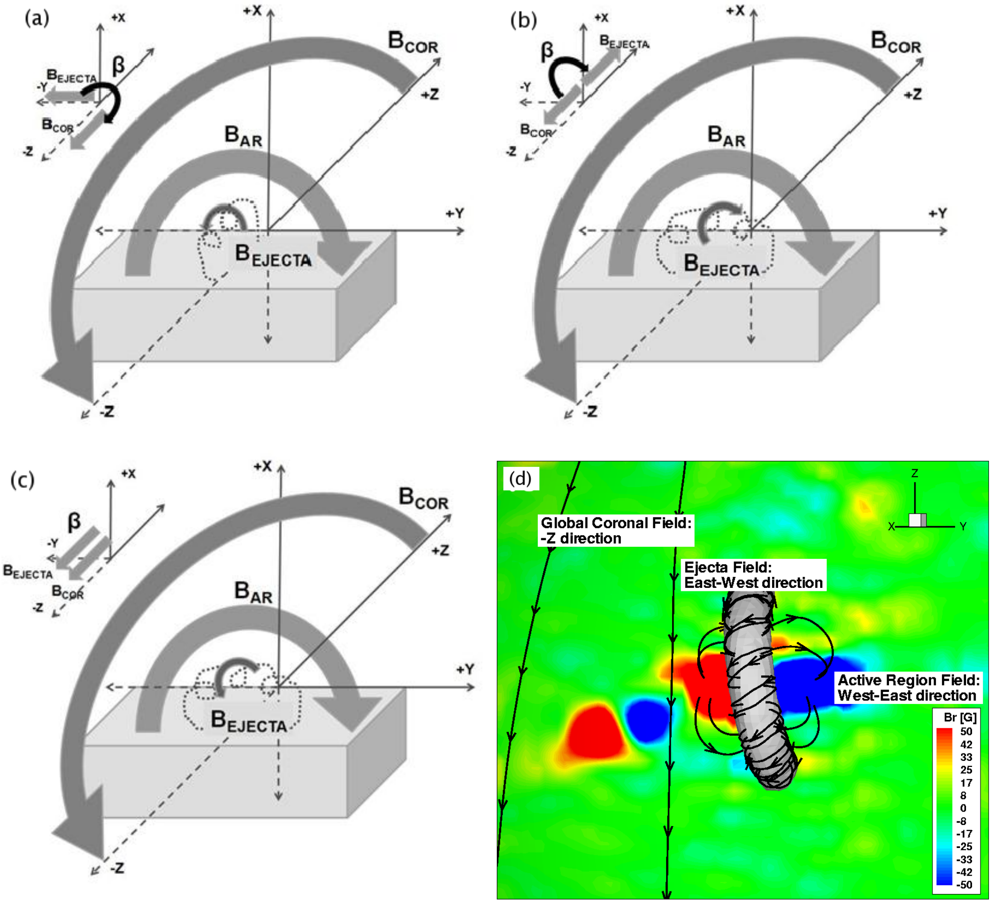

Figure 2.3: (a)-(c) Schematics to demonstrate the relative geometry of the ejecta field B_{ejecta}, active region field B_{ar}, and global coronal field B_{cor} in Cases A-C. The inserts show the definition of β, the angle between B_{ejecta} and B_{cor}. B_{ejecta} is (a) perpendicular, (b) antiparallel and (c) parallel to B_{cor} (which is in the -Z direction). B_{ar} is along the +Y direction. (d) Initial configuration (from the simulation) for the ejecta for Case A, inserted into AR8038. The solar surfce is colored with the radial component of the magnetic field. The gray isosurface is current density $J = 120\frac{mA}{m^2}$, which defines the surface of the flux rope, and the magnetic fields are labeled accordingly [Evans et al., 2011a].

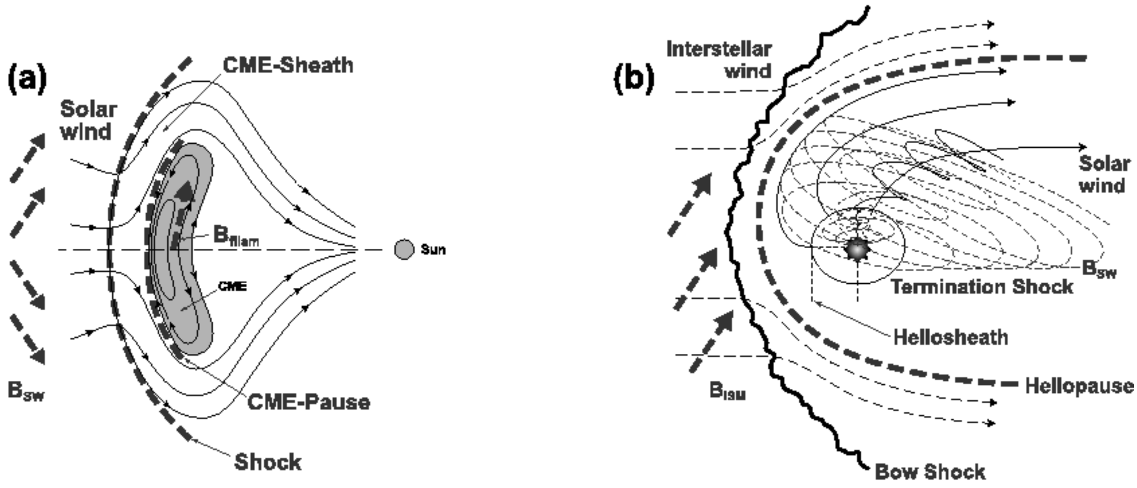

Figure 2.4: (a) An interplanetary coronal mass ejection (ICME) and (b) the outer heliosphere both present shock (CME-shock and termination shock) and sheath (CME-sheath and heliosheath) features. We draw on analogies between the two structures. The effect of the interstellar magnetic field (B_{ISM} in the outer heliosphere) corresponds to the effect of the magnetic field in the ICME (B_{ejecta}). See text for a detailed discussion. Figure adapted from Opher [2010].

$^3/_{256}$ $R_\odot$ is placed in the direction of the ICMEs' propagation [Evans et al., 2011a]. The rectangular box has dimensions of 1 $R_\odot$ in longitude, 1.8 $R_\odot$ in latitude, and extends to 6 $R_\odot$ in the ICME's path. The purpose of the box is to eliminate the influence of jumps in grid refinement on the ICMEs' evolution and capture the shock and ICME properties well near the nose. The total number of cells in the simulation domain is 12.4×10^6.

2.5 Study A: The role of the ejecta field

The magnetic field structure of the ejecta of a coronal mass ejection (CME) is not very well known near the Sun. In order to constrain this parameter, we draw an analogy between the outer heliosphere and CMEs. There are commonalities between the two structures (see Fig. 2.4, adapted from Opher [2010]. The supersonic solar wind in the outer heliosphere passes through a shock, called the termination shock (TS), as it approaches the interstellar medium (ISM). The TS is located 85-95 AU from the Sun [Stone et al., 2005, 2008]. The heliosheath is the region between the TS and the heliopause (HP; the contact discontinuity between the solar wind and the ISM). The subsonic solar wind propagates through the heliosheath and deflects around the HP. Similarly, an ICME can drive a shock as it propagates away from the Sun. In the rest frame of the shock, a supersonic solar wind is shocked as it moves in the Sunward direction. This subsonic flow deflects around the magnetic ejecta at the contact discontinuity (we refer to this structure as the CME-pause). The CME-pause is the location of pressure balance between the shocked solar wind and the magnetic ejecta, and so it is analogous to the HP. Between the CME-pause and the CME-driven shock is the CME-sheath. Therefore, in the direction of solar wind flow away from the Sun, an ICME is like an inverted heliosphere (Fig. 2.4).

The HP is distorted by the interstellar magnetic field pressure due to the compression of the magnetic field against the HP by the slowdown of the approaching interstellar flow. This slowing causes the magnetic pressure to dominate the thermal pressure close to the HP, forcing it to align with the interstellar magnetic field [Opher et al., 2007, Opher et al., 2009]. The subsonic heliosheath flows downstream of the TS are immediately sensitive to the shape of the HP and therefore can probe the interstellar magnetic field direction (which is poorly constrained). The *Voyager 2* spacecraft crossing of the TS [Stone et al., 2008] provided the first in situ data of the heliosheath flows. Opher et al. [2009] used a global simulation and *Voyager 2* observations of heliosheath flows to constrain the interstellar field magnitude and direction.

The analogous quantity to the interstellar magnetic field in the ICME case is the ejecta magnetic field. The photospheric magnetic field from synoptic maps, specifically the neutral line of the source active region, is used to constrain the ejecta field direction near the Sun. The presence of a sigmoid can constrain the flux rope's orientation, as the material often aligns with the neutral line of the active region [Gibson et al., 2002, Sterling et al., 2000]. However, the neutral line structure is often complex, especially for active regions which produce fast CMEs [Wang and Zhang, 2008]. Additionally, studies have found the ejecta's field orientation to lie both along and across the neutral line of the source active region [Wood and Howard, 2009, Zhao and Hoeksema, 1998]. There is also an example of in situ flux rope signatures with no identifiable eruption signatures [Robbrecht et al., 2009]. Therefore, the features of an active region are not a conclusive diagnostic for the initial orientation of the ejected magnetic field. In this work, we propose CME-sheath flow deflections as an additional constraint.

Spacecraft such as *Ulysses*, the *Advanced Composition Explorer (ACE)*, the *Solar Heliospheric Observatory (SOHO)*, and the *Solar Terrestrial Relations Observatory (STEREO)* provide direct plasma data as some part of the ICME structure passes. A magnetic cloud (MC; subset of ICMEs), is categorized by low temperature, low plasma beta, and a strong rotation of a highly organized magnetic field [Burlaga et al., 1981]. The observed rotation of the MC's magnetic field has been interpreted as a twisted flux rope [Goldstein, 1983]; however, numerical models have been used to arge that the rotation could instead be due to writhing of the field [Jacobs et al., 2009]. Irrespective of whether the magnetic structure of an ICME is a twisted flux rope, flux rope models are successful in reproducing observational signatures (Forbes et al. 2006 and references herein). The orientation of a MC's flux rope axis can be estimated using minimum variance analysis [Bothmer and Schwenn, 1998]. The global magnetic structure of an ICME can be reconstructed with multiple spacecraft measurements using methods such as the Grad Shafranov reconstruction, from which the flux rope axis can be found [Owens and Cargill, 2004].

The capability of CME-sheath deflection flows to indicate the geo-effectiveness of an ICME was investigated in Liu et al. [2008a]. They found that the meridional deflection speed was well correlated to the ICME's speed (relative to the solar wind). As the meridional flow is coupled to the meridional magnetic field, the ICME speed was suggested as a predictor of the sheath magnetic field. Using a numerical simulation in which an eruption was set from the equatorial region, Manchester et al. [2005] characterized meridional flows in the CME-sheath. They identified the deflection of high-latitude sheath plasma towards the equator, which created a compression region behind the shock (stronger than the shock compression itself).

In a survey of non-radial solar wind flows in 1998-2002 ACE data, Owens and Cargill [2004] found that half of all large flow events were associated with ICMEs. Five events without complex deflection were studied in detail. The measured sheath flow deflection was in agreement with the inferred local ICME geometry (determined with variance analysis), demonstrating that the deflection measured by a spacecraft depends on the local axis of the flux rope, and the separation of spacecraft and the axis.

The evolution of an ICME is, in general, determined by two factors: properties of the ejecta (such as magnetic field geometry with respect to the coronal and active region fields); and the background solar wind in which it propagates (for example, Liu et al. [2006b] showed that magnetic clouds are flattened by their interaction with the solar wind). The same background solar wind is used in each simulation, so in this work we do not account for different backgrounds.

If the CME's velocity is greater than the local Alfvén speed, it can drive a fast shock ahead of it. The structures of the ICME and shock system are: the ejecta (remnant of the flux rope), the CME-pause (the location of pressure balance between the ejecta and the sheath material), the CME-sheath (shocked solar wind between CME-pause and shock), and the CME-driven shock. The CME-pause is an important feature because the CME-sheath plasma must flow around this object, and so its size and shape will influence the structure of the sheath. Also, it can tell us information about the magnetic field of what is inside, which is the ejection field.

To define these structures, we consider the angle [Burlaga, 1988]

$$\theta_B = sin^{-1}\frac{B_N}{B} \tag{2.7}$$

where B_N is the normal component of the magnetic field in the Radial-Tangential-Normal (R-T-N) coordinate system (a Cartesian system defined at the location of the spacecraft; R is the direction from the center of the Sun to the spacecraft location, T is in the direction R $\times$ Z, and N completes a right-handed system). A strong change in this angle indicates

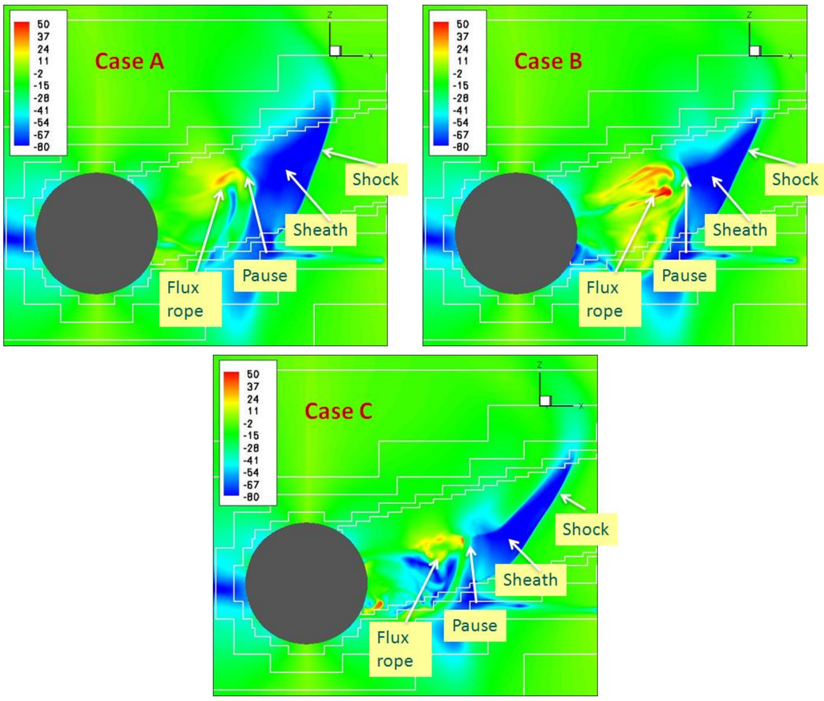

Figure 2.5: The angle θ_B is show in meridional slices for Cases A-C. This angle traces out the structures of the CME, like the shock, sheath, CME-pause and ejecta.

the boundary between regions of different magnetic fields, as can been seen in Figure 2.5. The simulation times correspond to the shocks reaching a height of 4.5 $R_\odot$, and the times are a) 40 minutes, b) 48 minutes, and c) 56 minutes after the flux rope was inserted. We can see the upstream solar wind, the shock, the sheath, and the ejecta. Features such as the shock inclination, sheath thickness, CME-pause size and shape differ significantly for the different cases.

Figure 2.6 shows the CME-pause for each simulated ejection, viewed along the +X axis looking towards the approaching ICME. We show an isosurface of temperature, $logT = 6.8$ (determined using the jump in θ_B described above). The contour gives the magnetic field strength, and the black lines show the ejecta magnetic field just inside the CME-pause (to show the different draping of the field around the CME-pause). The white line indicates the path of an artificial satellite, along which we measure the height of the CME-driven shock. The simulation times correspond to the shocks reaching a height of 4.5 $R_\odot$. The times are

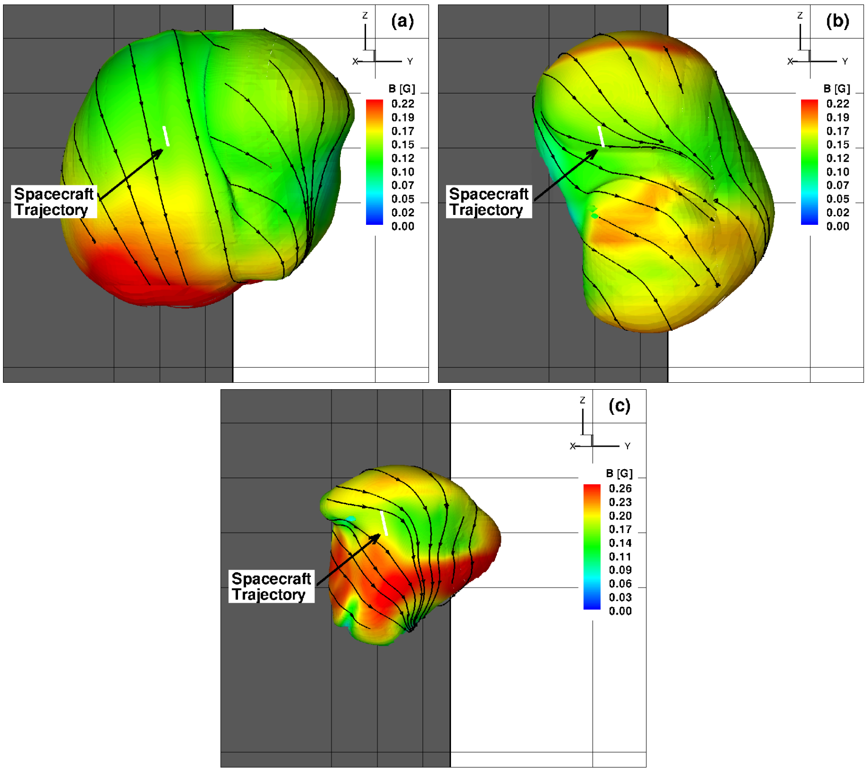

Figure 2.6: Isosurfaces of the CME-pause for (a) Case A, (b) Case B, and (c) Case C. The view is from a position along the +X axis looking toward the approaching ICME, and the surface was defined as an isosurface of temperature ($logT = 6.8$, T in K). The contour gives magnetic field strength, and the black lines show the ejecta magnetic field inside the CME-pause. The white solid line indicates the trajectory of an artificial spacecraft, and the simulation times (a) 40 minutes, b) 48 minutes, and c) 56 minutes after the flux rope was inserted correspond to the CME-driven shocks reaching a height of 4.5 $R_\odot$ along this trajectory. Note the differences in the shape and size of the CME-pause [Evans et al., 2011a].

a) 40 minutes, b) 48 minutes, and c) 56 minutes after the flux rope was inserted.

The CME-pause shape is different for each case, due to the magnetic pressure of the ejecta near the CME-pause dominating the thermal pressure. The average ratio of thermal to magnetic pressure is 0.083 (measured inside the ejecta for the three cases when the CME-pause is located at 4.5 $R_\odot$). The location on the CME-pause where the magnetic field strength is intensified is different for the three ejecta field configurations. As a result, the CME-pauses are distorted differently for different ejecta field orientations. This will cause different deflections of the subsonic CME sheath flows,

$$\theta_F = tan^{-1}\frac{V_N}{V_T}. \tag{2.8}$$

V_N and V_T are, respectively, the normal and tangential components of the plasma flow in the R-T-N coordinate system. We extracted data from a velocity streamline which intersects the artificial spacecraft's trajectory (shown as a white line in Figure 2.6) inside the ejecta. This method was chosen to ensure that we tracked the same location on the CME-pause at all times.

The deflection angle θ_F just downstream of the shock when the CME-driven shock position was 6 $R_\odot$ was: Case A: -86°; Case B, -82°; Case C, -77°. The deflections were not significantly different between the cases. The deflections just before the CME-pause are different by greater amounts: $\Delta\theta_F$ = 19, 82 and 101°. It can be seen that the deflection measured by a spacecraft is determined by the axis of the flux rope (which can be seen to be aligned with the CME-pause) and the distance from the axis. The same was found in the outer heliosphere [Opher et al., 2009]. These conclusions are also supported by an observational survey [Owens and Cargill, 2004].

Next we looked at the evolution of the flow deflection for each case. The magnetic field of a flux rope may rotate during propagation in the lower corona as a result of the Lorentz force [Isenberg and Forbes, 2007], and reconnection with the overlying fields, as shown in simulations by Cohen et al. [2010], Lynch et al. [2009] and Shiota et al. [2010]. This rotation will modify the shape of the CME-pause. The evolution of the flow deflection angle in this simulation is determined by the ejecta field evolution - the solar wind does not contribute to any differences between the three cases because each ejecta was launched into the same background solar wind.

We found that the evolution of θ_F has almost ceased by 6 $R_\odot$ for Case C. We calculated the magnetic energy density of the ejecta as a function of time and used that value to estimate how much reconnection occured in the simulation. As it is an ideal MHD simulation, all reconnection is purely numerical. We found that Case C had the least amount of reconnection, which is in agreement with its initial configuration: ejecta field perpendicular to the active region field and parallel to the global coronal field. Case B (ejecta field perpendicular to the active region and antiparallel to the global coronal field) experienced the most reconnection, and its deflection angle was still evolving at 6 $R_\odot$. Case A was similar to Case C. These results are in agreement with [Yurchyshyn et al., 2007], who found, using the Large Angle Coronagraph-Spectrograph (LASCO) white light images, that most flux ropes rotate by only about 10° above 6 $R_\odot$.

2.6 Study B: Piled-Up Compression

Next, we will look more at the plasma in a CME-sheath, focusing on the accumulation of material in front of the ejecta, and the consequences for particle acceleration. This work was presented in Das et al. [2011].

CMEs expansion can have several causes [Gosling et al., 1998]: the leading edge could be traveling faster than the back of the CME; the internal pressure (magnetic or thermal) could be more than that of the surrounding solar wind. Without a source to feed the expansion, it should decrease with distance from the Sun. Démoulin and Dasso [2009] showed that the observed expansion of magnetic clouds can be explained by considering the behavior of the solar wind pressure with distance - it drops off rapidly. Dasso et al. [2007] showed an expansion in the direction of propagation by calculating leading and trailing edge velocities.

The lateral expansion speed was empirically found to be related to the radial velocity as $V_R = 0.88 \times V_{EX}$ [Dal Lago et al., 2003], and the expansion speed could approach 2,000 km/s.

Siscoe and Odstrcil [2008] described the situation in which the deflection speed of the solar wind near the leading edge of an ICME is not large enough to let it flow around the body of the ICME, causing the solar wind to pile up around the ejecta. As the CME/ICME expands and propagates faster than the laterally deflected flow, the solar wind is expected to pile up in front of the nose of the object. In a numerical simulation similar to the one presented in this chapter, Liu et al. [2008b] first showed the formation and enhancement of a density structure at the back of the CME-sheath below 5 $R_{\odot}$. Dasso et al. [2007] showed observations of mass pile up in front of a CME/ICME at 1 AU. Ontiveros and Vourlidas [2009] show a high density compression behind the shock and ahead of the driver which they attributed to pile up. Möstl et al. [2009] showed in coronagraph images that there were two density peaks surrounding the dark cavity region. They explained the peak as solar wind material swept up by an expanding flux rope.

In Figure 2.7, we show the same type of density peak seen in [Möstl et al., 2009] appearing in front of the CME-pause in our simulation. We term this feature piled-up compression (PUC). The structures in the figure are determined with the parameter θ_B [Evans et al., 2011a], and labeled as: plasma depletion layer (PDL) [2], the PUC outlined in light yellow shaded region, and the flux rope (FR) in light blue. We calculate the PUC strength by taking the ratio of the maximum density in the sheath and the density value downstream of the shock. The value is larger than 10 along the line presented in Figure 2.7 from 2-5 $R_{\odot}$. In Figure 2.8, we show the ratio of the line of sight integrated white light intensity at time 40 minutes to the pre-CME value. The black lines show the CME-pause, and it can be seen that the PUC occurs at the back of the sheath, and is strongest at the top of the CME.

The high density regions between the PUC and the forward shock could facilitate the accelerations of charged particles in the lower corona. We are currently working on this

[2] Discussion on the formation of the PDL can be found in Das et al. [2011]

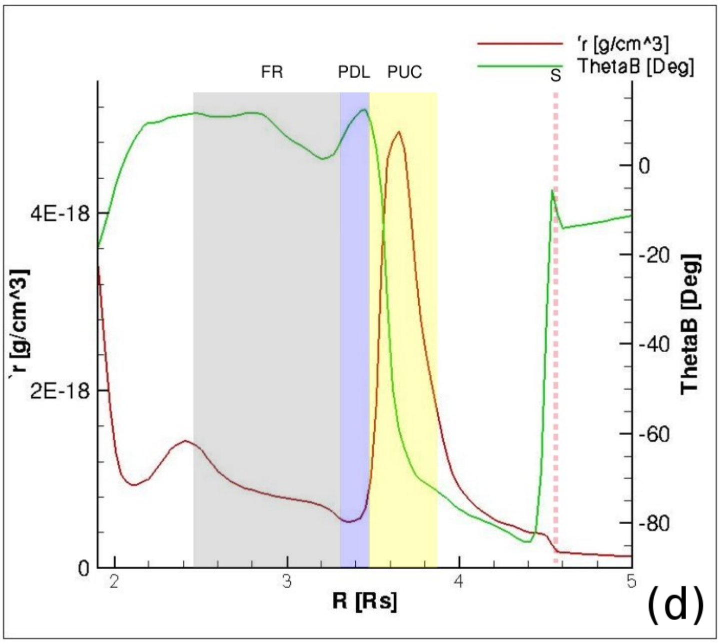

Figure 2.7: Line plot showing plasma density and θ_B as a function of height along a radial line [Das et al., 2011].

project, and present our preliminary results in estimating particle acceleration along magnetic field lines in Chapter 7.

2.7 Study C: Thermal Energy of CME

In this section, we present the evolution of the thermal energy of the CME, which was described in Loesch et al. [2011]. In Figure 2.9, we see that the thermal energy dominates over the kinetic and magnetic energies above 2 $R_{\odot}$. Also, the thermal energy is contained inside of the ejecta. Also, the shock compression ratio is large (3-4), which is in contrast to observations [Ontiveros and Vourlidas, 2009]. The value of the polytropic index from the steady state solar wind solution was not allowed to evolve after the flux rope was inserted. As the flux rope expanded, its density decreased (lower than the density in the steady state solar wind). Since the heating term was fixed, the thermal energy of the ejecta increased with time, and dominated the kinetic and magnetic energies. Therefore, these

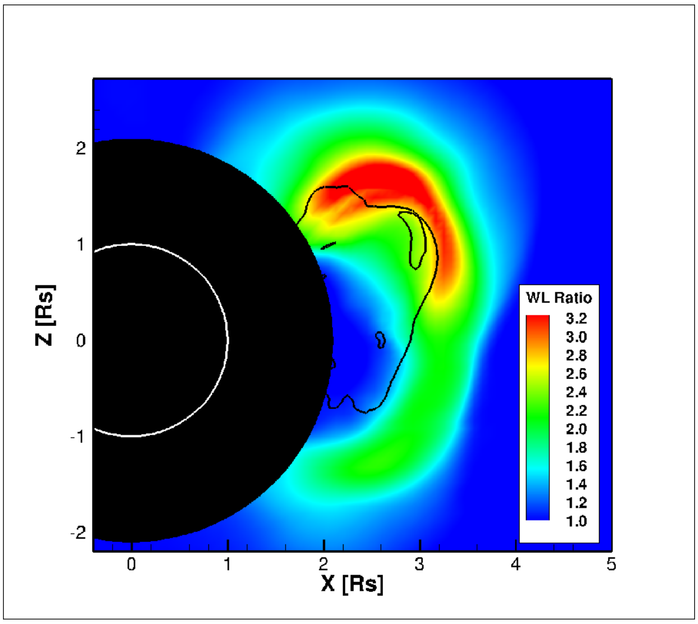

Figure 2.8: Synthetic white light coronagraphic image, 42 minutes after the flux rope was inserted. The black line locates the CME flux rope on the X-Z plane. The black disk shows the blocked portion of the Sun. WL Ratio at any location is defined as the ratio between its density integrated along the line-of-sight at that time and background density at the corresponding location when no CME was present [Das et al., 2011]

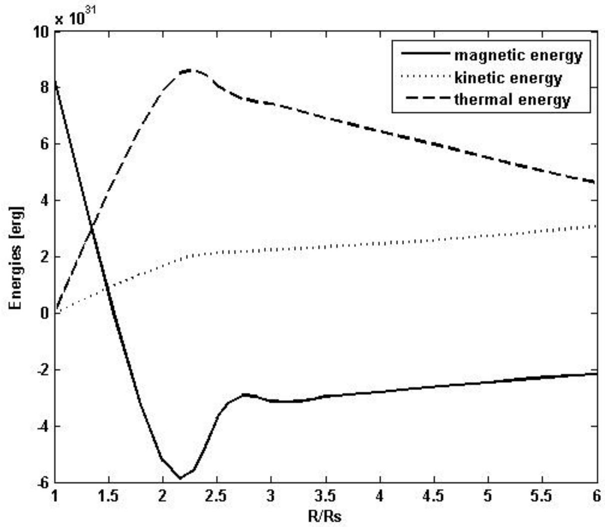

Figure 2.9: Energy profiles as a function of shock position, until 6 $R_{\odot}$. The energy at each position is computed by integrating over the entire simulation box, and subtracting the corresponding energy calculated from the steady state solution [Loesch et al., 2011].

results suggest that a polytropic solar model is not well suited to model CME-driven shocks.

2.8 Discussion

The goal of this chapter was to study the evolution of a CME in a polytropic solar wind background in the lower corona. First, by simulating three eruptions with different flux rope field directions, we found that the CME-pause size and shape are extremely sensitive to the ejecta magnetic field orientation. The magnetic pressure from the ejecta pushes out on and shapes the CME-pause. The deflection flows in the CME-sheath are sensitive to the pause, and so deflection angles measured by the same spacecraft for our three simulation cases are distinguishable from each other ($\Delta\theta_F = 45 - 98°$ at the CME-pause). This demonstrates that the flows are sensitive to the ejecta magnetic field.

We find that the flow deflection angle evolved with height until 6 $R_{\odot}$. The source of this evolution is the rotation of the ejecta due to the Lorentz force [Lynch et al., 2009] and magnetic reconnection [Cohen et al., 2010]. The initial orientation (and magnitude) of the ejecta field in relation to the coronal field determines the amount of rotation in the lower corona. We found the evolution of θ_F diminishes as the CME propagates. If the ejecta field does not undergo significant rotation after 10 $R_\odot$, then θ_F at the same location on the CME-pause would be frozen-in during propagation through the heliosphere, relating a lower corona quantity to a measureable quantity in the heliosphere.[3]

The evolution of the CME-sheath flows is related to the evolution of the ICME, which is determined by two factors: the ejecta's properties and the background solar wind in which it propagates. Reconnection causes acceleration and rotation, and the location and strength of the reconnection may be determined by the ejecta field strength and direction. Later (Chapter 7) we will describe a future project which will improve the physics of reconnection in MHD modeling of CMEs.

However, we also found that the method used to drive and heat the solar wind (varying polytropic index) resulted in unphysical CME heating. This makes us question the feasibility of using a polytropic model for understanding the kinematics of CME evolution. In the next chapter, we study more solar wind models and their approaches to coronal heating, to see if any of those choices affect the lower corona environment in a negative way.

[3]see Vourlidas et al. [2011] for an example of strong rotation above 10 $R_\odot$.

Chapter 3: The Background Solar Wind and CME-Driven Shocks

3.1 Introduction

In this chapter, we use observational constraints on shock formation in the lower corona to challenge the use of ad hoc heating in global MHD modeling. A shock forms by the steepening of a driven pressure wave, for example when a disturbance traveling slower (or faster) than the background Alfvén speed [1]. Whether the potential driver (flare or CME) forms no shock, one shock, or multiple shocks in the lower corona largely depends on the profile of the Alfvén speed [Forbes et al., 2006].

Type II radio bursts and energetic electron events [Klassen et al., 2002, Mewaldt et al., 2003] indicate that CME-driven shocks can accelerate particles very low in the corona. Therefore, understanding the formation and evolution of shocks near the Sun is crucial. Tylka et al. [2003] related high energy (GeV/nucleon) solar energetic particles (SEPs) observed in ground-level events to CME-driven shocks below 4 $R_\odot$. In a type II radio burst survey, [Gopalswamy et al., 2005] determined an average source CME height of 1.6-2.2 $R_\odot$. Also, they also found that only 5 of 72 sampled CMEs that were associated with large SEP event had speeds less than 1000 km/s.

These observations show that it is crucial for global MHD models to have a realistic lower corona to simulate CMEs in the lower corona. However, global models are limited by the difficulty of treating microphysics over large scales, for example, resolving the several orders of magnitude variations of density and temperature across the transition region [Downs et al., 2010]. As a result, most MHD models start at the base of the lower corona

[1] The characteristic velocity is the fast magnetosonic speed, but in the lower corona the Alfvén speed is much larger than the sound speed, and so we neglect the sound speed.

and use ad hoc approaches to achieve coronal heating and wind acceleration. The methods include: 1) utilizing an empirical heating function or non-uniform polytropic index distribution [Cohen et al., 2007, Groth et al., 2000, Mikić et al., 1999, Roussev et al., 2003]; 2) Alfvén wave energy without damping [Lionello et al., 2009]; and 3) Alfvén wave energy with an empirical damping length [Ofman, 2004, Usmanov and Goldstein, 2006]. These models are benchmarked with observations in the inner heliosphere (for example with *Ulysses* or *ACE*), but not in the corona.

Local (1D or 2D) models are useful tools to test coronal heating mechanisms because they include higher resolution than global models. They can treat the photosphere, chromosphere, and transition region individually and can include more detailed physics. Models of closed loops [Rappazzo et al., 2007] and open flux tubes [Cranmer et al., 2007, Verdini and Velli, 2007] investigated MHD turbulence to dissipate Alfvén wave energy through a nonlinear interaction of outwardly propagating and reflected waves. The results of these simulations can be useful to global modelers, such as the scaling of the heating rate with magnetic field for strong and weak fields [Rappazzo et al., 2007]. In this chapter, we show that these local models are in better agreement with the observational constraints on the Alfvén speed profile in the lower corona than global MHD models.

3.2 Models

Below we describe the ten models whose Alfvén speed we analyzed in the lower corona. The first group of models is global MHD models which primarily drive the solar wind with thermal heating functions; the second group is semi-analytic models, and the final group is MHD models which include damped Alfvén waves. The magnetic fields are modeled as multipole expansions or calculated from the Potential Field Source Surface (PFSS) model using magnetograms. The density is either constrained by observations or solved using MHD equations and an assumed density at the inner boundary. All models were chosen for solar minima conditions.

3D Global MHD Models with Thermal Empirical Heating: M1-M5

M1: Manchester et al. [2004] (MA04) Groth et al. [2000] introduced an empirical heating function (exponentially decreasing and latitude dependent) into the MHD equations to drive the solar wind by recreating the effects of energy absorption, thermal conduction and radiative losses. This steady-state solar wind model was used in MA04 to model the propagation of a CME from the Sun to 1 AU. The magnetic field is treated as a multipole expansion using observations as constraints. The advantages of this model are that it provides a global 3D picture and agreement with observations near 1AU. The disadvantages of this model are that it uses a simplified magnetic field model and drives the solar wind solely with thermal heating.

M3: Roussev et al. [2004] (RO04) RO04 extended the model of [Groth et al., 2000] by incorporating magnetograms and using the Potential Field Source Surface (PFSS) model to extrapolate the magnetic field from the photosphere into the corona. The PFSS model has been successful at predicting interplanetary magnetic field polarity and the solar wind speed at Earth [Arge and Pizzo, 2000]; however it is known that PFSS models obtain a weak magnetic field value at 1 AU. This problem is currently resolved by increasing the magnetic field intensity at the Sun. This model employs a non-uniform polytropic index distribution, as in Roussev et al. [2003]. The advantage of this model are that it provides a global 3D picture, agreement with observations near 1AU, and a complex magnetic field configuration. The disadvantage of this model is that it drives the solar wind solely with thermal heating.

M2: Cohen et al. [2007] (CO07) Like RO04, CO07 includes magnetograms and employs a non-uniform polytropic index distribution to drive the solar wind. The Wang-Sheeley-Arge (WSA) PFSS model is used in conjunction with the Bernoulli integral to extrapolate the polytropic index from the source surface to the solar surface along magnetic field lines, resulting in a polytropic index which depends on solar wind velocity and temperature. The model is tested for both solar minimum and maximum conditions, and the solar wind velocities at 1 AU match better to observations for solar minimum conditions. For this study, we include the model with CR1922 (solar minimum conditions). The advantages of this model are that is provides a global 3D picture, agreement with observations near 1AU, and a complex magnetic field configuration. The disadvantage of this model is that it drives the solar wind solely with thermal heating.

M4: Riley 2006 (RIL06) The polytropic 3D MHD model of RIL06 also makes use of magnetograms. RIL06 uses an adiabatic energy equation with a reduced polytropic index and solves the set of resistive MHD equations [Mikić et al., 1999]. The advantages of this model are that it provides a global 3D picture and a complex magnetic field configuration. The disadvantages of this model are that it produces an unrealistic density profile and drives the solar wind solely with thermal heating.

M5: Lionello, R. 2008 private communication (LI08) This 3D MHD model differs from the other MHD models in that the lower boundary extends down to include the chromosphere and transition region, while others start in the lower corona. The magnetic field configuration is generated using smoothed magnetograms, and the profiles in this study correspond with CR1913. The model includes uniform viscosity and uniform resistivity, both of which are smaller than realistic values by computational limitations. The model uses an energy equation which explicitly treats radiation loss and coronal heating, and includes a term to represent (undamped) Alfvén waves. The coronal heating is an empirical exponential function similar in form to that of MA04 except that it depends only on radial distance. The advantages of this model are that it utilizes magnetograms, it includes the chromosphere and transition region and an improved energy equation including Alfvén wave momentum. The disadvantage of this model is that it primarily drives the solar wind with thermal heating.

Semi-analytic Models: M6 & M7

M6: Mann et al. [2003] (MA03) MAN03 is a semi-empirical model for an equatorial active region. The magnetic field is a background quiet Sun (which goes like r^{-2}) superimposed with an active region modeled as a dipole. The electron density is a combination of two models: the one-fold Newkirk [1961] model is used from the surface until 1.8 $R_\odot$, where the solution is matched with the model from Mann et al. [1999], which matches well with Wind observations above 1.8 $R_{\odot}$ and is suitable for active regions. The reason for the two sources is because the Newkirk model matches better to observations in the quiet equatorial region near the Sun, but fails to match above 1.8 $R_{\odot}$. The advantage of this model is that it utilizes an observed density profile. The disadvantages of this model are that it is a 2D model and it uses a simplified magnetic field model.

M7: Guhathakurta et al. [2006] (GSO06) Sittler and Guhathakurta [1999] (herein SG99) developed a global electron density based on from observations (SOHO Whole Sun Month and Ulysses data, see SG99). The magnetic field in GSO06 is also taken from SG99, and takes the form of a multipole expansion whose expansion factors are constrained by coronal observations (SOHO/EIT and Ulysses). The chosen magnetic field produces good results in the polar regions, but is poorly applicable in the equatorial region. As a result, the Alfvén speed profile for the equator from this model is taken above 2.5 $R_{\odot}$. The advantages of this model are that it utilizes observed values of density and magnetic field. The disadvantages of this model are that it is a 2D model and it drives the solar wind solely with thermal heating.

Models with Alfvén Wave-Driven Winds: M8, M9 & M10

M8: [Cranmer et al., 2007] (CR07) CR07 drives the solar wind with Alfvén waves and MHD turbulence. This 1D radial model contains acoustic and Alfvén wave pressure to accelerate the solar wind, utilizing acoustic waves to heat the chromosphere and Alfvén waves in the corona. The main strategy is to cascade the energy from large scale Alfvénic fluctuations to high frequency collisionless kinetic modes. This cascade is accomplished by partially reflecting Alfvén waves to create ingoing waves to damp the outgoing waves. As in Cranmer and van Ballegooijen [2005], the initial magnetic field structure is a multipole expansion slightly modified from Banaszkiewicz et al. [1998]. The initial radial dependence of the electron density is derived to match white-light polarization brightness measurements in the extended corona. Their model includes terms from radiation, conduction, Alfvén and acoustic wave damping. The advantage of this model is that it includes waves and thermal heating. The disadvantages of this model are that it is 1D radial and applies solely to coronal holes.

M10: Verdini and Velli [2007] (VE07) VE07 is a local heating model including a static photosphere and chromosphere, transition region, and open corona. Global MHD models do not include these lower regions because of the high resolution needed to resolve these layers, instead using the corona as a lower boundary. VE07 incorporate Alfvén wave reflection and dissipation and use Ulysses and Helios data as constraints. The numerical model solves the MHD equations assuming incompressible, adiabatic transverse fluctuations in the velocity and the magnetic field, following waves in the frequency range 10^{-6} Hz to 10^{-2} Hz. The chromosphere and photosphere are considered to be isothermal, with an exponentially varying density and a flux tube geometry chosen to agree with a quiet Sun coronal hole model [Hollweg et al., 1982]. In the corona, the temperature is given by the semi-empirical model of Casalbuoni et al. [1999]. The advantages of this model are that it drives the solar wind with waves, it includes the lower layers of the solar atmosphere, and it uses observations as constraints. The disadvantages of this model are that it uses a simplified density model and it does not provide a global picture.

M9: Usmanov and Goldstein [2006] (UG06) In this 3D model, the solar wind is driven by including Alfvén wave momentum and energy in the WKB approximation. WKB approximation is valid as long as the waves have wavelengths shorter than local characteristic scale. WKB approximation is useful in a global model because it does not require a high-resolution description of the momentum and energy transformations from the waves to the flow. The set of MHD equations solved include an additional equation with two new variables: the Alfvén wave energy density and the velocity of the Alfvén waves. The MHD equations are solved only in the inner region (1-20 $R_\odot$), and in the outer region the solution is given by forward integration along the hyperbolic radial coordinate. The free parameters were chosen to fit the Ulysses data and the computed values match fairly well near 1 AU. The advantages of this model are that is provides a global 3D picture and it drives the wind with Alfvén wave momentum. The disadvantages of this model are that it uses a simplified magnetic field model and artificial damping for Alfvén waves.

3.3 Alfvén Speed Profile in the Lower Corona

Figure 3.1 shows the Alfvén speed profiles for all models: polar/open field region profiles are shown in Figure 3.1a, equatorial streamer profiles in Figure 3.1b, and active region profiles in Figure 3.1c.

For the semianalytic models (M6 and M7), there are two characteristics of the Alfvén speed profiles: a minimum (valley) around 1.5 $R_\odot$ in MAN03, and a maximum (hump) around 3.8 $R_\odot$ in both MAN03 and GSO06. These profiles are consistent with the studies of type II radio bursts mentioned earlier. They are also consistent with the profile used in Gopalswamy et al. [2001] to explain the relation among metric, decameter-hectometric, and kilometric type II bursts, in addition to the formation of shocks at 1-3 $R_\odot$. In addition, the valley and hump structures also allow for the formation of multiple shocks. Although simplified models, the semianalytic studies are based on observed values of density and magnetic field. For the MAN03 profile, a driving agent (e.g., CME or flare) with velocity could form a shock between 1-3 $R_\odot$. The shock would dissipate by 4 R as a result of the hump in the Alfvén speed, and reform after 5 $R_\odot$.

For the global MHD models driving the solar wind with thermal heating (M1,M2,M3,M4,M5), the profile in the equatorial region either drops off quickly to 500 km/s 1 below 1.4 $R_\odot$, or has a hump and a low Alfvén speed ($< 500 km/s$) in the lower corona. In Figure 3.1c, the letters C, D, and E for M2 indicate the direction of propagation out of the active region: C is straight out through the center, and Dand E are taken at an angle from the center of the AR, D lying in a meridional plane and E in a plane parallel to the equatorial plane.

For the global MHD model with Alfvén wave-driven wind and unrealistic damping (M9), the profile falls off much less rapidly than the MHD models that use empirical heating (see Figure 3.1b). However, by 5 $R_\odot$ it matches well with the other global MHD profiles. This profile does not contain a hump.

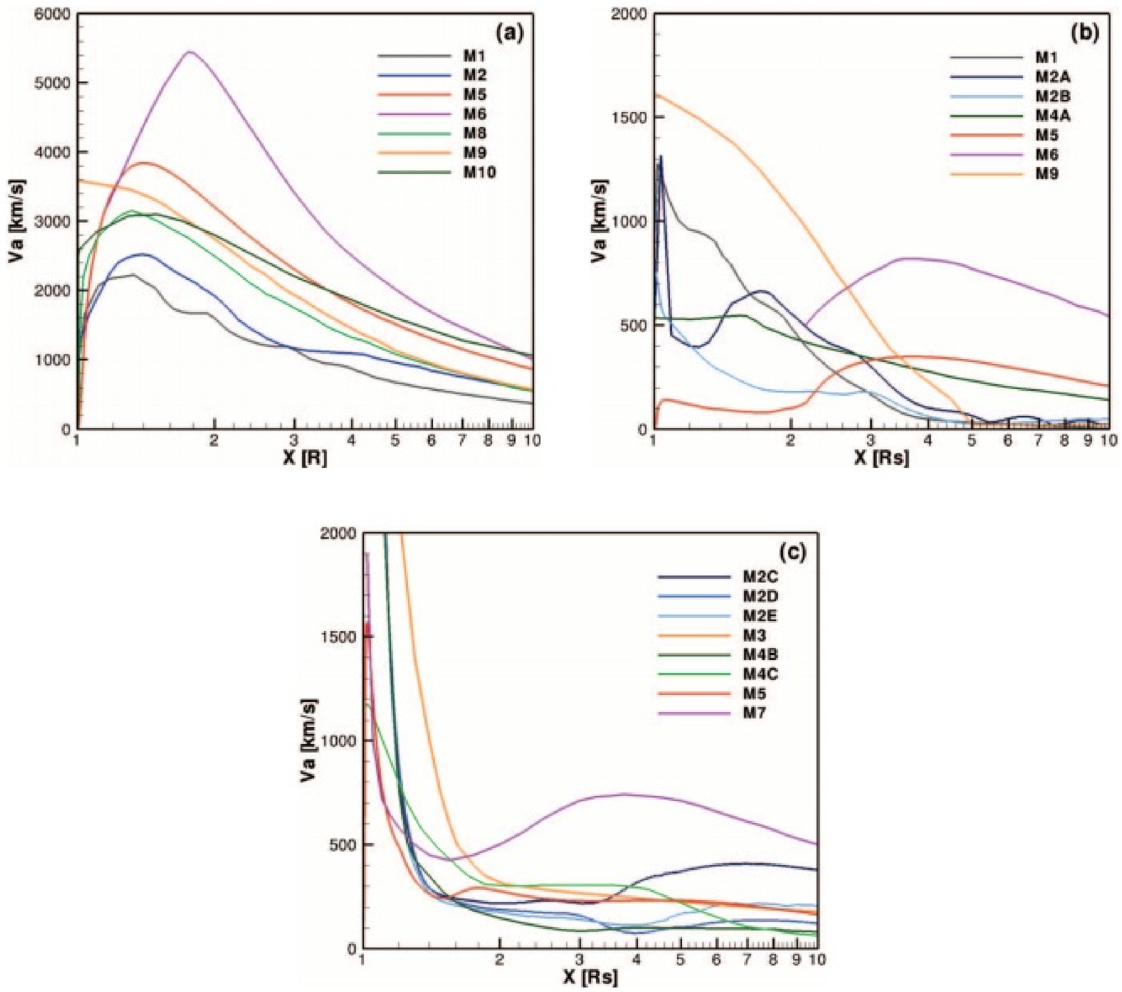

Figure 3.1: Alfvén speed profiles for (a) the polar open field regions, (b) streamers, and (c) active regions. [Evans et al., 2008].

For the local studies of Alfvén wave-driven winds (M8 and M10), the profiles contain a hump, although very close to the Sun, below 2 $R_{\odot}$ (see Figure 3.1a). Below 8 $R_{\odot}$, the magnitude of the Alfvén speed for these two models is larger than the global MHD models that only include thermal heating, and smaller than for the semiempirical model. Also, the hump is closer to the Sun for the models including Alfvén waves compared to the semiempirical model.

In the plots shown in Figure 3.1, the Alfvén speed profile for streamers was taken from

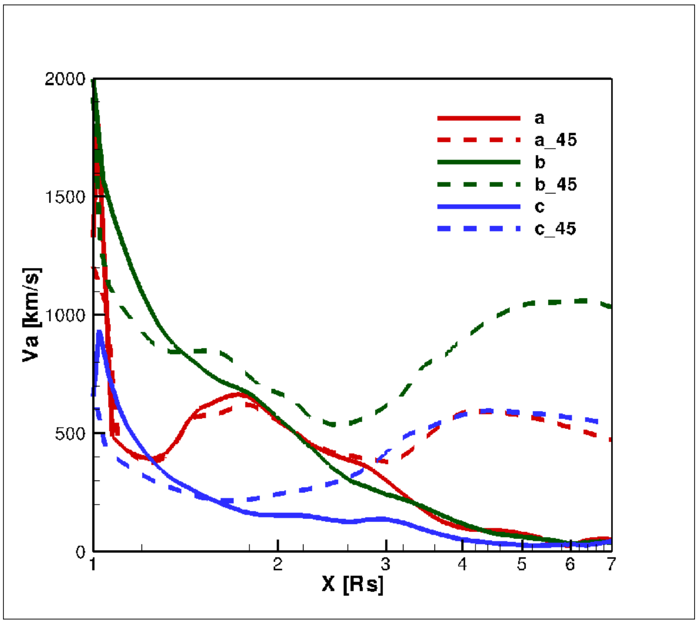

Figure 3.2: Alfvén speed for propagation in the meridional plane radially out of a streamer (solid lines) and 45° away from the center of the streamer (dashed lines) (O. Cohen 2007, private communication). The labels a, b, and c correspond to variations in thermal heating [Evans et al., 2008].

the line through the center of the streamer. We investigated the effect of the direction of propagation on the Alfvén profile using one single MHD model (see Figure 3.2). The motivation was that (1) the Alfvén speed will have directional dependence as $Bcos(\theta)$ and (2) the MAN03 plot of Alfvén speed (which shows a clear hump) is taken 45° away from the line through the center of the active region. We took new profiles from 45○ away from the streamer for the CO07 model with three variations (labeled a, b, and c in Figure 3.2) in thermal heating obtained by varying the magnetic field (in order of increasing strength, a, c, b) and density (in order of increasing value a, c, b) at the inner boundary (solar surface).

In the quiet Sun, propagation at an angle has two effects: a hump develops around 5-6 $R_\odot$ for all three cases of variation of thermal heating. For propagation straight out of the streamer, the Alfvén speed drops quickly for all three cases. Finally, we investigated the Alfvén speed profile near an active region. The Alfvén speed profile was found to be comparable to the fast polar profile 0.2 $R_\odot$ above the surface and enhanced compared to the quiet Sun until 0.5 $R_\odot$ for model M2. In model M4, a profile taken $10^\odot$ Carrington latitude away from an AR still differed from the quiet-Sun profile. In addition, profiles taken obliquely out of an AR were found to differ in the magnitude and location of the hump from each other and from the profile taken radially out of the AR.

3.4 Discussion

This chapter presented a study of the implication of the method of driving the solar wind in the lower corona, in particular in the Alfvén speed profile. State-of-the-art global MHD modeling has allowed for numerous studies of the formation, propagation, and interaction of solar phenomena such as CMEs with the terrestrial magnetosphere. This modeling is a powerful tool for creating a realistic 3D picture of these solar disturbances. Most models are benchmarked with plasma parameters near 1 AU from observations of satellites such as ACE, Wind, Ulysses and STEREO. Although the MHD models consistently reproduce aspects such as density and magnetic field structure, and the bimodality of the solar wind at 1 AU, we have shown here that they are not consistent with type II radio burst observations in the lower corona. We associate this mismatch as a result of the different methods of solar wind acceleration and coronal heating.

As shown in [Evans et al., 2008], global magnetohydrodynamics models produce Alfvén speed profiles that are in conflict with observations: (1) multiple SEP events are observed with a single exciting agent, but most profiles are missing the hump required to form multiple shocks; and (2) few slow CMEs cause large SEP events, but most profiles drop very quickly, allowing all slow CMEs to drive strong shocks to form below 4 $R_\odot$. Simplified Alfvén wave-driven wind models have steeper profiles, but are still in disagreement with multiple shock formation. Only studies that include Alfvén waves with physics-based damping are in agreement with observations. This implies that the results of these one-dimensional local studies should be included in global models before we can study shock formation in the lower corona.

The inclusion of Alfvén waves with unrealistic damping in a global MHD model steepens the Alfvén speed profile, but it is still not in agreement with these observations. Only local studies including Alfvén waves with physically motivated damping achieve: a) the steepened profile and b) the hump needed to align the models correctly with observations from type II radio bursts and energetic electron events. This implies the results of these studies must be included in global models before we can study shock formation in the lower corona. We do so in the next chapter, by studying the damping mechanism of surface Alfvén wave damping.

Finally, we also look at the effect of the direction of propagation of the exciting agent, for example a CME. Propagation at an angle has two effects: above 3 $R_\odot$, a hump develops around 5-6 $R_\odot$ for all three cases of variation of thermal heating. For propagation straight out of the streamer, the Alfvén speed drops quickly for all three cases. Based on these results, forming multiple shocks is not only dependent on the driving agents speed and Alfvén speed, but also on the direction of propagation from the active region. A CME which propagates at an angle to the streamer will be more likely to form multiple shocks.

Chapter 4: Surface Alfvén Wave Damping as a Heating Mechanism for the Solar Wind

4.1 Introduction

A motivation behind this thesis is that the the ability to accurately forecast space weather events at Earth is limited in part by the lack of a realistic background solar wind model in which to propagate solar disturbances.

In Chapter 2, we showed that a polytropic solar wind background resulted in unphysical heating of a CME in the lower corona. In Chapter 3, we showed that global models which utilized ad hoc heating mechanisms (such as the polytropic model) generate an Alfvén speed profile in the lower corona which seems to be in disagreement with observations of shock-accelerated particles. We argued that the physics of Alfvén waves must be included in MHD modeling with a physical damping mechanism (as in local models). The first global models which specify physically motivated wave dissipation are currently being developed [Lionello et al., 2009, Oran et al., 2010, van der Holst et al., 2010]. (For reviews of solar wind modeling, and discussions on the successes and challenges see Cranmer [2010], Ofman [2010]).

In the lower corona, the frequencies of Alfvén waves expected to be appreciably damped are: below those strongly damped in the chromosphere (1 Hz; Leake et al. [2005]); and on the order of those dominating in the heliosphere (10^{-4} Hz; Belcher and Davis [1971]). The possible damping mechanisms for low frequency Alfvén waves in the lower corona are numerous [Narain and Ulmschneider, 1996]. Commonly accepted dissipation mechanisms include ion-cyclotron resonance [Chandran et al., 2010, Cranmer et al., 1999, Isenberg et al., 2001] (thought to dominate in the fast solar wind) and turbulent dissipation [Cranmer et al., 2007, Verdini and Velli, 2007] (which occurs in both open and closed field regions).

Until now, no global wave-driven solar wind models have focused on wave dissipation at the region at the boundary of open and closed fields, even though there is evidence that the heating mechanism along open field lines in this region is different than the generally accepted mechanisms in the fast solar wind, wuch as ion cyclotron resonance. First, a signature of ion cyclotron resonance is that the heating is proportional to the ratio A/Z (A is the atomic mass and Z is electric charge). The preferential heating of heavy ions is seen in the center of coronal holes. However, at the streamer center and at the border with open field lines, Si XII had a higher temperature than O VI (Zangrilli et al. [1999]; UltraViolet Coronagraph Spectrometer (UVCS) data). This suggests that another mechanism could be dominant. Second, turbulent dissipation requires incoming (sunward) waves. These waves are thought to be generated by the reflection of outgoing waves due to gradients in the Alfvén speed along the direction of the magnetic field [Cranmer and van Ballegooijen, 2005, Velli, 1994]. However, at the boundary region, the gradients in the Alfvén speed across the magnetic field could be comparable or stronger to that along the magnetic field [Vásquez et al., 2010].

Additionally, there are observations which suggest that strong heating occurs at the boundary of open and closed fields. Vásquez et al. [2010, 2011] produced three-dimensional (3D) reconstructions of electron density and temperature in the very low corona (from local differential emission measure (LDEM) technique applied to extreme ultraviolet Solar Terrestrial Relations Observatory (STEREO) data)[1]. Using this analysis, Vasquez et al. found that the temperature at the boundary was enhanced for multiple Carrington Rotations, suggesting an efficient heating mechanism in this region. Secondly, they found density enhancements at the boundary of open and closed magnetic field. Thirdly, the density in that region falls off much more slowly with height than the streamer core, resulting in a larger density at the boundary than in the streamer above 1.2 $R_\odot$ (solar radii; measured from

[1]These density reconstructions are achieved using a model, and limitations of the model could generate artifacts or generate unphysical results.

center of the Sun). Because local electron densities are determined by the integral of the flux of dissipated Alfvén waves and the radiative heat flux along a field line, the observed electron enhancement could indicate a downward heat flux due to wave damping above. Also using LDEM reconstructions of temperature, Vásquez et al. [2011] found that small closed loops in which the temperature increased from the footpoint to apex were located near the boundary of open and closed fields, and loops which cooled were away from the boundary.

Combining all of these points suggests that some other process (aside from ion cyclotron and turbulent dissipation) could be dominant in the boundary region between open and closed magnetic fields. A mechanism which requires transverse gradients in the local Alfvén speed is surface Alfvén wave (SAW) damping. The dissipation can heat both the fast and slow solar wind, and is referred to as resonant absorption for waves moving along closed loops, and phase mixing for waves along open field lines [Ruderman et al., 1999]. Direct observations of resonant absorption have been presented along closed loops in [Aschwanden et al., 2003]. In Verth et al. [2010], Coronal Multi-channel Polarimeter (CoMP) data [Tomczyk and McIntosh, 2009] in the 1-4 mHz range along closed loops was associated with resonant absorption due to gradients in density across the loops. Verth et al. [2010] found that resonant absorption is an efficient dissipation process in this region and frequency range. To date, observational evidence along open flux tubes has not been reported. Estimations from one- and two-dimensional models for open flux tubes with prescribed magnetic field geometry and idealized solar wind parameters suggested SAW damping could be a significant heat source [Jatenco-Pereira and Opher, 1989, Narain and Sharma, 1998, Sakai et al., 2001]. Evans et al. [2009] calculated the heat deposited along open field lines due to SAW dissipation using solar wind parameters from a global MHD model and found that waves with frequencies higher than 0.28 mHz were appreciably damped with a total energy contribution that was comparable to the ad hoc heating term in Cohen et al. [2007]'s global MHD model.

In this chapter, we take two steps. First, we estimate the amount of energy available to be dissipated by SAW damping. We find that the mechanism is important along the boundary of open and closed magnetic field regions. Then, we implement SAW in a 3D global model in which wave evolution is coupled self-consistently to the MHD equations. We do so with the recently developed model of van der Holst et al. [2010]: a 3D data-driven solar wind model within the Space Weather Modeling Framework [Toth et al., 2011]. The wave pressure gradient accelerates the fast wind, and coronal heating is achieved through wave dissipation. In van der Holst et al. [2010], the wave dissipation occurred along open field lines in a manner set to mimic turbulence [Hollweg, 1986]. Here, I show that the addition of SAW dissipation results in a solar wind solution which agrees better with observations in both the lower corona and inner heliosphere.

4.2 Estimating the Importance of Surface Alfvén Wave Heating

4.2.1 Introduction

Here we investigate the contribution of surface Alfvén wave damping to the heating of the solar wind during solar minimum conditions. These waves are present in regions of strong inhomogeneities in density or magnetic field (e. g., the border between open and closed magnetic field lines). We extract magnetic field geometries from the polytropic solar wind model of Cohen et al. [2007], calculate how a spectrum of Alfven waves would be damped along those field lines between 1-4 $R_\odot$ (solar radii), the region of interest for both acceleration and coronal heating. We consider waves with frequencies lower than those that are damped in the chromosphere and on the order of those dominating the heliosphere: $3 \times 10^{-6} - 10^{-1}$ Hz. In the region between open and closed field lines, within a few $R_\odot$ of the surface, no other major source of damping has been suggested for the low frequency waves we consider here. This work is the first to study surface Alfvén waves in a 3D environment without assuming a priori a geometry of field lines or magnetic and density profiles. Next, we calculate the heating in the polytropic model due to the reduced and varying polytropic index, and compare it to the heat flux by SAW damping. We find that SAW damping can produce enough energy to heat the corona at the boundary of open and closed magnetic field lines.

Waves occur naturally as a perturbation to the MHD equations, and so their presence may be expected when solving the MHD equations. However, in global simulations waves have to be included explicitly [Usmanov and Goldstein, 2003] due to time and spatial limitations. The time step of this simulation (0.2 seconds) is less than the smallest period considered in this analysis (3 seconds). Additionally, the grid resolution is not enough to spatially resolve the waves.

4.2.2 Theory

The full derivation of dissipation due to surface Alfvén wave heating is given in Appendix B. The damping length along a magnetic field line is given by: [Jatenco-Pereira and Opher, 1989, Lee and Roberts, 1986]:

$$L_{SW} = 18\frac{v_{A0}}{\omega}\left(\frac{r_0}{r}\right)^{\frac{S}{2}}\left(\frac{v_A}{v_{A0}}\right)^2(1+M_A) \tag{4.1}$$

where $M_A = \frac{u_{SW}}{v_A}$ is the Alfvén Mach Number. The subscript 0 indicates the variable is to be evaluated at the reference height (see Appendix B). The expansion of open field lines, S, is given by $A_{cs}(r) = A_{cs}(r_0)\left(\frac{r}{r_0}\right)^{S(r)}$, where $A_{cs}(r)$ is the cross sectional area of the flux tube at distance r. A value of 2 for S indicates pure radial expansion. The lines which border closed field lines must expand superradially (open faster than radial) to fill the space above the closed loops. In studies where S is not a function of r, typical values in the lower corona are 2-6 [Jatenco-Pereira et al., 1994, Moore et al., 1991, Narain and Sharma, 1998].

We calculated S explicitly in a 3D background solar wind using the non-uniform polytropic index [Cohen et al., 2007]. We generated a background solar wind using MDI synoptic magnetogram data for CR1912 (August 1996) as a boundary condition. This timeframe was

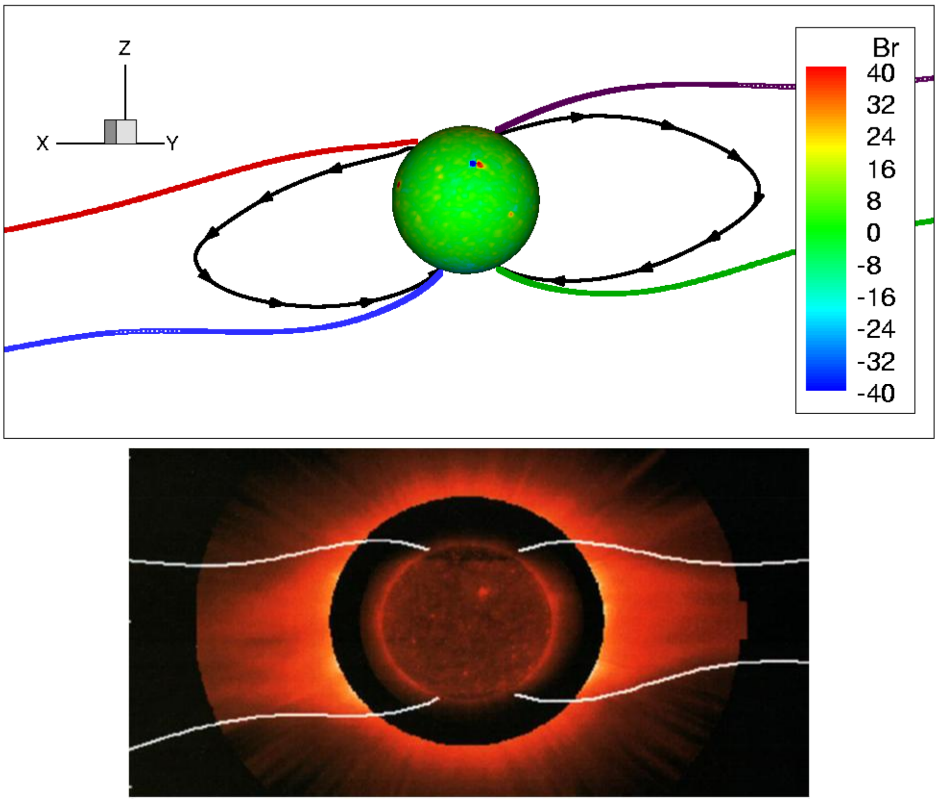

Figure 4.1: (Top) 3D coronal hole boundary field lines obtained from the simulation for 1996 August 17. The different colors refer to: red as northeast line (NE); blue as southeast line (SE); green as southwest line (SW);and purple as northwest line (NW). The black lines show closed equatorial streamers, and the arrows give the direction of the magnetic field. The solar surface is shown colored by the radial component of the magnetic field [Evans et al., 2009]. (Bottom) Coronal hole boundary field lines in the plane of the sky for 1996 August 17, as derived from SOHO UVCS observations [Dobrzycka et al., 1999].

chosen to make a direct comparison of the large-scale solar magnetic topology derived from observations during solar minimum conditions [Dobrzycka et al., 1999] (herein referred to as DO99). DO99 used an intensity increase of two emission lines from SOHO's Ultraviolet Coronagraph Spectrometer instrument to identify coronal hole boundary (CHB) latitudes as a function of height. In the simulation we identify the CHB locations by hand.

4.2.3 Results

In Figure 4.1 we show the results for the CHB field lines from (a) our MHD simulations and (b) the observations of DO99 in the plane of the sky on 17 August 1996. Although similar, we found that three out of four simulated CHB are higher in latitude compared to DO99. Also, the superradial expansion factors covered a wider range than estimated from observations. We attribute both of these to a 2D vs 3D projection effect (see Evans et al. [2009] for details of this calculation), and emphasize that simulations of surface Alfvén waves should be done in 3D.

In Figure 4.2, we plot L_{SW} which was calculated using parameters ρ, B and u_{sw} from the steady state solution. Figure 4.2a presents L_{SW} for the coronal hole boundary field lines in Figure 4.1 with frequency 4.17×10^{-3} Hz, normalized at 1.04 $R_\odot$ to the damping length (L_0) of the SW line. This normalization allows for comparison of the profile features from different source regions as a function of height. In Figure 4.2b we feature only the SW line and present L_{SW} for several frequencies, from $3.3 \times 10^{-1} - 3.8 \times 10^{-6}$ Hz. It can be seen that frequencies above 2.8×10^{-4} (short dashed line) will be appreciably damped within a few solar radii of the surface.

Figure 4.2a shows distinctly different profiles from the southern and northern CHB lines. We examined the source region of each footpoint and found that the SE and SW lines originated near small active regions in which the radial component of the magnetic field was $B_r \approx 50$ G. Both northern hemisphere lines originated from quiet sun regions ($B_r \approx 1$ G). For the SWMF and other MHD models, Evans et al. [2008] showed that the Alfvén profile will contain a maximum, or hump, if the source region is quiet sun. The profile from an active region in global models begins at a maximum value, and drops to less than a few hundred $\frac{km}{s}$ within one solar radius from the surface.

The profile of L_{SW} is controlled by the Alfvén speed profile. The normalized profiles in Figure 4.2a show that the position corresponding to $L_{SW} = 1R_\odot$ is closest to the Sun for active regions. The profiles from quiet Sun source regions have a plateau, pushing

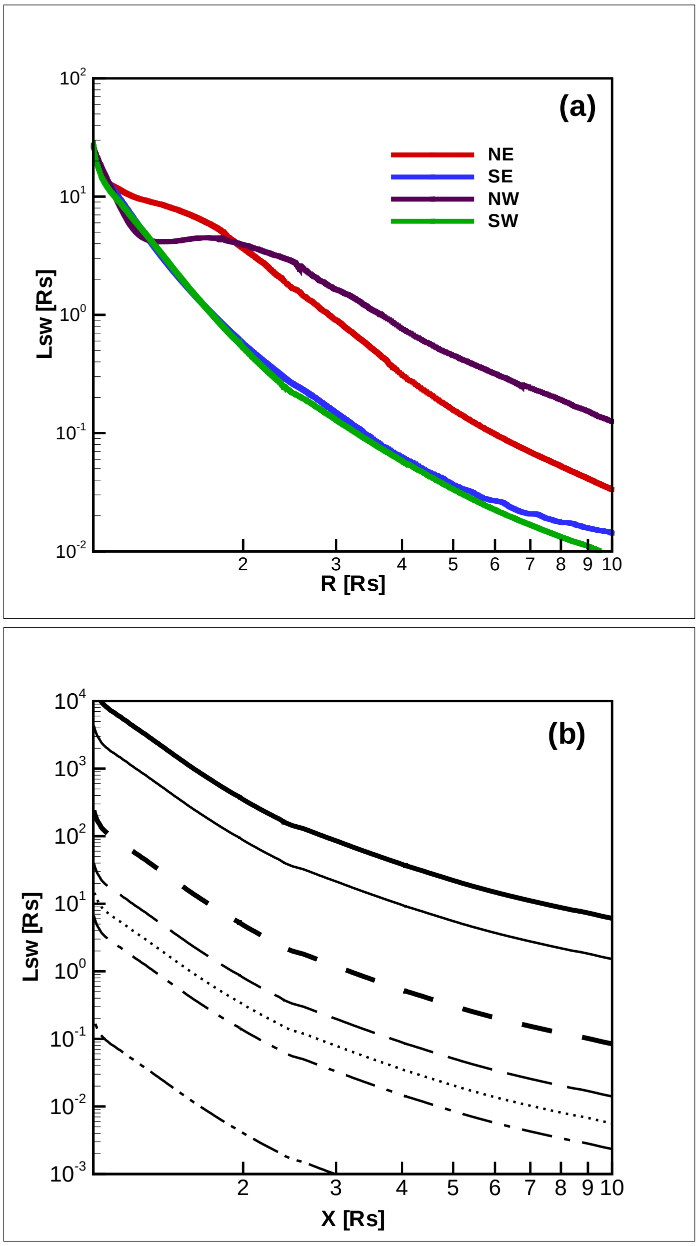

Figure 4.2: a) Surface Alfvén damping length (L_{sw}) profiles for the coronal hole boundaries in Figure 4.1 (colors correspond), normalized to the L_0 of the SW line (green) from 1.04-10 $R_{\odot}$. Note the plateau in the profiles for lines whose source region on the sun is quiet sun, differing from field lines with footpoints near active regions, whose profiles drop quickly. b) Profiles for the SW coronal hole boundary field line corresponding to different frequencies. From the bottom up to top profile: 3.3×10^{-1} Hz (dash-dot-dot line); 1×10^{-2} Hz (dash-dot line); 4.17×10^{-3} Hz (dot line); 1.67×10^{-4} Hz (long dash line); 2.8×10^{-4} Hz (short dash line); 1.5×10^{-5} Hz (thin solid line); 3.8×10^{-6} Hz (thick solid line). Waves with frequencies above 2.8×10^{-4} are appreciably damped below 4 $R_{\odot}$ [Evans et al., 2009].

$L_{SW} = 1R_\odot$ further from the Sun. The implication of this result can be seen in the equation relating the Alfvén wave energy density,

$$\epsilon_{SW} = \left(\frac{M_{A0}}{M_A}\right)\left(\frac{1+M_{A0}}{1+M_A}\right)^2 \exp\left(-\frac{r}{L_{SW}}\right). \tag{4.2}$$

If the damping length is $1R_\odot$ or less, then the waves will be damped close to the Sun. Therefore, the presence of the hump means the energy of the surface Alfvén wave can travel further into the corona before substantial damping occurs. This means that the quiet sun region will damp more surface waves at further distances, so it is more efficient in carrying the wave momentum out into the corona. Active regions will damp closest to the Sun.

Using the frequencies that are appreciably damped, we estimated how much wave energy flux would be dissipated along each field line, assuming all of the energy goes into heating the plasma. Following Jatenco-Pereira et al. [1994], we assume a spectrum of surface Alfvén waves $\phi_{AW}(\omega) = \phi_0 \left(\frac{\omega}{\bar{\omega}}\right)^{-\alpha} \frac{erg}{cm^2 sHz}$, where $\phi_0 = 1.3 \times 10^5 \frac{erg}{cm^2 sHz}$, $\bar{\omega}$ is the mean frequency in the observed range and the power index corresponding to the low frequency waves we are considering is α=0.6 [Tu et al., 1990].

Along a magnetic field line, the flux lost due to surface Alfvén wave damping is given by:

$$\phi_{lost,total} = \int_{\omega_1}^{\omega_2} \phi_0 \left(\frac{\omega}{\bar{\omega}}\right)^{-\alpha} \left[1 - \exp\left(\int_{r_1}^{r_2} -\omega \frac{r^{\frac{S}{2}} v_{A0}}{18 r_0^{\frac{S}{2}} v_A^2 (1+M_A)} dr\right)\right] d\omega \tag{4.3}$$

where the limits are $\omega_1 = 2.8 \times 10^{-4}$ Hz and $\omega_2 = 0.3$ Hz, $r_1 = 1.04R_\odot$ and $r_2 = 4R_\odot$, and the definition of L_{sw} from Eq. B.35 has been included (v_A, S, M_A, are all functions of r.) (See Evans et al. [2009] for a full derivation of this expression.)

The range of $\phi_{lost,total}$ values for the field lines in Figure 4.1 were 6.1-6.4 $\times 10^4$ $ergs/cms$. To determine whether this energy flux is enough to match the coronal heating due to the variable polytropic index, we estimated its contribution to the heating along a field line.

From the first law of thermodynamics, with the ideal gas law and assuming that the ratio of specific heats is a constant, one can derive a polytropic equation,

$$\frac{p}{\rho^{\alpha}} = const. \tag{4.4}$$

where α is referred to as the polytropic index. The notation stems from Parker [1963] to clarify that this index can (but need not) be the ratio of specific heats, and that we are not necessarily considering an adiabatic process. The symbol γ is typically used for the ratio of specific heats, and in the case of an adiabatic expansion (no heat enters or leaves the system), $\alpha = \gamma = \frac{5}{3}$. An isothermal wind expansion would be characterized by $\alpha = 1$. Observations of the solar wind have indicated that α=1.46-1.58 in the heliosphere [Totten et al., 1995]. A value closer to unity is adopted in some global MHD models in the region near the Sun in order to generate fast solar wind and match temperature observations in the heliosphere [Usmanov and Goldstein, 2003].

All previous discussion made the underlying assumption that α was constant with height. If that condition is not met, then the polytropic index is referred to as an effective (or local) polytropic index and written as Γ [Totten et al., 1995]. The polytropic equation (Eq. 4.4) is modified to

$$\frac{dlnP}{dr} = \Gamma\frac{dln\rho}{dr} + ln\rho\frac{d\Gamma}{dr} \tag{4.5}$$

such that the relationship between density and pressure is not simple.

In a steady state (i. e. no time dependence) simulation with a fixed, constant $\alpha = \gamma$, the conservation of energy can be written as [Manchester et al., 2004]:

$$\nabla \cdot \left[\mathbf{u}\left(\frac{\gamma p}{\gamma - 1} + \frac{\rho u^2}{2} + \frac{B^2}{4\pi}\right) - \frac{(\mathbf{u}\cdot\mathbf{B})\,\mathbf{B}}{4\pi}\right] = \rho\mathbf{g}\cdot\mathbf{u} + q. \tag{4.6}$$

The heating function q can take different forms, for example an exponential dependent on magnetic field strength and distance from the Sun [Groth et al., 2000]. In the polytropic model of Cohen et al. [2007], there is no q and the ratio of specific heats γ is replaced by the effective polytropic index Γ,

$$\nabla \cdot \left[\mathbf{u} \left(\frac{\Gamma p}{\Gamma - 1} + \frac{\rho u^2}{2} + \frac{B^2}{4\pi} \right) - \frac{(\mathbf{u} \cdot \mathbf{B})\,\mathbf{B}}{4\pi} \right] = \rho \mathbf{g} \cdot \mathbf{u}. \tag{4.7}$$

Although Γ has both latitudinal and azimuthal dependence below 4 $R_\odot$, in [Evans et al., 2009] we considered only the radial variation, and so we replace ∇ by $\frac{d}{dr}$. We assume that the exact same solar wind solution is produced by the two energy equations (one with a variable polytropic index and one with an additional volumetric heating function and $\gamma = \frac{5}{3}$). To quantify the amount of heating in the polytropic model, we subtract Eq. 4.7 from Eq. 4.6, and integrate along a magnetic field line between r_1=1.04 $R_\odot$ and r_2=4 $R_\odot$:

$$Q = \int_{r_1}^{r_2} - \left[\frac{d\,(u_r p)}{dr} \left(\frac{\Gamma}{\Gamma - 1} - \frac{\gamma}{\gamma - 1} \right) - \left(\frac{d\Gamma}{dr} \frac{u_r p}{(\Gamma - 1)^2} \right) \right] dr \frac{erg}{cm^2 s}. \tag{4.8}$$

See Evans et al. [2009] for more details. The range of values for Q for the four field lines in Figure 4.1 is 8 $\times 10^3$-3 $\times 10^5$ erg/cms . The energy flux from the dissipated waves is therefore comparable to the heating due to the variable polytropic index along field lines at the boundary of open and closed magnetic fields. It is important to stress that this study [Evans et al., 2009] was not self-consistent - we did not consider any back effects on the waves from the plasma.

4.3 Implementation in a Wave-Driven Model

In this section we present the new solar corona (SC) component of the SWMF. In it, the wave transport equation describing low frequency waves [Jacques, 1977, Sokolov et al., 2009] is coupled to the MHD equations for the solar wind [van der Holst et al., 2010]. The wave pressure gradient accelerates the wind, and coronal heating is achieved through wave dissipation. The van der Holst et al. [2010] model considers a flat (or gray) spectrum of waves. Our contribution to the model is the implementation of surface Alfvén wave damping. The estimations from the previous section suggested that SAW damping would be an important heating mechanism, and in this work we show that surface Alfvén waves brings the model better in agreement with observations both near the Sun and in the heliosphere.

4.3.1 Methodology and Simulation Details

In the low frequency, Wenztel-Kramers-Brillouin limit, MHD waves are treated as wave train packets [Dewar, 1970, Jacques, 1977, Sokolov et al., 2009]. The wave energy flux can be expressed generally as:

$$\mathbf{F} = \mathbf{V_g} E_W + \mathbf{u} \cdot \mathbf{P_W} \tag{4.9}$$

where E_W is the wave energy density, $\mathbf{u}$ is the bulk fluid velocity, bf Pw is the wave pressure tensor, and V_g is the group velocity,

$$\mathbf{V_g} = \frac{\partial \omega}{\partial \mathbf{k}} = \frac{\partial \omega_0}{\partial \mathbf{k}} + \mathbf{u} = \mathbf{V_{g0}} + \mathbf{u} \tag{4.10}$$

where ω is the frequency in the moving frame (subscript 0 in intertial frame), $\mathbf{k}$ is the wave number. In the case of a transverse Alfvén wave, $V_{g0}= v_A$. The wave energy density can be written as

$$E_W = \frac{1}{2}\rho\omega_0^2 a^2 \tag{4.11}$$

where a is the wave amplitude. This expression is valid for all wave modes.

For low frequency Alfvén waves, the pressure tensor is isotropic and can be written simply as

$$P_W = \frac{1}{2} E_W. \tag{4.12}$$

In the case of an expanding atmosphere with no wave dissipation, the wave transport equation is written as [Jacques, 1977],

$$\frac{dE_W}{dt} + \nabla \cdot \mathbf{F} = \mathbf{u} \cdot (\nabla P_W) \tag{4.13}$$

The wave energy in an accelerating medium is not conserved: the term on the right hand side is the rate of work done by the waves on the flow. The quantity which is conserved is the wave action,

$$S = \frac{E_W}{\omega_0}. \tag{4.14}$$

However, when wave dissipation is considered (by including the term $-\Gamma E_W$ on the right hand side of Equation 4.13, where Γ is the dissipation rate), S is no longer conserved.

In the current treatment [van der Holst et al., 2010], all waves are outgoing (anti-Sunward), launched from the inner boundary. (Boundary conditions will be described in detail below). In this configuration, two different Alfvén wave energy densities are defined: E_W^+, launched from a location where the magnetic field is positively radial (and therefore having velocity $+v_A$; $v_A = \frac{B}{\sqrt{4\pi\rho}}$), and E_W^-, launched where the magnetic field is negatively radial ($-v_A$). The spectral evolution of Alfvén waves is currently under development [Oran et al., 2010]. Therefore, the waves are modeled as a flat (or gray) spectrum in this work.

The transport equation for each wave energy density can be written as

$$\frac{\partial E_W^\pm}{\partial t} + \nabla \cdot \left[(\mathbf{u} \pm \mathbf{b} v_A) E_W^\pm \right] - \frac{1}{2} E_W^\pm (\nabla \cdot \mathbf{u}) = -\Gamma_\pm E_W^\pm \tag{4.15}$$

u is the solar wind velocity, b is a unit vector along the magnetic field, v_A is the Alfvén speed

(B is the magnetic field strength, and ρ is the mass density), and Γ is the wave dissipation term. The negative sign on the left hand side indicates wave dissipation only (no growth considered). The waves are coupled to plasma via the MHD energy equation,

$$\frac{\partial E_b}{\partial t} + \nabla \cdot E_b \mathbf{u} + (\gamma - 1) E_b \nabla \cdot \mathbf{u} = \Gamma_+ E_W^+ + \Gamma_- E_W^- \tag{4.16}$$

and the momentum equation,

$$\frac{\partial (\rho \mathbf{u})}{\partial t} + \nabla \cdot \left(\rho \mathbf{u}\mathbf{u} - \mathbf{B}\mathbf{B} + \left(p + \frac{B^2}{2} \right) \mathbf{I} \right) = -\nabla p_W - \rho \frac{G M_\odot}{r^2} \mathbf{e_r} \tag{4.17}$$

where E_b is the energy density of the background plasma, P_W is the wave pressure ($= \frac{E_w}{2}$; [Jacques, 1977]), and γ is the polytropic index (set to the adiabatic value of 5/3). The equations of mass continuity, magnetic induction (for ideal MHD), and the divergenceless of $\mathbf{B}$ close the system. The reader is referred to van der Holst et al. [2010] for more details.

For this work, the crucial term is the one which describes the wave dissipation, Γ. It can be expressed generally as

$$\Gamma = \frac{v_g}{L} \tag{4.18}$$

where v_g is the group velocity of the Alfvén wave ($v_g = u \pm v_A$) and L is the damping length scale for the dissipation mechanism.

As shown in Appendix B, under the condition of a strong transverse gradient, the damping rate for surface Alfvén waves can be expressed as in [Hasegawa and Uberoi, 1982, Lee and Roberts, 1986],

$$\Gamma_{SW} = \pi (\bar{k} a) \left(\frac{\omega_2^2 - \omega_1^2}{8 \omega_0} \right) \tag{4.19}$$

where $\bar{k}$ is the average wave number. The subscript SW stands for surface wave.

To implement SAW dissipation into a global model, we consider gradients in density and write Eq. B.34 as,

$$\Gamma_{SW\pm,i} = \frac{v_{g,i,\pm}}{\frac{C'_{SW}}{\omega}\frac{\rho}{\sqrt{\left(\frac{\partial\rho}{\partial x_j}\right)^2+\left(\frac{\partial\rho}{\partial x_k}\right)^2}}} \tag{4.20}$$

where C_{SW} controls the damping strength, and i, j and k represent the x, y and z directions. It is assumed that the wave polarization (δB) is in the direction perpendicular to the resonant layer. This equation captures the behavior of the mechanism: inversely proportional to frequency, and characterized by transverse gradients in density. It should be emphasized that this phenomenological form for the dissipation is in agreement with that which was formally derived in the thin tube (strong gradient) limit [Terradas et al., 2010].

In this paper, Alfvén waves are modeled as a flat (or gray) spectrum, so the frequency dependence in Eq. 4.21 is absorbed into the free parameter ($C_{SW} = \frac{C'_{SW}}{\omega}$). SAW dissipation applies in all regions, and so Γ_{SW} is calculated at each spatial location for all waves, and at each iteration the waves are dissipated. The dissipated wave energy is passed to the plasma (as in Eq. 4.16), so that the total energy (waves and plasma) is conserved.

An LDEM reconstruction of electron density [Vásquez et al., 2010] from $R = 1.035 - 1.225R_\odot$ was used to verify that the gradients in the simulations were reasonable. Although the simulation does not resolve small scale features present in the LDEM reconstructions, the order of magnitude and distribution of the gradients in the simulation are in agreement with the those calculated using the LDEM reconstructions.

Although we do not treat a spectrum of waves, we can estimate the frequency range for which this treatment is valid. The condition of strong damping ($ka < 0.1$) is estimated by

$$ka \approx \frac{\omega}{v_a}\frac{\rho}{\frac{d\rho}{dx}} < 0.1. \tag{4.21}$$

This condition is satisfied in our simulation for $\omega \leq 13mHz$. This estimated frequency limit is within the range found to be important for SAW damping in Evans et al. [2009]

($\omega \geq 0.28 mHz$), and those observed along closed loops in Verth et al. [2010] (1-4 mHz).

The inner boundary condition for the radial component of the magnetic field is specified from the National Solar Observatory's Global Oscillation Network Group (GONG) magnetogram data for Carrington Rotation 2077 (2008 November-December), as shown in Figure 4.3a). The magnetogram data was multiplied by a factor 1.8 due to the low spatial resolution of GONG [Cohen et al., 2007]. The initial condition for the magnetic field is calculated with the Potential Field Source Surface (PFSS) model [Altschuler and Newkirk, 1969]. The inner boundary condition for the solar wind temperature and density (shown in Figure 4.3b) and c)) were specified using LDEM reconstructions [Vásquez et al., 2010] for the same time period as the magnetogram data. The initial conditions for the single-fluid plasma density and solar wind speed are given by the isothermal Parker solar wind solution [Parker, 1958].

The wave energy density at the inner boundary is set to zero for all closed magnetic field lines (as determined by the PFSS model). For open field lines, a purely anti-sunward (outgoing) wave energy density is specified using conservation of energy along a magnetic flux tube with the Bernoulli integral [Suzuki and Inutsuka, 2006]. At 1 AU, the solar wind energy is assumed to be purely kinetic, with a velocity calculated using the Wang-Sheeley-Arge (WSA) model [Arge et al., 2003]. This allows the wave energy input at the boundary to be calculated according to

$$E_W^{\pm} = \frac{(\rho u r^2)_{1AU}}{r^2} \frac{f_{exp}}{|v_{A,r}|} \left(\frac{u_{WSA}^2}{2} + \frac{GM_\odot}{R_\odot} - \frac{\gamma}{\gamma - 1} \frac{p}{\rho} \right) \tag{4.22}$$

where u_{WSA} is the solar wind velocity at 1 AU obtained using the WSA model, γ is the polytropic index (set to 5/3), f_{exp} is the expansion factor for the magnetic field line, and ρu is the mass flux at 1 AU. The mass flux in the fast solar wind is constrained with Ulysses data (see van der Holst et al. [2010] for details). The wave pressure ($= \frac{E_W}{2}$) is shown in Figure 4.3d), and ranges from 0 to 0.0015 $\frac{dyn}{cm^2}$.

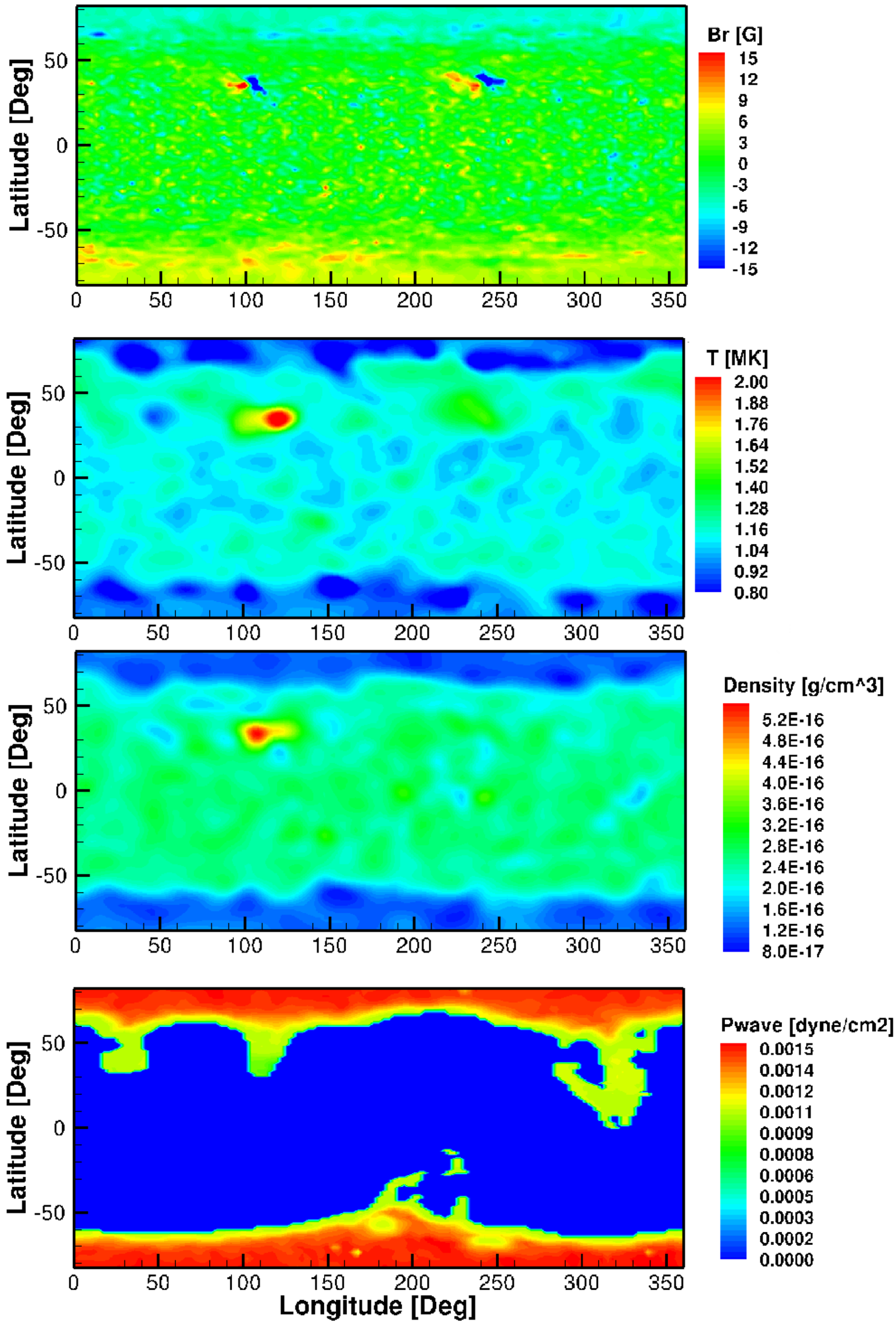

Figure 4.3: Carrington maps showing the inner boundary conditions used in the simulations: a) radial magnetic field, derived from a GONG synoptic magnetogram for CR2077; b) solar wind temperature and c) density, both reconstructed using the LDEM technique for CR2077; and d) Alfvén wave pressure, calculated using the Bernoulli integral [Evans et al., 2011b]. See text for details.

In addition to SAW damping, we will use turbulent dissipation (as implemented in van der Holst et al. [2010], following Hollweg [1986]) We explore both mechanisms individually, and in combination. The damping rate for each can be written as:

$$\Gamma_{SW\pm} = \frac{v_{g,\pm}}{C_{SW}\frac{\rho}{\delta_{\perp}\rho}} \tag{4.23}$$

$$\Gamma_{TUR\pm} = L_{TUR}\sqrt{\frac{E_W^{\pm}B}{\rho}} \tag{4.24}$$

The free parameters which control the strength of the dissipation are: L_{TUR} for turbulent dissipation, and C_{SW} for surface Alfvén wave damping. The values were chosen to obtain a maximum fast solar wind velocity of $750\frac{km}{s}$ at 0.1 AU. The values for each were: simulation with only turblent dissipation, $L_{TUR} = 2.1R_{\odot}$; simulation with only SAW, $C_{SW} = 10$; and simulation with both mechanisms, $L_{TUR} = 10.3R_{\odot}$ and $C_{SW} = 12$. In the simulation with both mechanisms, we lowered the SAW dissipation rate by 20% and then fixed L_{TUR} with the solar wind velocity. This is not a unique solution (see Appendix B).

The computational domain is a Sun-centered $48 \times 48 \times 48$ $R_{\odot}$ cartesian grid of blocks composed of $4 \times 4 \times 4$ cells. There are 6 levels of refinement, with a smallest cell size of 3/128 $R_{\odot}$ in a shell of thickness 0.3 $R_{\odot}$ at the inner boundary. The heliospheric current sheet is refined to 3/32 $R_{\odot}$. The total number of cells in the simulation are 2.4×10^6.

4.3.2 Results

In this section we present the results of three simulations: one for each dissipation mechanism individually, and one which included both surface Alfvén wave and turbulent dissipation. All simulations have the same boundary conditions. First we present the large-scale simulation results, and then we look specifically at the region in the very low corona (R$\leq 1.225R\odot$)at the boundary of open and closed fields. We include LDEM reconstructions and Ulysses data as evidence that surface Alfvén wave dissipation occurs and is important. Finally, we compare the Alfvén speed profile from the new solar wind model to the previous solar wind model in the SWMF, and discuss the implications for modeling shock formation and evolution.

4.3.3 Inner Heliosphere

In Figure 4.4 the dissipation rate for waves (Γ as defined in Eqs 4.23 and 4.24) is shown in meridional slices. The values for surface Alfvén wave dissipation are shown in a) and b); turbulent dissipation is shown in c) and d). Panels a) and c) correspond to waves traveling along the magnetic field, and opposite is shown in panels b) and d). The magnetic field projected onto the plane is shown as black lines.

Although we parameterized the form of the surface Alfvén wave damping rate, the chosen expression reproduces the expected behavior of the mechanism. Radial and latitudinal gradients in density create dissipation along mid-latitude (40-70°) open magnetic field lines between 1-2.5 $R_{\odot}$. We expect dissipation in this region due to the superradial expansion of the magnetic field, which is reproduced well by density gradients. Also as expected, there is reduced dissipation above the poles, where the field line expansion is radial. Latitudinal gradients in density produce surface Alfvén wave dissipation near the solar surface at the boundary of the open and and closed magnetic field lines, and extends out into the corona surrounding the current sheet. Turbulent dissipation occurs mostly at high latitudes between 1-4 $R_{\odot}$, where the magnetic field (and thus the wave energy density) is largest.

For both mechanisms, the dissipation rate differs for the two waves in the simulation (traveling along or opposite to the magnetic field). For the turbulent dissipation, this is due to the dependence of Γ on the wave energy density. For surface Alfvén wave damping, this occurs due to the dependence on the group velocity of the wave.

Figure 4.5 shows the steady state solar wind temperature at $R = 0.1AU$. The panels correspond to simulations with different wave dissipation choices: a) turbulent dissipation only; b) surface Alfvén wave dissipation only; and c) combination of both mechanisms. The

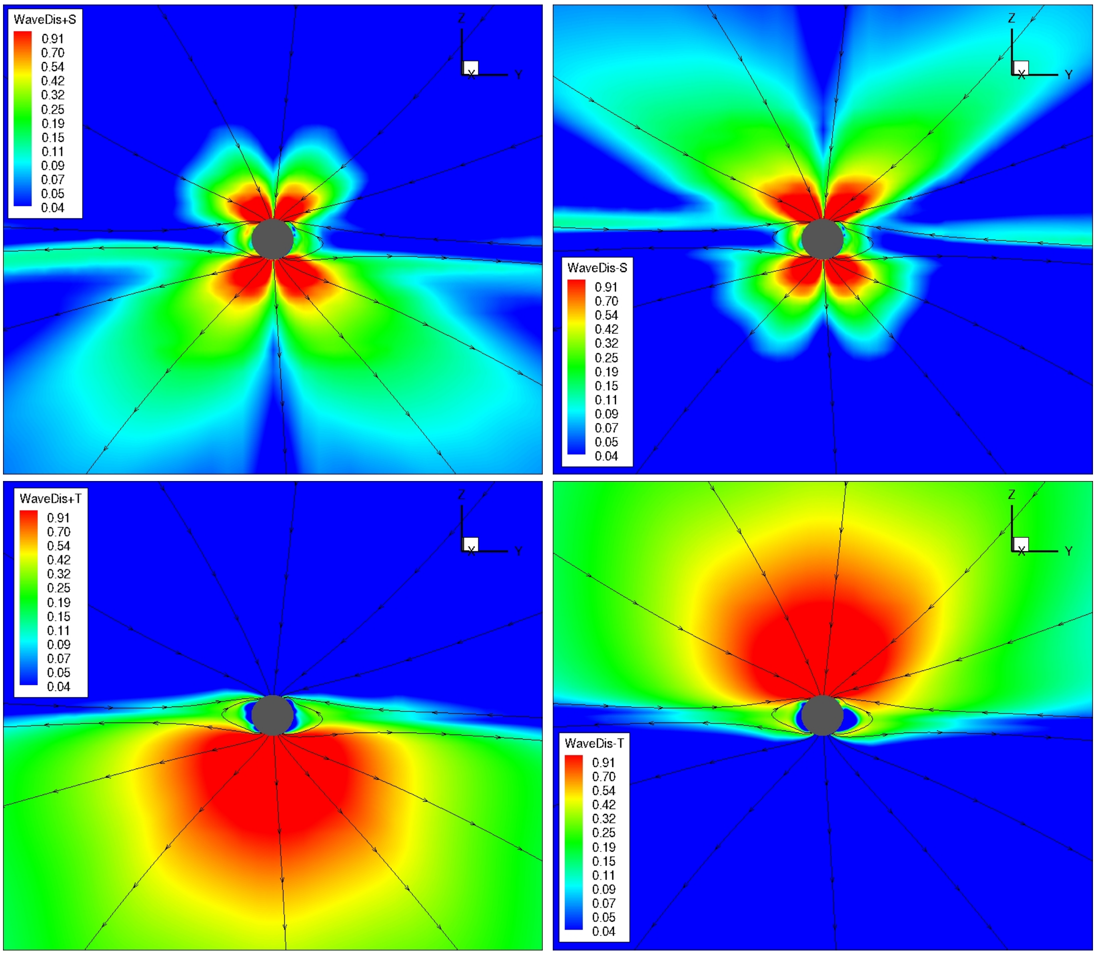

Figure 4.4: Meridional slices of the dissipation rate for waves, Γ. The values for surface Alfvén wave dissipation are shown in a) and b); turbulent dissipation is shown in c) and d). Panels a) and c) correspond to waves traveling along the magnetic field, and opposite is shown in panels b) and d). The magnetic field projected onto the plane is shown as black lines. The gray circle defines the inner boundary ($R = 1.035\ R_{\odot}$) [Evans et al., 2011b].

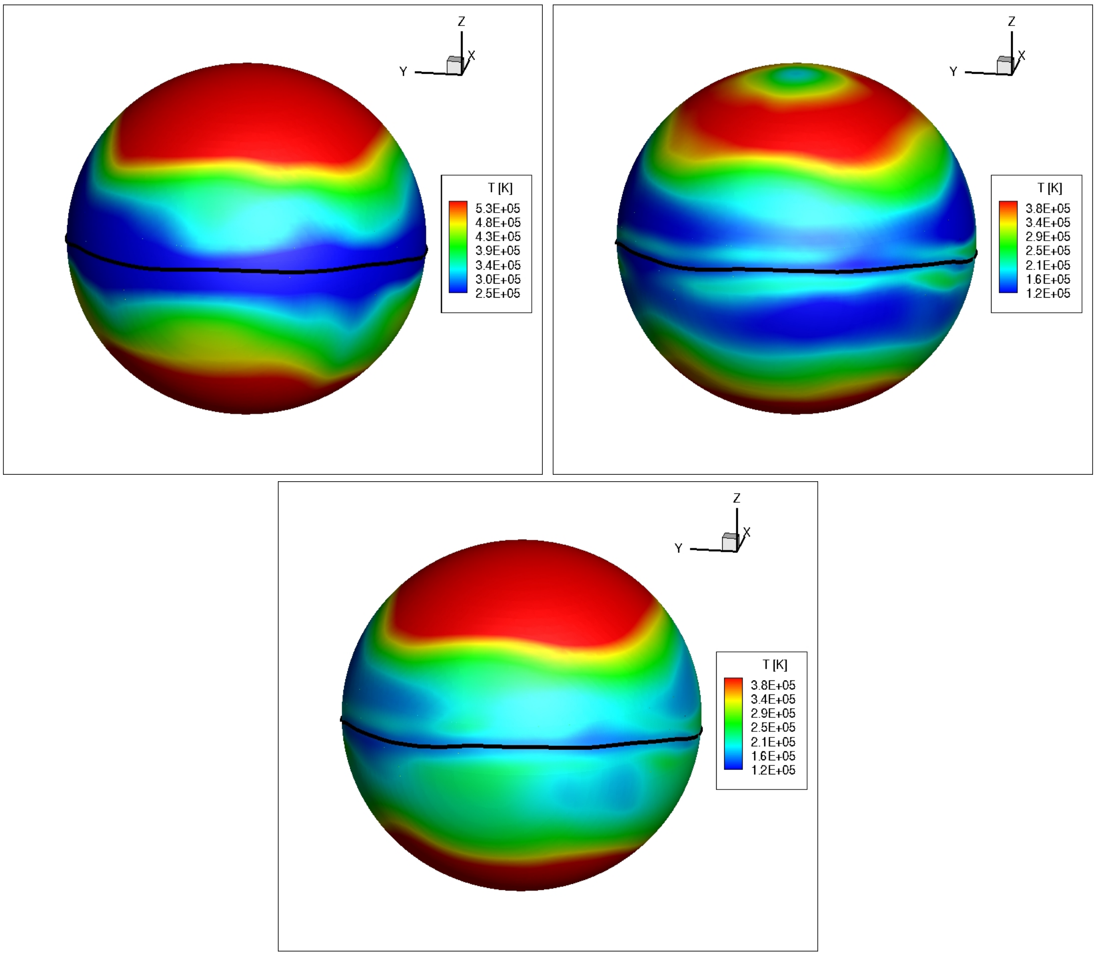

Figure 4.5: The steady state solar wind temperature at R=0.1 AU is shown in all panels. The panels correspond to simulations with different wave dissipation choices: a) turbulent dissipation only; b) surface Alfvén wave dissipation only; and c) combination of SAW and turbulent dissipation. The thick black line marks the location of the heliospheric current sheet [Evans et al., 2011b].

turbulent dissipation provides most of the heating directly above the poles, and because it scales with the magnetic field, produces a temperature minimum at the heliospheric current sheet. Surface Alfvén wave dissipation provides heating in two locations: the subpolar superradially expanding open field lines, and at the boundary between open and closed magnetic fields. Combining the mechanisms (Figure 4.5c) results in strong heating at high latitudes, including low (subpolar) latitude heating from SAW, and around the HCS (also due to SAW).

The temperature profile when both dissipation mechanisms are used is most aligned with observations (details of observations in Appendix C). First, heating which is observed around the HCS is reproduced by SAW dissipation (although in the literature it has been attributed to turbulence). Second, using ion temperature data measured during the first fast latitude scan of Ulysses, we calculated scaled latitudinal temperature distribution in the fast solar wind at 1 AU. The slope of this data (when a linear fit was applied) increases in the direction from the pole towards the equator. This suggests that there could be a heating mechanism at work in the solar wind which is efficient at the boundary between fast and slow solar wind (or, at the Sun between open and closed magnetic fields). The sharp transition between fast and slow solar wind measured by Ulysses is not reproduced in the model; in all simulations the transition occurs over $25°$ of latitude.

In Figure 4.6, we show the large-scale solar wind structure from a simulation in which both SAW and turbulent dissipation were used. The meridional slice gives the magnitude of the solar wind speed. The scale is -24 to 24 $R_\odot$ in each direction. The sphere represents the inner boundary, from which selected magnetic field lines are drawn (shown in black). The color contour on the solar surface is the radial magnetic field, with the colorbar corresponding to Figure 4.3a). The model produces a bimodal solar wind through the wave pressure gradient, which accelerates the fast solar wind. This bimodal wind is achieved independent of the wave dissipation mechanism [van der Holst et al., 2010]. However, the dissipation rate does affect the magnitude of the solar wind speed (see discussion in Appendix B).

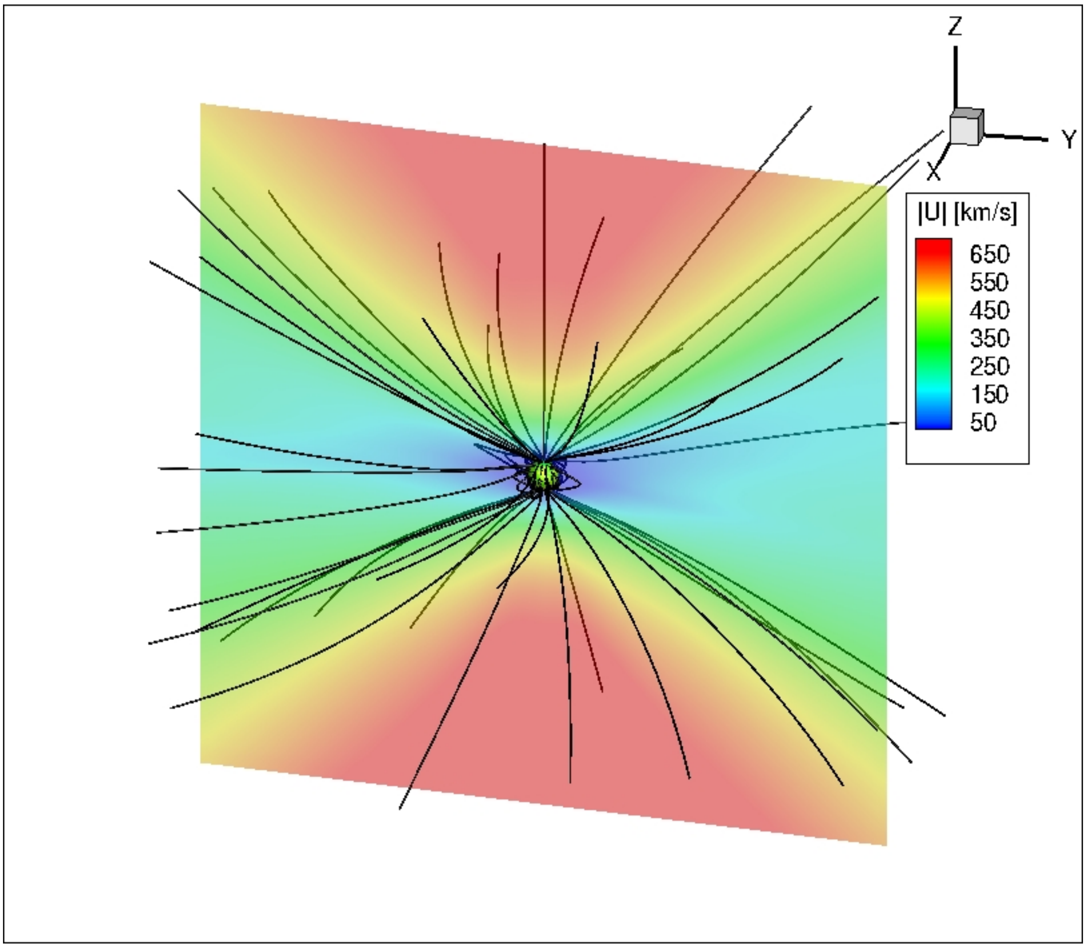

Figure 4.6: Large-scale solar wind structure is shown. The meridional slice gives the magnitude of the solar wind speed. The scale is -24 to 24 Rs in each direction. The sphere represents the inner boundary, from which selected magnetic field lines are drawn (shown in black). The color contour on the solar surface is the radial magnetic field, with the colorbar corresponding to Figure 4.3a) [Evans et al., 2011b].

4.3.4 Very Low Corona

In Figure 4.7, meridional slices containing two sets of temperature data are shown. The panels correspond to simulations with different wave dissipation choices: a) turbulent dissipation only; b) surface Alfvén wave dissipation only; and c) combination of both mechanisms. The gray circle marks the inner boundary of the simulation (1.035 $R_{\odot}$. Between the gray circle and the white ring, the temperature plotted is the electron temperature reconstructed using the LDEM technique for CR2077 (the same timeframe as the data used for the inner boundary of the simulations; Vásquez et al. [2010]). The white spots in LDEM data indicate locations where the reconstruction failed. This failure could be due to time dependent phenomena. Beyond the white ring, the simulation temperature is plotted. The magnetic field projected onto the plane is shown as black lines.

The white arrows in Figure 4.7 mark the regions of high temperature present at the boundary of open/closed magnetic field in the LDEM data. These hot spots are well reproduced by surface Alfvén wave dissipation (see Figure 4.7b.

Additionally, a study of temperature variations along closed loops with apex height less than 1.225 $R_{\odot}$ by Vásquez et al. [2011] found that loops could have temperature profiles which increased or decreased from footpoint to apex. However, they found that the loops in which the temperature increased with height were located near the boundary of open and closed fields lines. Although we did not treat wave dissipation along closed field lines in this study, it has been established that resonant absorption occurs and is efficient at heating closed loops [Aschwanden et al., 2003, Sakai et al., 2001, Verth et al., 2010]. This aspect will be pursued in a future study.

4.3.5 Profile of Alfvén Speed

Observations of energetic electrons and type II radio bursts indicate that CME-driven shocks can accelerate particles very close to the Sun [Klassen et al., 2002]. It is well established that CMEs drive shocks at larger distances [Claßen and Aurass, 2002, Gopalswamy and

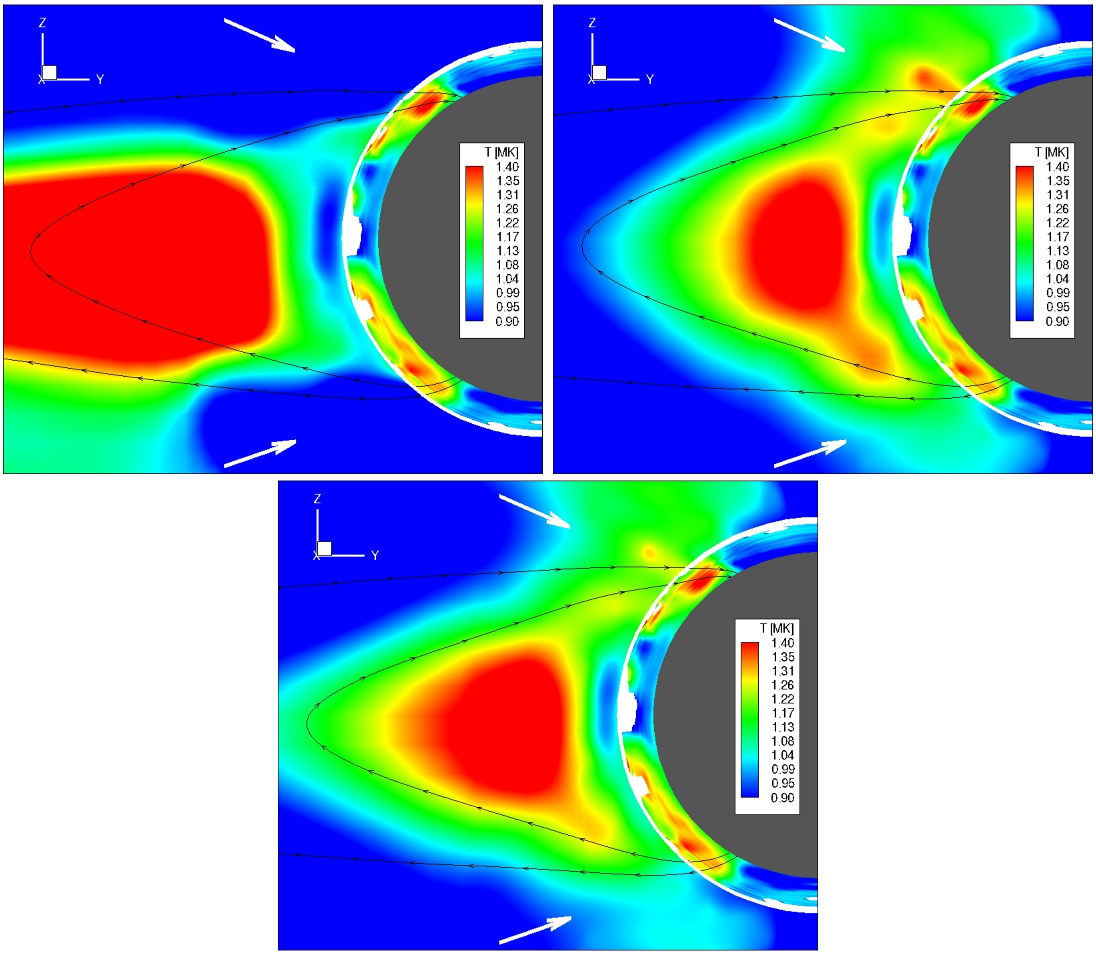

Figure 4.7: Meridional slices containing two sets of temperature data are shown. The grey sphere marks the inner boundary of the simulation (1.035 $R_{\odot}$. Between the grey circle and the white ring, the temperature plotted is the electron temperature reconstructed using the LDEM technique for CR2077. Beyond the white ring, the simulation temperature is plotted. The panels correspond to simulations with different wave dissipation choices: a) turbulent dissipation only; b) surface Alfvén wave dissipation only; and c) combination of both SAW and turbulent dissipation. The magnetic field projected onto the plane is shown as black lines. The white arrows mark "hot spots" which are present in the LDEM data and surface Alfvén wave simulations [Evans et al., 2011b].

Kaiser, 2002]. However, there appears to be a disconnect between the lower corona and interplanetary shocks [Cane and Erickson, 2005]. Gopalswamy et al. [2001] and Mann et al. [2003] (among others) claim that the explanation for the observations is a maximum (or "hump") in the Alfvén speed profile, combined with a CME velocity profile with acceleration low in the corona. The scenario would be that CMEs can drive strong shocks close to the Sun which then dissipate around 4 $R_{\odot}$ due to the maximum in the Alfvén profile. The shock could form again above 6-10 $R_{\odot}$ and propagate through the heliosphere.

In Evans et al. [2008], we presented Alfvén speed profiles from several solar wind models. It was found that global MHD models with ad hoc heating generated an Alfvén speed profile which was too flat, allowing even slow disturbances to drive strong shocks in the lower corona, which would continue as interplanetary shocks (in contrast with observations which suggest that the shock dissipate and form again). Evans et al. [2008] showed that 1D models which included Alfvén waves and physically motivated Alfvén wave dissipation produced steepened Alfvén profiles, resulting in shock dissipation, which better aligned with the observations. As a result of the study, Evans et al. [2008] proposed that the inclusion of Alfvén waves with physically motivated dissipation (which is presented in this work) would steepen the Alfvén speed profile in a global MHD model.

Figure 4.8 shows Alfvén speed profile with radial distance from an active region. The black line was calculated from the semi-empircal model presented in [Mann et al., 2003], specific to the same active region as in the simulation (see Appendix C for details of the model). The blue line was taken from the simulation in this paper with both surface Alfvén wave and turbulent dissipation. The red line was taken from a simulation using the model of Cohen et al. [2007], in which the solar wind is heated by a spatially varying polytropic index. As proposed in Evans et al. [2008], the profile of the Alfvén speed was significantly steepened by the inclusion of waves: the slope from the valley to the hump is 139 km/s/Rsun for the Alfvén wave simulation, and 70 km/s/Rsun for the polytropic simulation. Also, the value at the hump for the Alfvén speed is over 500 km/s for the wave-driven model, more than 150 km/s larger than the hump in the polytropic profile. The speed at the valley for

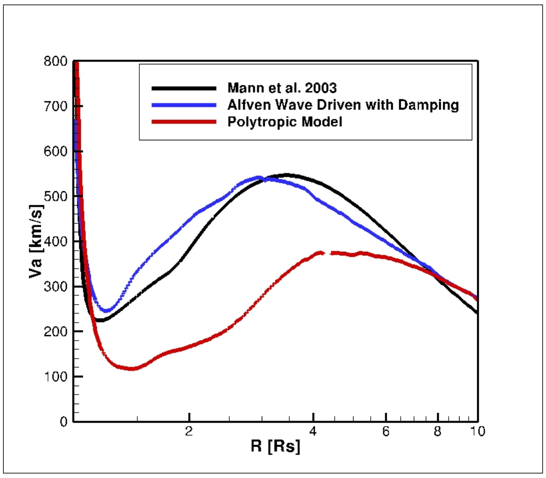

Figure 4.8: Alfvén speed profile with radial distance from an active region. The black line was calculated from the semi-empircal model presented in Mann et al. 2003. The blue line was taken from the simulation in this paper with both surface Alfvén wave and turbulent dissipation. The red line was taken from a simulation using the model of [Cohen et al., 2007], in which the solar wind is heated by a spatially varying polytropic index [Evans et al., 2011b].

the polytropic model is less than 150 km/s, whereas the wave-driven Alfvén speed is less than 300 km/s over only a short distance. The wave-driven profile inhibits shock formation by low velocity (<300 km/s) drivers.

4.4 Discussion

The work presented in this chapter was motivated by the work presented in Chapters 2 and 3. We showed how the artificial heating utilized in polytropic solar wind models lead to a lower corona environment which was not in agreement with observations of shocks, and that local models which included physically motivated Alfvén wave dissipation were.

In this first part of this chapter, we estimated the effect of surface Alfvén wave damping in heating the solar wind in the lower corona. We found that it could provide sufficient heating at the boundary of open and closed magnetic fields. We considered a spectrum of waves in the frequency range 3.8×10^{-6} to 3.3×10^{-1} Hz [Cranmer and van Ballegooijen, 2005]. We found that waves with frequency above 2.8×10^{-4} Hz would be appreciably damped below $4R_{\odot}$. The mHz range is observed along closed loops, and it has been confirmed that SAW damping is an efficient process in this range [Verth et al., 2010].

Motivated by these results, we made the first self-consistent implementation of surface Alfvén wave damping into a global MHD model. What distinguishes the solar wind model presented in this paper from others in the literature is the combination of: 1) data-driven boundary conditions, 2) a momentum source of wave pressure, and 3) the self-consistent calculation of an additional non-MHD energy source through physically motivated wave dissipation. Although several global models now apply complex energy equations which treat physical processes such as electron heat conduction and radiative cooling, all include empirical heating functions to achieve coronal heating [Airapetian et al., 2011, Downs et al., 2010, Lionello et al., 2009, Riley et al., 2011, Usmanov et al., 2011]. The physically motivated wave dissipation presented here removes the need for ad-hoc coronal heating terms. However, the surface Alfvén wave dissipation presented in this paper was calculated with a phenomenological dissipation rate, which contains one free parameter. We constrained this parameter using the fast solar wind speed.

Including surface Alfvén wave dissipation in the model of [van der Holst et al., 2010] improved agreement with observations of coronal temperature both near the Sun and in the inner heliosphere. The electron temperature in the very low corona ($R < 1.225R_{\odot}$) from LDEM reconstructions has been shown to feature "hot spots" at the boundary of open and closed magnetic fields. The simulation with SAW produces hot spots which match the LDEM data, both in location and magnitude. In the heliosphere, we have argued that a fit of the scaled Ulysses temperature data showed enhanced temperature at the boundary of fast and slow solar wind, which is a signature of SAW dissipation. However, surface Alfvén waves alone cannot reproduce the high temperature structure in the open field regions, as they do not heat directly above the poles. It should be combined with other mechanisms.

A temperature maximum at the boundary of fast and slow wind in the heliosphere has also been shown in Usmanov et al. [2011]. That model coupled the large-scale solar wind to turbulence equations in the super-Alfvénic limit; the inner boundary at 0.3 AU. The temperature maximum in that simulation was due to a maximum in the turbulent energy at the boundary, driven by strong stream shears.

We also demonstrated that the inclusion of SAW dissipation improved the usability of the solar wind model in time-dependent phenomenon. As proposed in Evans et al. [2008], the inclusion of Alfvén waves with a physically motivated dissipation mechanism steepened the Alfvén speed profile in the lower corona, aligning the Alfvén profile better with observational constraints. This improved Alfvén profile makes this model a more viable solar wind background in which to simulate CME-driven shocks than a polytropic solar wind model. Future missions, such as Solar Probe Plus, will provide even stronger constraints for wave dissipation by sampling the lower corona environment directly.

The next step in developing a physically-motivated solar wind is to treat wave spectral evolution. This aspect has been implemented in a 2.5D stellar wind model [Airapetian et al., 2010], and is under development in the SWMF [Oran et al., 2010]. A spectrum of Alfvén waves is crucial to the implementation of ion-cyclotron damping, thought to be prevalent in coronal holes [Chandran et al., 2010, Cranmer et al., 1999, Isenberg et al., 2001]. Additionally, relaxing the WKB limit (to account for counter-streaming waves) will allow for self-consistent calculation of nonlinear turbulent dissipation of in and outgoing waves [Chandran and Hollweg, 2009, Cranmer et al., 2007, Verdini and Velli, 2007]. The Coronal Multi-channel Polarimeter ($CoMP$) has provided new observational estimates of resonant damping [Verth et al., 2010], and we will work to compare our estimates to what has been observed. The spectral evolution in the formalism of Sokolov et al. [2009] will allow us to study the conversion of surface Alfvén waves to other wave modes as well. Future missions such as Solar Probe will provide even stronger constraints by sampling the lower corona environment directly (near 10 $R_{\odot}$).

In the next chapter, we present the first simulation of the interaction of a CME with a solar wind model which includes SAW damping.

Chapter 5: Evolution of a Coronal Mass Ejection in an Alfvén Wave-Driven Wind

5.1 Introduction

In all previous global simulations of CMEs in the lower corona, the solar wind heating was treated in an ad hoc manner. For example, one approach is the so-called polytropic model, in which the polytropic index is varied at each spatial location in order to achieve coronal temperatures. This solar wind model was used in such works as [Cohen et al., 2010, Liu et al., 2008b]. In Das et al. [2011], Evans et al. [2011a], Loesch et al. [2011] the value of the polytropic index from the steady state solar wind solution was not allowed to evolve after the flux rope was inserted. As the flux rope expanded, its density decreased (lower than the density in the steady state solar wind). Since the heating term was fixed, the thermal energy of the ejecta increased with time, and dominated the kinetic and magnetic energies. Therefore, in order to model CMEs in the lower corona, a physics-based solar wind model is required.

Including Alfvén waves as a driver and source of heat in solar wind models was motivated by observations of Alfvénic fluctuations [1] in the solar wind [Belcher and Davis, 1971], and in the lower layers of the solar atmosphere [De Pontieu et al., 2007, Tomczyk et al., 2007]. Additionally, Alfvénic fluctuations have been observed in prominence material [Okamoto et al., 2007], and in ICMEs at distances of 0.3-0.7 AU [Gosling et al., 2010, Yao et al., 2010]. However, Alfvén wave signatures in ICMEs are rarely seen at distances of 1 AU or larger [Liu et al., 2006a]. These observations suggest that Alfvén waves are carried into the corona by the eruption, but the waves dissipate during propagation.

[1] Alfvénic signature in observations is a correlation between perturbations in magnetic field and velocity, i. e. $\delta B \propto \delta V$

In this chapter, we present the first modeled CME in a solar wind which is driven by Alfvén waves. The waves are damped by a physically-motivated dissipation mechanism (as presented in Chapter 4). As in Chapter 2, we do not model the initiation process: the CME is modeled from the base of the corona to 8 $R_{\odot}$ as an out-of-equilibrium flux rope. We study its evolution in an ambient solar wind. Because the flux rope travels faster than the local magnetosonic speed, it acts as a piston and drives a shock wave ahead of it. We find that surface Alfvén wave damping occurs at the shock, and that the resulting temperature distribution of the CME is more realistic than from a CME modeled polytropic solar wind.

5.2 Simulation Set Up

We utilize the new solar corona component of the Space Weather Modeling Framework [Evans et al., 2011b, Toth et al., 2011, van der Holst et al., 2010] as described in Chapter 4. The wave dissipation is given by turbulence (with free parameter $L_{TUR} = 5.75 R_{\odot}$) and surface Alfvén wave damping (free parameter $C_{SW} = 18$). The parameters were chosen to fix the maximum fast solar wind speed to 800 $\frac{km}{s}$ (at 24 $R_{\odot}$), and make the relative strength of the SAW damping more than turbulence (maximum rates of 1.4 $\times 10^{-3}$ to 5.1 $\times 10^{-4}$ Hz in the steady state). We include MDI magnetogram data from CR2029 (May 2005) as a boundary condition for the coronal magnetic field. The flux rope was inserted into NOAA AR0759, the source region for the Earth-directed May 13 CME. The flux rope was oriented such that the mass of the flux rope was parallel to the neutral line of the active region, and the current direction was chosen to make the flux rope left-handed [Bisi et al., 2010b]. The free parameters of the flux rope are shown in Table 1 (see Appendix A for flux rope details).

The simulation begins by running the steady state solar wind for 12,000 iterations in local time stepping (see Chapter 2, Section 2), during which AMR increases resolution around the current sheet. The grid cell sizes range from 0.024 $R_{\odot}$ at the inner boundary, to 0.094 $R_{\odot}$ at the current sheet, to 0.75 $R_{\odot}$ at the outer boundary. Next, the simulation is

Table 5.1: Flux Rope Parameters

Parameter	Value
d	25 Mm
R	95 Mm
a	18 Mm
I	250 MA
ρ	1.8e-17 g/cm^3
Free Energy	5 $\times$ 10^{31} ergs
Footpoint Separation	11.8°

run in time accurate mode for 30 minutes to relax to a steady state solution. We then refine a rectangular box in the region $1R_\odot < X < 7.25R_\odot, -6.5R_\odot < Y < 4R_\odot, -3R_\odot < Z < 7.5R_\odot$ to cell size 0.047 $R_\odot$. The box contains the entire CME and shock structure (nose and flanks) for the first 60 minutes of evolution. We did this to study the global influence of the disturbance on the solar wind environment in the corona, and visa-vera. We are not aware of any other study which resolves the entire CME structure in this manner out to $8R_\odot$. However, the consequence is that this study is at lower resolution than our previous CME study. In Chapter 3, the highest refinement was 0.012 $R_\odot$, but we could only focus our analysis near the nose of the ejecta.

5.3 CME and Shock Dynamics

First, we present the general dynamical evolution of the CME and CME-driven shock. In Fig. 5.1, we show a global view of the simulation at t=60 minutes. At this time, the shock position is 8 $R_\odot$ at high latitudes. In panel a, the perspective is such that the CME is approaching the viewer (halo view), and in panel b, is the view is rotated to see the side of the CME. The transparent purple iso-surface is defined at a plasma temperature (10 million K) which allows us to visualize the shock location [2]. Inside the shock surface, traces of the ejecta can be seen. The sphere is the solar surface, where the color contours are the radial

[2]For all analysis, the shock position is calculated with jump conditions along lines, but for a 3D visualization, we chose temperature because it corresponds approximately to the location of jump conditions.

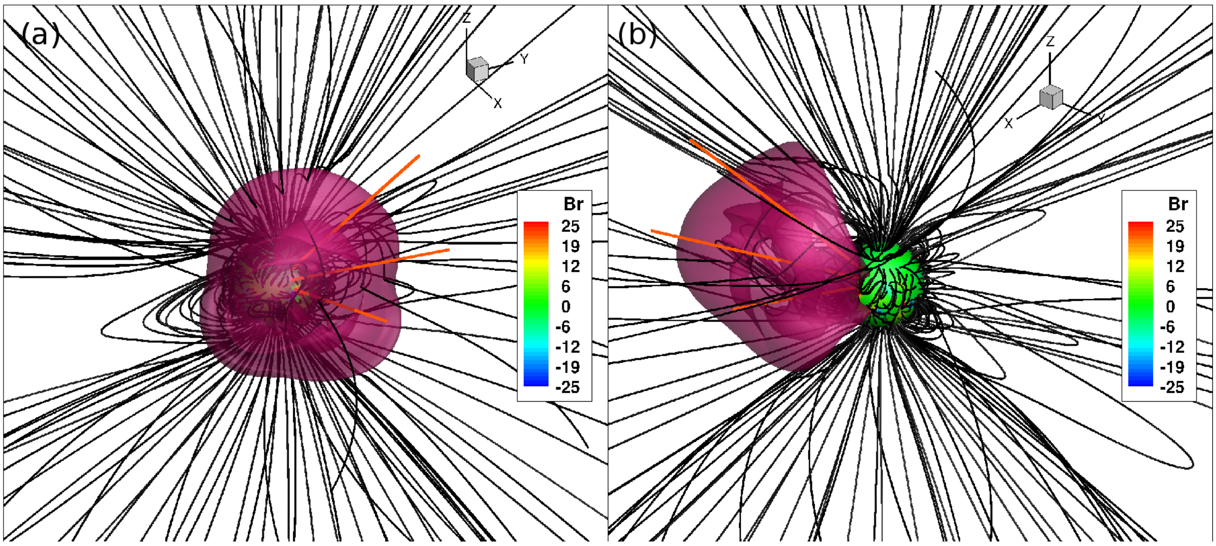

Figure 5.1: Here we show a global view of the simulation at 60 minutes after the flux rope was inserted. At this time, the shock position is 8 $R_{\odot}$ at high latitudes. In panel a, the perspective is such that the CME is approaching the viewer (halo view), and in panel b, is the view is rotated to see the side of the CME. The transparent purple iso-surface is defined at a plasma temperature (10 million K). Inside the shock surface, traces of the ejecta can be seen. The sphere is the solar surface, where the color contours are the radial component of the magnetic field. The black lines show magnetic field lines, including open polar field lines, closed streamers, streamers opened by the CME, and the twisted field lines of the ejecta [Evans et al., 2011c].

component of the magnetic field. The black lines show magnetic field lines, including open polar field lines, closed streamers, streamers opened by the CME, and the twisted field lines of the ejecta.

Because we have a large box of uniform refinement, we are able to study the behavior of the CME as a function of latitude. The three orange lines in Fig. 5.1 show locations along which we sample data presented in later figures. The lowest latitude line, Line 1, is at latitude 17 degrees, and passes through the center of the coronal streamer. The middle line, Line 2, is at latitude 31 degrees, and traces the approximate direction of the nose of the CME. The final line, Line 3, is at latitude 46 degrees, and passes through the edge/flank of the CME. Each line is drawn from the point (0,0,0), and therefore only Line 1 intersects the CME initiation site.

For our analysis, we need to define the structures in the simulation: the shock, sheath, CME-pause and ejecta. As discussed in detail in Chapter 3 Section 3, we utilized the angle [Burlaga, 1988]

$$\theta_B = sin^{-1}\frac{B_N}{B} \tag{5.1}$$

where B_N is the normal component of the magnetic field in the Radial-Tangential-Normal (R-T-N) coordinate system (a Cartesian system defined at the location of the spacecraft; R is the direction from the center of the Sun to the spacecraft location, T is in the direction R $\times$ Z, and N completes a right-handed system). A strong change in this angle indicates the boundary between regions of different magnetic fields, as can been seen in Figure 5.2 (t=40 minutes, 4.5 $R_\odot$). The white lines are projections of the magnetic field on the plane, and the gray lines correspond to the orange lines in Figure 5.1. It can be seen that there is a sharp jump in the angle at the shock and at the CME-pause, and so we use this criterion to define the shock and CME-pause positions. As a result of numerical diffusion, the shock is not a sharp discontinuity, but instead has a finite thickness. Therefore, defining the upstream and downstream positions of the shock is not a trivial matter. Here, we utilize the jump in θ_B to define the upstream shock position (other options include plasma density and velocity gradients, for example). The downstream is identified with a gradient in solar wind speed (as in Loesch et al. [2011]). The shock position is then assigned to be the midpoint of the upstream and downstream locations.

In Figures 5.3 and 5.4, we show the bulk fluid speed (U, blue line) and the magnetosonic speed ($V_m s$; green line) as a function of distance for Lines 1 and 3, respectively, at several selected times. The y-axis scale on all panels is from 0-2000 km/s. In Figure 5.3b, the single vertical line marks the front of the disturbance (before a shock has formed). In Figure 5.3c-f and Figure 5.4b-c, the two lines mark the shock location and the back of the sheath (front of the flux rope). At t=0, the profiles of V_{ms} have different shapes, as discussed in Chapter 2. Line 1 (Figure 5.3a), which was extracted radially from the active region, monotonically decreases with height from a large initial value. Line 3 (Figure 5.4a) shows a maximum

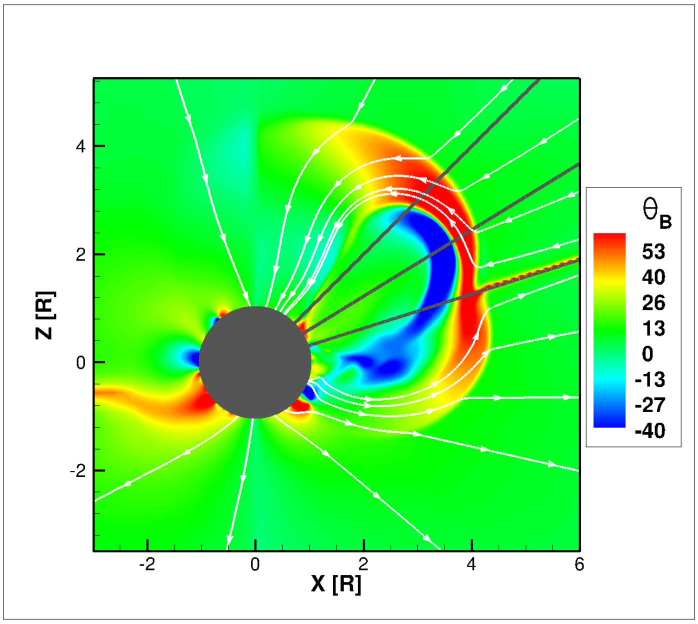

Figure 5.2: The angle θ_B is show in a meridional slice after 40 minutes of CME evolution. This angle traces out the structures of the CME, like the shock, sheath, CME-pause and ejecta.Slice showing CME structures after 40 minutes of evolution. The three gray lines are (in order of increasing latitude) Line 1, Line 2 and Line 3 [Evans et al., 2011c]. See text for details.

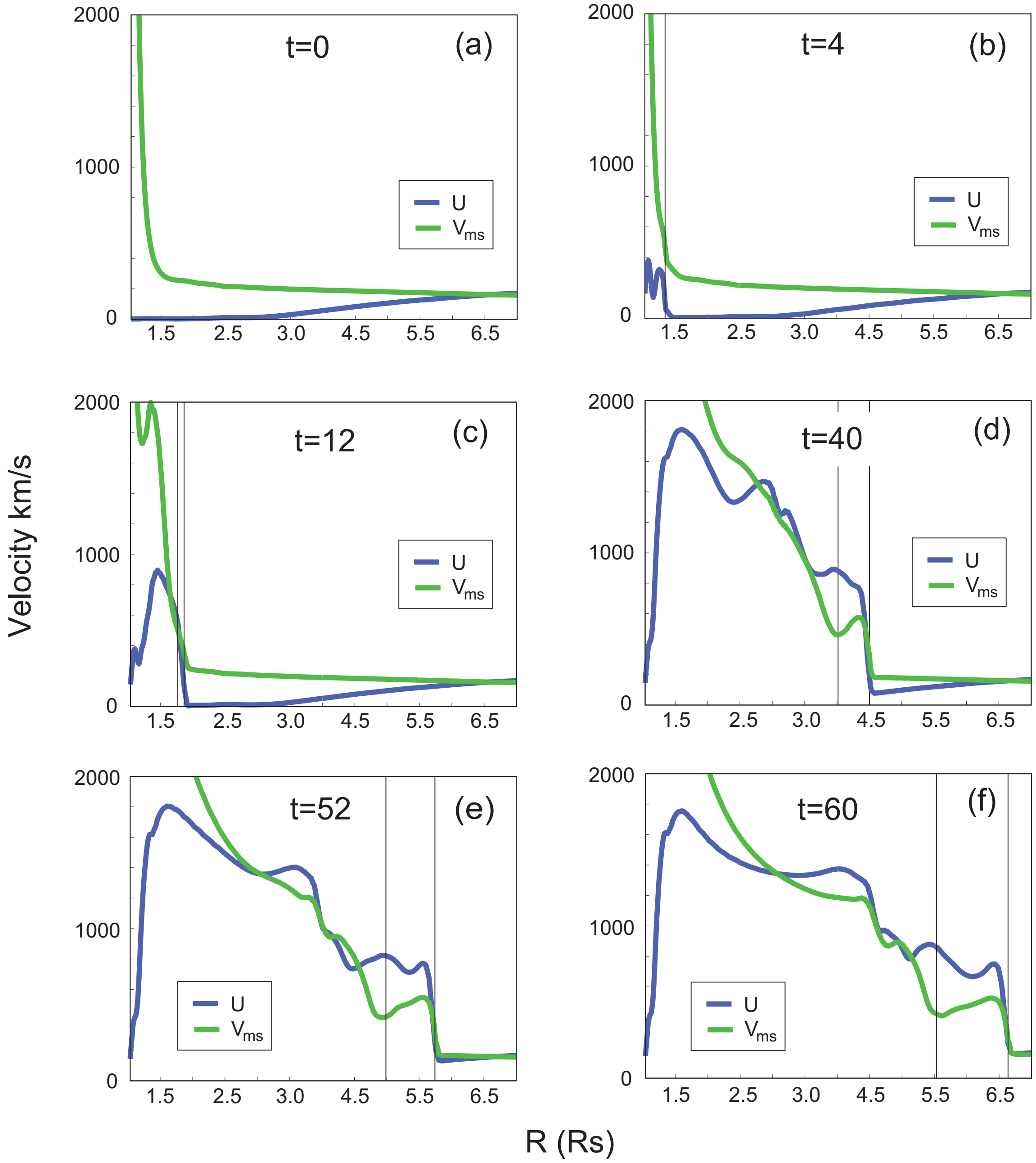

Figure 5.3: The bulk fluid speed (U, blue line) and the magnetosonic speed (V_ms; green line) as a function of distance for Line 1 at 0, 4, 12, 40, 52 and 60 minutes after the flux rope was inserted. The y-axis scale on all panels is from 0-2000 km/s. The vertical lines mark the shock location and the back of the sheath (front of the flux rope) [Evans et al., 2011c].

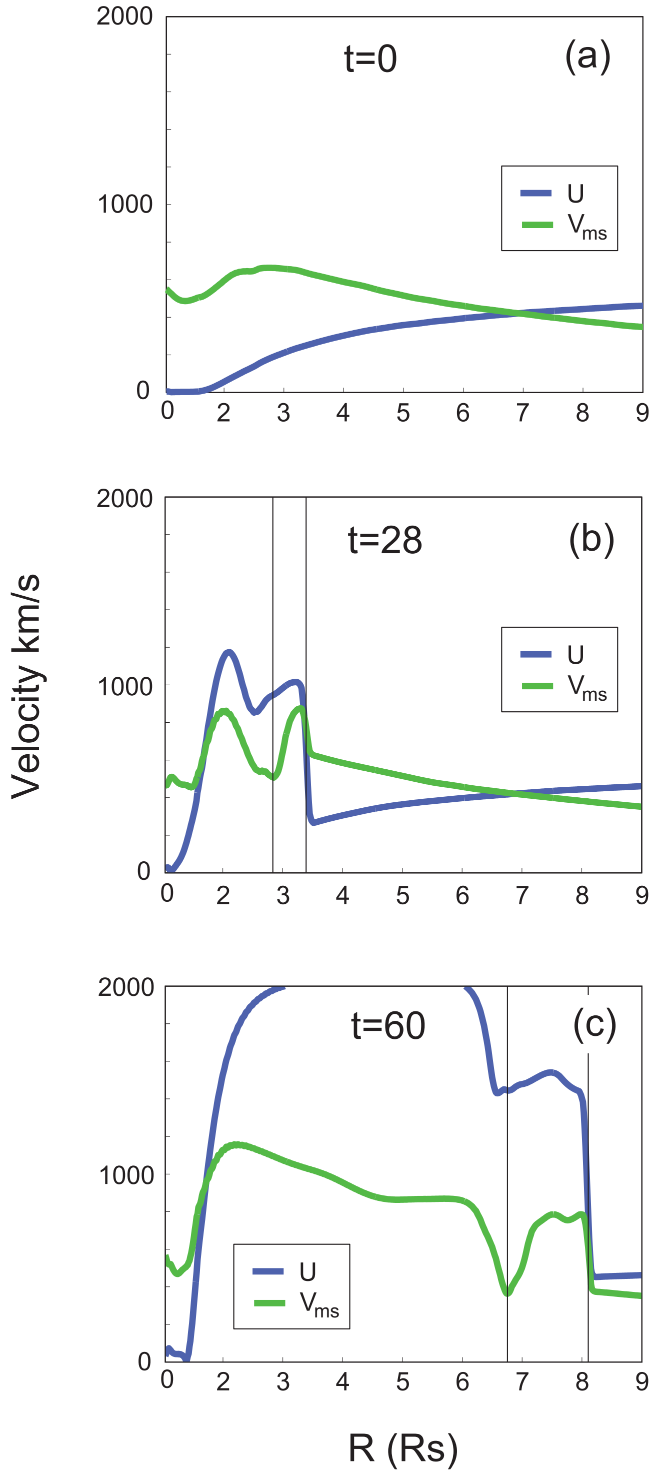

Figure 5.4: The bulk fluid speed (U, blue line) and the magnetosonic speed (V_ms; green line) as a function of distance for Line 3 at 0, 28 and 60 minutes after the flux rope was inserted. The y-axis scale on all panels is from 0-2000 km/s. The vertical lines mark the shock location and the back of the sheath (front of the flux rope) [Evans et al., 2011c].

(hump) in the profile at 2.8 $R_\odot$, expected behavior for a region nearby to active regions or quiet Sun. Although shock waves have been observed at heights less than 1.2 $R_\odot$ Kozarev et al. [2011], this modeled flux rope has an initial radial velocity which is much smaller than the local magnetosonic speed (Figure 5.3b), and therefore the disturbance does not steepen into a shock along Line 1 until t=12 minutes (2 $R_\odot$; Figure 5.3c). More than thirty degrees higher in latitude, along Line 3, the shock steepening can be seen in Figure 5.4c ($3R_\odot$; t=26 minutes).

In Figures. 5.3c-f and 5.4c, it can be seen that the disturbance alters the profile of $V_m s$. This effect was not discussed in Chapter 2, where we considered only the Alfven speed profile in the pre-event solar wind. Here we see how the characteristic speed changes by the presence of the disturbance, and we see that the profile is increased, which inhibits the formation of a reverse shock behind the CME-driven shock.

In Fig 5.5, we show the shock height as a function of time (panel a) and shock velocity as a function of shock height (panel b) for Lines 1, 2, and 3 (thin solid line, dashed line, and thick solid line, respectively). The shock velocity is calculated according to the Rankine-Hugonoit condition for conservation of momentum across the shock [Liu et al., 2008b, Lugaz et al., 2007],

$$V_S = \frac{\rho_u \left(\mathbf{U_u} \cdot \mathbf{n}\right) - \rho_d \left(\mathbf{U_d} \cdot \mathbf{n}\right)}{\rho_u - \rho_d} \tag{5.2}$$

where the shock normal $\mathbf{n}$ is calculated as in [Loesch et al., 2011],

$$\mathbf{n} = \frac{\mathbf{U_u} - \mathbf{U_d}}{||\mathbf{U_u} - \mathbf{U_d}||}. \tag{5.3}$$

It can be seen that the shock velocity increases with latitude, ranging from 1,000 to 1,500 km/s at Line 3. This latitudinal dependence is due to the motion of the CME having two contributions: the radial, propagation motion plus the expansion (lateral) motion. In order to track the lateral motion of the CME, we generated synthetic Thompson-scattered

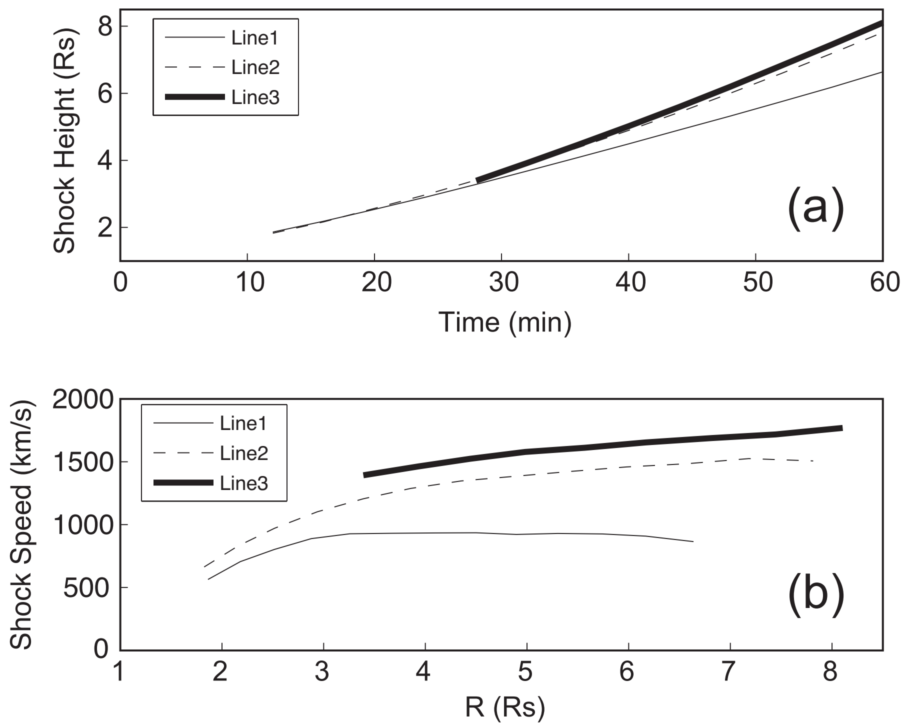

Figure 5.5: The shock height as a function of time (panel a) and shock velocity as a function of shock height (panel b) for Lines 1, 2, and 3 (thin solid line, dashed line, and thick solid line, respectively) [Evans et al., 2011c].

white light coronagraph images with the SWMF. The image is generated by specifying an observer location, aperture size and a limb darkening parameter (set to 0.5). The simulation then integrates the plasma density along lines of sight, and generates an image which can be compared to coronagraph images from LASCO and STEREO. Figure 5.6 shows the resulting images for times a) 16, b) 30, and c) 60 minutes, for an observer in a vantage point such that the CME is propagating towards the spacecraft (halo view). In panel d, we show the eruption at t=60 minutes, as seen from the perspective of a limb event (90 degrees from the halo vantage point). At early times, the shock cannot be distinguished from the flux rope, but at t=60 minutes, the faint front of the shock is seen to be separated from the ejecta material from both vantage points, as seen in observations [Ontiveros and Vourlidas, 2009].

We calculate the expansion velocity according to the cone model, in which it is defined as the rate at which the widest lateral dimension increases with time [Dal Lago et al., 2003]. The dashed line circles in Figure 5.6 show how we calculated the lateral dimension. During the timeframe in which the structure is visible as a halo event (16-60 minutes), the expansion speed exceeds 1,000 km/s, and exceeds the radial velocity of the disturbance in the very low corona. The strong lateral expansion not only drives a fast shock at the flank of the CME, but it also causes solar wind material to accumulate in front of the flux rope. This structure was defined to be a piled-up compression region (PUC; Das et al. [2011]). In Figure 5.7, we show both the shock compression ratio (ratio of downstream to upstream density), and post shock compression ratio (PSCR; ratio of PUC to downstream density) for Lines 1, 2, and 3 as a function of shock height. Along Line 1, the SCR is 4 below 2.5 $R_\odot$, but decreases to 3 until 7 $R_\odot$. At all heights, the PSCR (here due to streamer interaction, Manchester et al. 2005) has a weak value of 2. Along Line 2, the SCR is also 4 below 3 $R_\odot$, at which point it decreases with height. However, the PSCR is much stronger than at the streamer core, and becomes larger than the SCR at 4.5 $R_\odot$. This compression is a PUC due to the lateral expansion. The PUC is even stronger along Line 3, dominating the SCR at all heights. The strong PUC found in the simulation should be observable in CME events detected in coronagraph images [Ontiveros and Vourlidas, 2009].

There is a question of whether the PUC is a compression region or a reverse shock [Das et al., 2011, Liu et al., 2008b]. In Figure 5.3 c-d and 5.4c, it can be seen that there are instances when the flux rope moves faster than $V_m s$, so PUC could be a shock. At other times (Figure 5.3 e-f), its speed is below the magnetosonic speed, so the structure is a compression region. Any further investigation of this point is left to future work, as the resolution in this simulation was not high enough to study this point in detail.

Lastly, in Fig. 5.8, we show the standoff distance (the separation between the ejecta/driver and the disturbance front/shock) along Lines 1, 2, and 3 as a function of height. The standoff distance grows slowly at first, because the expansion speed is large, and the ejecta can keep up with the shock, as discussed in Gopalswamy and Yashiro [2011]. However, at later

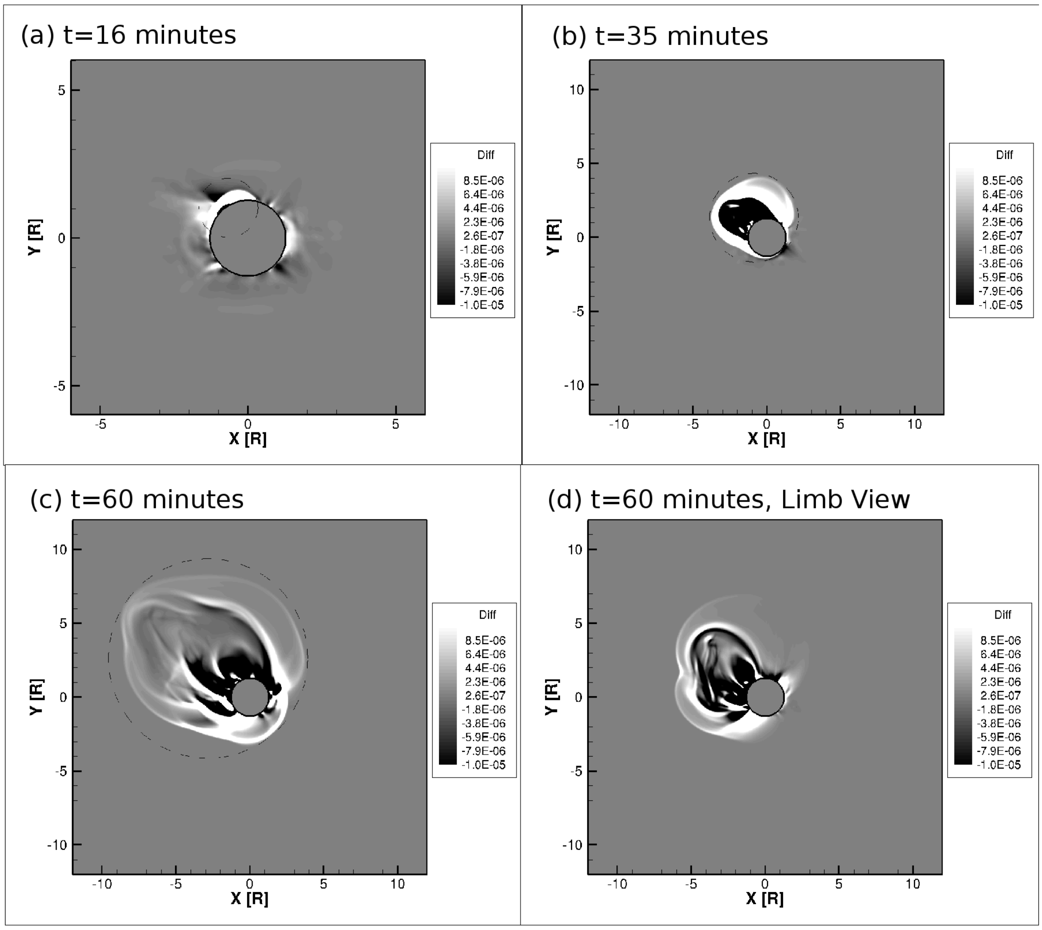

Figure 5.6: Synthetic white light images from the simulation for times a) 16, b) 30, and c) 60 minutes, for an observer in a vantage point such that the CME is propagating towards the spacecraft (halo view). In panel d, we show the eruption at t=60 minutes, as seen from the perspective of a limb event (90 degrees from the halo vantage point) The dashed line circles show fits of the lateral expansion, used to calculate the expansion velocity [Evans et al., 2011c].

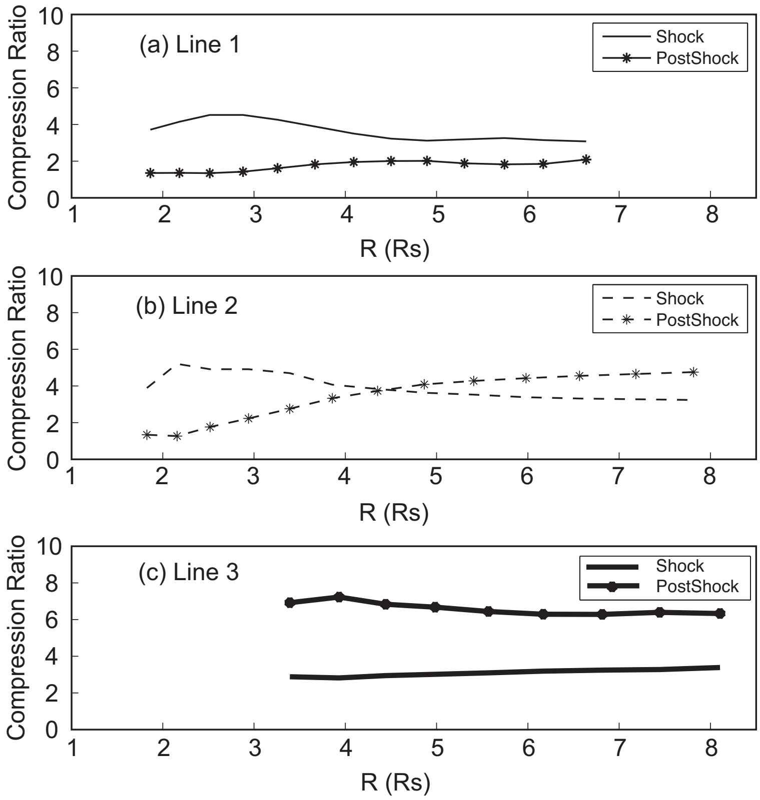

Figure 5.7: Shock and postshock compression ratios for Lines 1, 2 and 3 [Evans et al., 2011c]. See text for details.

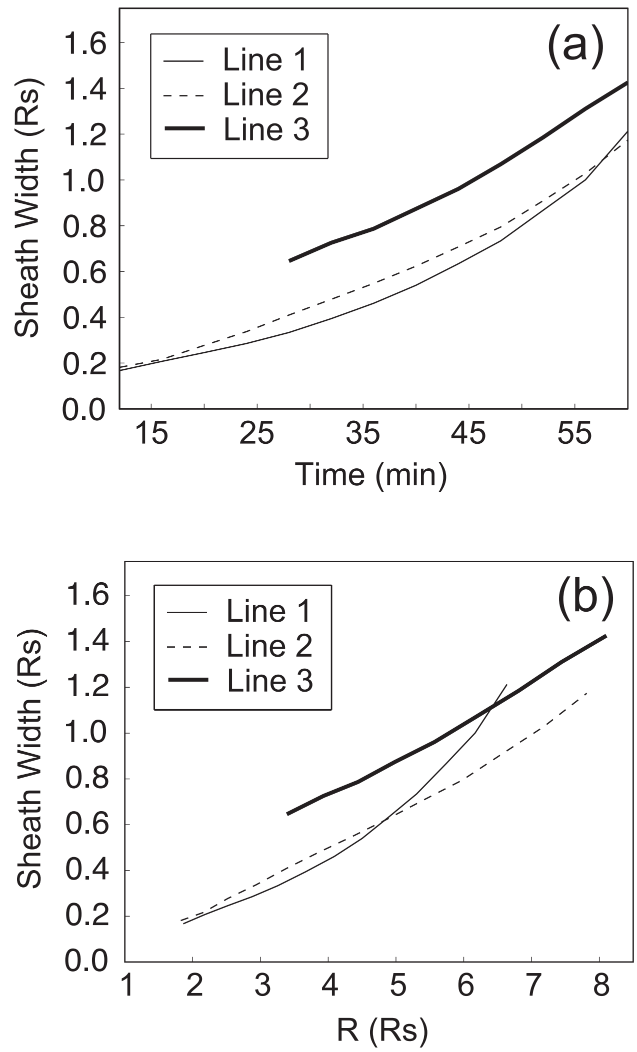

Figure 5.8: Sheath width as a function of a) simulation time, and b) shock height along radial lines at different latitudes [Evans et al., 2011c].

times, the shock speed increases. If the driver does not accelerate, then the shock can separate from the driver (meaning the standoff distance increases more rapidly). If the expansion of the modeled CME is realistic (and not a consequence of the flux rope model) then the evolution of the sheath for a fast CME (with speeds over 1,000 km/s) should follow a similar pattern.

5.4 Wave Energy Evolution and Shock Heating

Before we describe the evolution of Alfvén waves due to the presence of the CME, we will review the distribution of wave energy in the steady state solar wind. Initially, the wave energy is specified on the inner boundary based on the magnetic field geometry: at the footpoints of closed fields lines, the wave energy is set to zero; and at the footpoint of open field lines, the wave energy is specified by applying conservation of energy along the field line (see Chapter 4).The wave energy evolves according to

$$\frac{dE_W}{dt} = -\nabla \cdot (E_W \mathbf{V_g} + \mathbf{u} \cdot \mathbf{P_W}) + \mathbf{u} \cdot (\nabla \cdot \mathbf{P_W}) - \Gamma E_W \tag{5.4}$$

The first term on the right hand side of the equation represents advection of the wave energy by the solar wind. The second term is the wave stress, which represents an exchange of momentum between the waves and the solar wind. The final term is the wave dissipation, which is wave energy passed to the solar wind as heat.

As the flux rope is inserted out of equilibrium, it immediately begins to rise and expand. In Figure 5.9a-c, we show the wave energy density and plasma density along Line 1 at several times. The black vertical line marks the leading edge of the disturbance. In panel a (t=4 min) the disturbance is propagating in a region where the wave energy is essentially zero (the closed loop streamer region). At t=16 minutes (panel b), the disturbance enters a region where the wave energy is non-zero, and it appears as if the disturbance pushes the wave energy forward. In panel c (t=20 minutes; R=2.5 $R_\odot$), the wave energy continues to

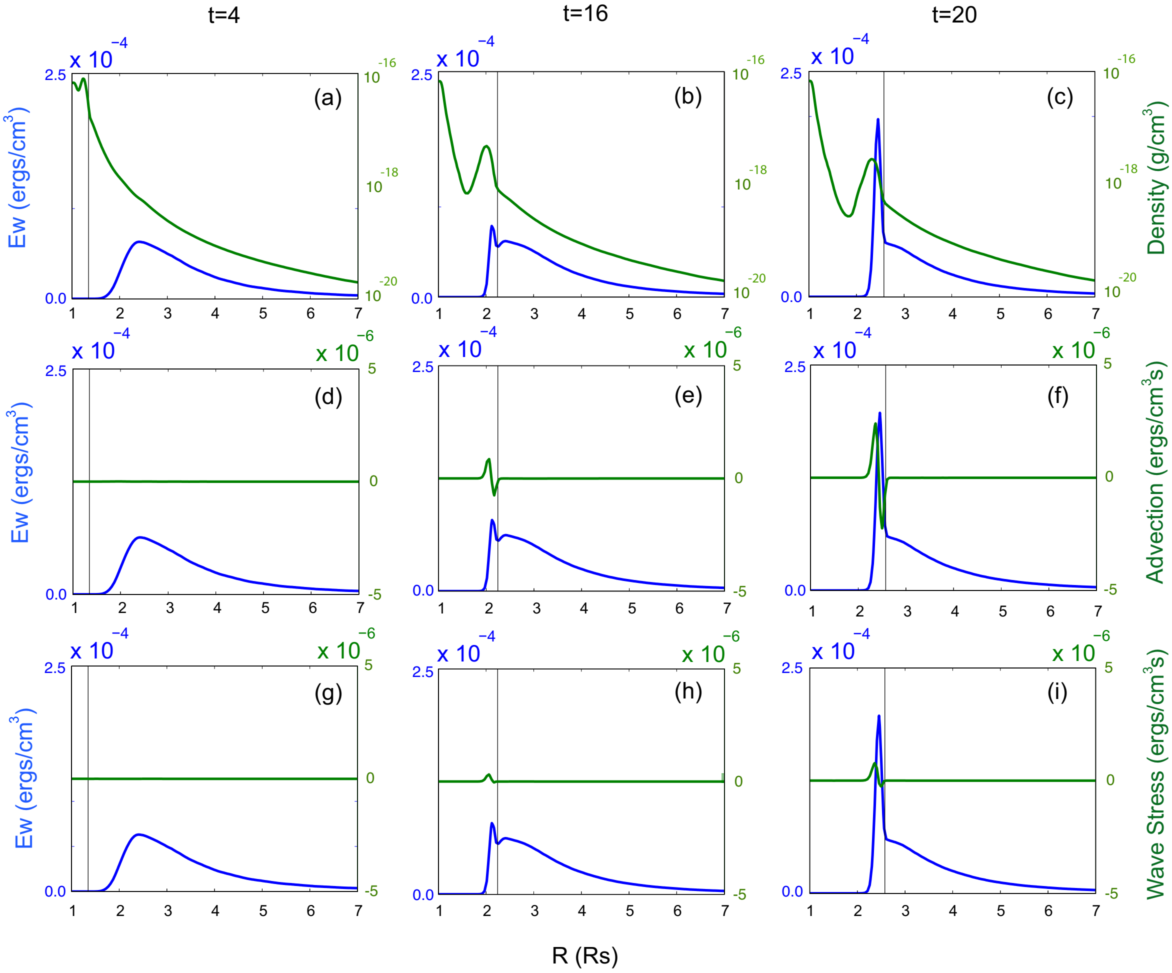

Figure 5.9: Evolution of the wave energy (blue lines) at 4 minutes (first column), 16 minutes (second column) and 20 minutes (third column) after the flux rope was inserted (sampled along Line 1). In the top row, the plasma density is shown as the green line. In the second row, the advection term in the wave transport equation is shown as the green line. In the third row, the wave stress (or work done on or by waves) term is shown as the green line. The black vertical line marks the leading edge of the CME [Evans et al., 2011c]

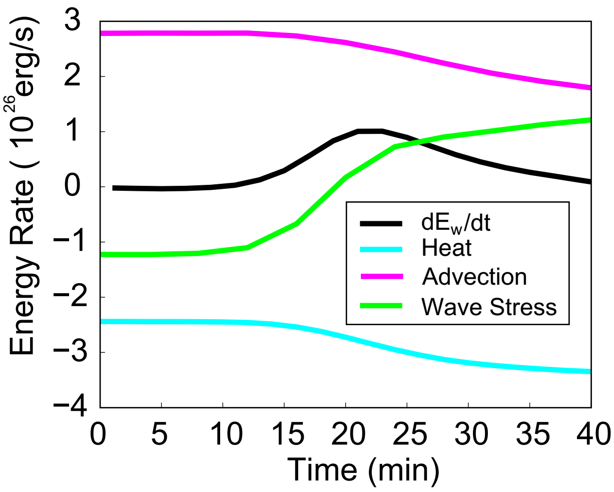

Figure 5.10: Terms of wave transport equation (Eq. 5.4) integrated in the volume surrounding the CME as a function of time [Evans et al., 2011c].

move out into the corona with the shock.

In Fig. 5.9, we show the advection (panels d-f) and wave stress terms (panels g-i) of the wave transport equation. The physical explanation of the transport of the wave energy with the flux rope is that the disturbance sets up a gradient in velocity, which drives advection of the wave energy with the disturbance. The gradient in velocity is strongest at the shock, and since the wave energy cannot travel ahead of the shock (the group velocity is less than the shock speed), the wave energy is focused to the downstream shock location. Therefore, the role of the advection term is to transport the energy spatially according to the motion of the CME (or shock). The wave stress term also plays a role in the evolution of the wave energy in the sheath. In Chapter 4, we discussed the role of the wave stress term in the solar wind it transfers momentum to the wind to accelerate it, which occurs because the gradient of the wave pressure is a negative quantity everywhere. However, the advection of wave energy into the sheath creates a gradient which is positive. This leads to a transfer of energy from the sheath plasma to the waves, which locally enhances the wave energy. The peak of the wave energy density decreases with time due to wave dissipation (discussed in detail below).

To understand what is happening on large-scales, we integrate each term of the wave transport equation in a volume of uniform grid refinement which contained the entire CME structure through one hour of propagation. The result is shown in Fig 5.10: change in energy, black; advection, magenta; wave stress, green; and wave dissipation, blue. In the steady state solar wind solution, the wave stress in the volume was $-1\times10^{26} erg/s$. Around 14 minutes, the total wave stress in the volume becomes more positive, and at 20 minutes, the term integrated in the volume is positive. This process increases total amount of wave energy in the volume from $2.03\times10^{30} ergs$ to $2.12\times10^{30} ergs$ (from t=0 to t=40 minutes; R=$4.5R_{\odot}$). At t=25 minutes, the kinetic energy of the CME is $2\times10^{31} ergs$. Therefore, the transfer of energy from the CME to the waves has a negligible effect on the motion of the CME and the shock (meaning, there is no signature in the kinetic energy evolution). This wave stress term drives changes in dE/dt from 14-24 minutes, until the wave dissipation becomes important.

The wave dissipation in the simulation is a combination of two mechanisms: turbulence and surface Alfvén wave dissipation. Both dissipation mechanisms occur at the shock (for SAW due to the gradient in density, and for turbulence because the wave energy and magnetic field are enhanced), but the rate of dissipation for surface Alfvén wave damping is a factor of 5 (or larger) than turbulence at the shock. In the volume surrounding the CME, the wave heating rate remains at the steady state solar wind value until around 10-12 minutes (Fig. 5.10; the shock has not formed at this time). There are two reasons that the heating begins to increase at this time: a) the amount of wave energy available to be damped is increased due to advection and energy transfer from the plasma, and b) the shock forms, which creates a strong gradient in density. Around t=45 minutes (5 $R_{\odot}$), the heating term becomes larger than the advection and wave stress terms. At this point, the amount of available wave energy decreases, which causes the heating rate to decrease as well.

During the time from 25-40 minutes, the heating rate due to surface Alfvén wave dissipation is $10^{26} ergs/s$. During the same time frame, the thermal energy of the entire

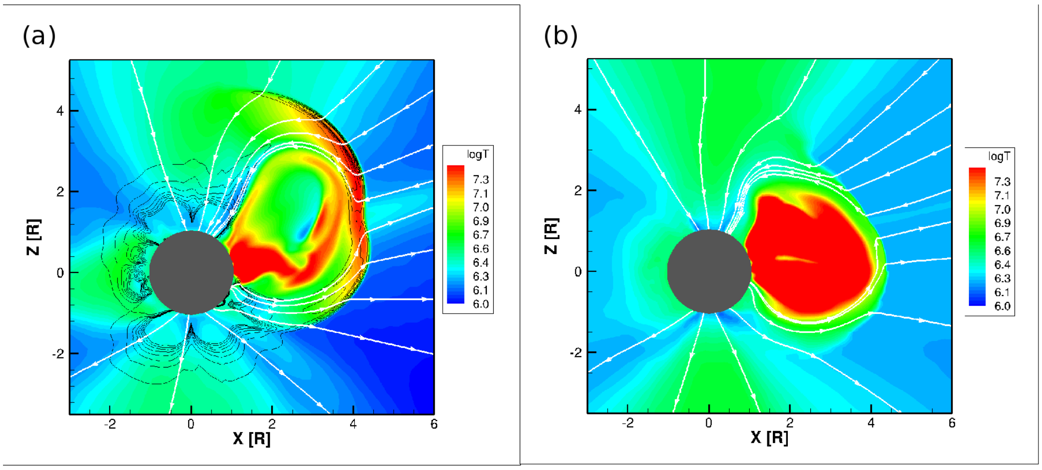

Figure 5.11: Wave-driven (left) and polytropic (right) solar wind backgrounds. Here we show the CME temperature after 40 minutes of evolution. The white lines are the projection of the magnetic field, and the black lines in panel (a) are contours of the SAW damping rate [Evans et al., 2011c].

CME structure (ejecta, sheath and shock) increases at a rate of $10^{27} ergs/s$. SAW heating therefore contributes 10% of the total heating during this time. In Fig. 5.11a, we show a meridional slice at time t=40 minutes. The color contour is log(T), where T is the plasma temperature in K. The contour lines show the heating rate due to surface Alfvén wave dissipation, and it can be seen that the heating at the shock is comparable to the heating in the fast solar wind. In Fig. 5.11b, we show the same flux rope in a solar wind with the same boundary conditions, except coronal heating is achieved by reducing the polytropic index to a value less than 5/3 near the Sun. The two temperature profiles are dramatically different: the ad hoc coronal heating resulted in overheating of the flux rope being the hottest part of the CME. However, the physically motivated heating by surface Alfvén wave dissipation causes the temperature in the sheath to be comparable (or in some places exceeding) the temperature at the edges of the ejecta. The core of the ejecta is cooler (1 million K) than the sheath (10 million K). This result is in agreement with in situ data of interplanetary CMEs in the heliosphere, the temperature in the sheath is observed to be above the temperature of the solar wind [Zhang et al., 2007], and the flux rope temperature is lower than the solar wind. It is also in agreement with the UVCS results, which found that thermal energy in the lower corona is on the order of the kinetic energy [Lee et al., 2009].

5.5 Discussion

In this chapter, we presented the first global simulation of a coronal mass ejection which propagates in a solar wind which includes physically motivated wave dissipation as a heating mechanism. We find that the coronal mass ejection and the associated shock have a strong impact on the solar wind. The CME alters the wave energy by concentrating it in the sheath through advection, and also increasing its value through momentum transfer. Even with our simple treatment of wave energy evolution (see Chapter 4), we are able to show how Alfvén waves are focused into the sheaths of ICMEs. The wave energy is then dissipated at the shock due to surface Alfvén wave damping. These results explain why Alfvénic signatures have been seen in prominence material, but are often not present in ICMEs at 1 AU [Liu et al., 2006a, Okamoto et al., 2007]. We find that even though this heating is concentrated to a small volume of the total CME structure, it accounts for 10% of the total increase in thermal energy of the CME, and therefore is an important heating mechanism in the corona (2-10 $R_\odot$).

We also studied the CME dynamics. We analyzed the lateral motion of the ejecta. Using synthetic white light images, we calculated the expansion velocity and found it to be large (1,000 km/s). This expansion resulted in a faster shock at the flanks, with a large piled-up compression region. As the PUC ratio was 8 in the middle corona, we estimate that this behavior should be present in events which have been observed with the STEREO coronagraph imagers.

Chapter 6: Future Work

The work presented in thesis will be used in two future projects with a common theme; namely the connection between large and small scales - between kinetic and fluid approaches in space physics. The first project will use the CME simulation results from Chapter 5 to study particle acceleration and transport in the lower corona by coupling the MHD results to a kinetic particle acceleration simulation. In Chapter 2, we saw how reconnection in the simulation (although purely numerical) affected the CME's evolution. The second project will incorporate the effect of small-scale reconnection physics in a global MHD simulation of a CME to improve our understanding of the role of this process in CME evolution.

6.1 Coupling a CME simulation to a Particle Transport Model

In this work, we want to understand the acceleration and transport of energetic protons in the lower corona due to an interaction with a CME-driven shock and sheath. The ingredients in this recipe include a spectrum of seed particles, a kinetic model of particle transport, and a global MHD simulation of CME evolution in the lower corona. In the past, all of these components were used independently to study the problem of shock acceleration [Dayeh et al., 2009, Desai et al., 2003, Giacalone, 2005, Manchester et al., 2005, Roussev et al., 2004]. Only one effort has been made to combine an MHD simulation of a CME with a particle transport model [Kóta et al., 2005]. In this work, the MHD variables were extracted along magnetic field lines, and coupled to a particle transport model. Although this work demonstrated that structures in a CME sheath can accelerate particles, it was not an in-depth study.

An opportunity exists to go beyond Kóta et al. [2005] and couple the MHD solution to an entire kinetic simulation grid. The kinetic model is the Energetic Particles Radiation

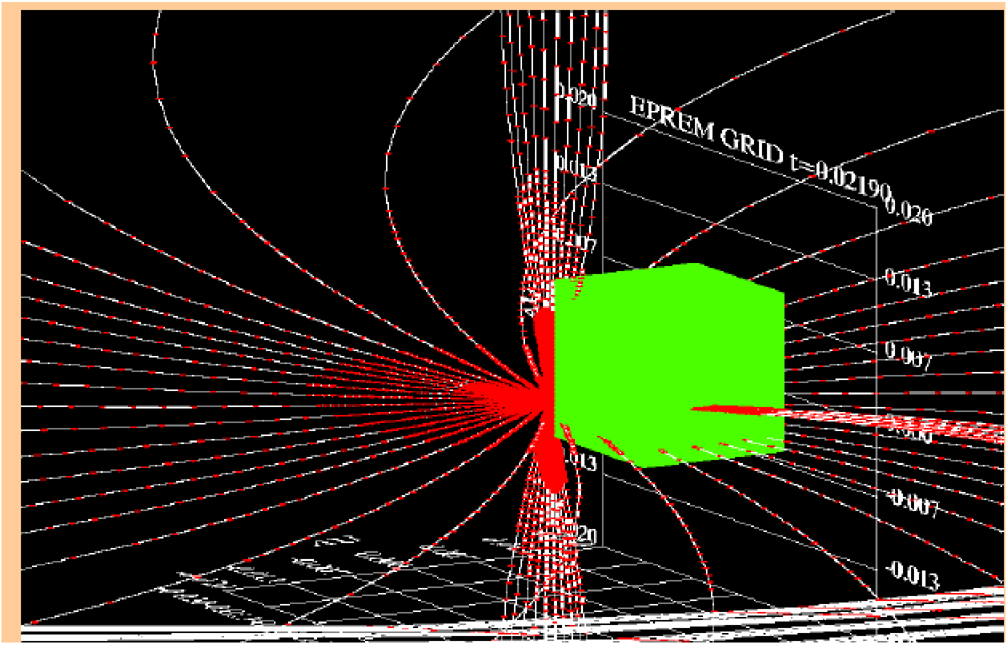

Figure 6.1: The dynamic grid of EPREM is shown. The nodes (red dots) move out along streamlines (white lines). The scale is in AU. The green box shows where the MHD parameters were interpolated onto the EPREM grid, containing the CME (Source: K. Kozarev).

Environment Model (EPREM; [Schwadron et al., 2010]. The model solves for particle transport in a dynamical grid, in which nodes move away from the Sun along streamlines, as shown in Figure 6.1 (the nodes are red dots along the white streamlines). EPREM has a Parker solar wind model incorporated, but for our work the solar wind parameters are output from the MHD solution. The full MHD grid is used for the first step, and then only the region which contains the CME is updated every two minutes.[1] See Figure 6.1 for the EPREM grid and the box of MHD data (green box) updated at 40 minutes.

For seed particles, we will use spectra of quiet time suprathermal particles derived from in situ observations (M. Al-Dayer, private communication), for the timeframe which matches the CME event we simulate in the MHD model (13 May 2005 eruption, as studied in Chapter 5). The particle fluxes are scaled to lower corona heights, and used as input in the kinetic model. Any changes to the fluxes will be due to an interaction with the CME structures.

This work will allow us to understand how the structures of a CME sheath, such as the piled-up compression in front of the ejecta, will affect particle acceleration in the lower corona. The results can be propagated to Earth to compare with in situ data for this event. Additionally, many tests of the sensitivity of the acceleration on the free parameters of particle transport (contained in the calculation of mean free paths and the diffusion coefficient) will be made by K. Kozarev.

6.2 Magnetic Reconnection: Kinetic Plasma Effects in MHD Modeling

Important physics which is critical for processes involving magnetic reconnection are missing from MHD modeling (such as Hall currents and anisotropic pressure). In order to improve the modeling, one needs to identify areas where the assumptions of MHD break down, formulate how to incorporate non-ideal effects in MHD, and quantify the interaction between

[1]The shock travels approximately 0.2 $R_\odot$ in two minutes.

global dynamics and processes on kinetic scales.

In two-dimensional (2D) theory, in which the current is taken to be along the Y-axis, the Y-component of Ohm's Law (first moment of Vlasov equation for electrons) and the momentum equation (first moment of Vlasov equation for ions) near a reconnection site (inside of the diffusion region) are:

$$E_y = -[v_i \times B]_y + \frac{1}{ne}[J \times B]_y + \frac{1}{ne}\left(\frac{\partial P_{exy}}{\partial x} + \frac{\partial P_{ezy}}{\partial z}\right) + \frac{m_e}{e}\frac{dv_{ey}}{dt} + \eta J_y \tag{6.1}$$

$$E_y = -[v_i \times B]_y + \frac{1}{ne}\left(\frac{\partial P_{ixy}}{\partial x} + \frac{\partial P_{izy}}{\partial z}\right) + \frac{m_i}{e}\frac{dv_{iy}}{dt} \tag{6.2}$$

In Eq. 6.1, the terms on the right hand side of the equation are: convection, Hall term, electron non-gyrotropic pressure, electron inertia and anomalous resistivity. In Eq. 6.2, the terms on the right hand side are convection, ion non-gyrotropic pressure and ion inertia. At the reconnection site, the Hall term is zero. In the diffusion region (see Fig. 6.2, from Kuznetsova et al. [2007]), the ion non-gyrotropic pressure term from Eq. 6.1 must match the Hall and electron non-gyrotropic pressure terms. At the outer boundary of the diffusion region, conservation of flux requires that the reconnection electric field must match the electric field directly outside the box.

Very near the reconnection site, the term dominating in Eq. 6.1 is the electron non-gyrotropic pressure, which can be approximated as

$$E_0^{ng} = \frac{1}{e}\sqrt{2m_eT_e}\frac{\partial v_{ez}}{\partial x} \tag{6.3}$$

Kinetic simulations have shown that the reconnection rate does not depend on the electron mass or temperature. This allows the above expression to be written instead in terms on the ion mass, and the bulk fluid temperature and velocity. It was found to have good agreement with kinetic simulation [Kuznetsova et al., 2000].

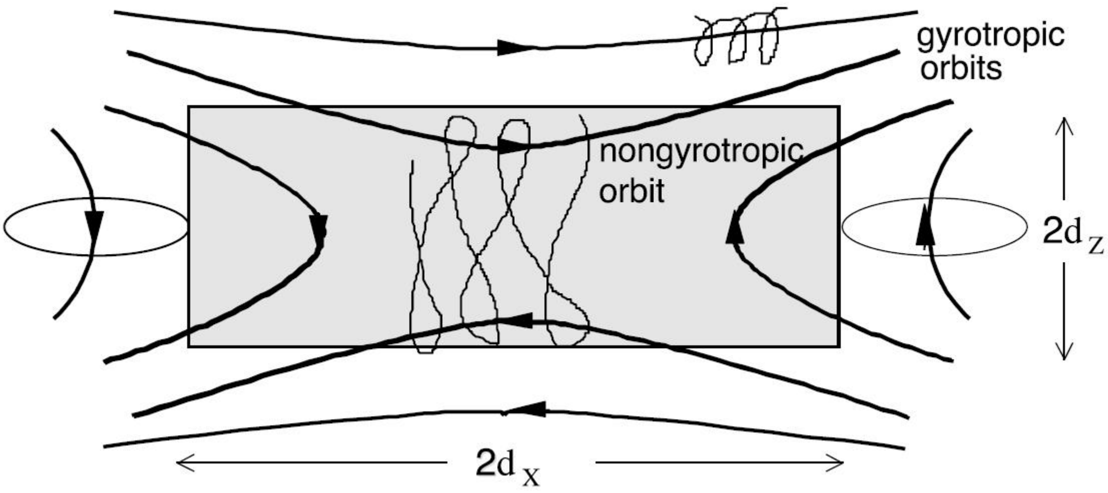

Figure 6.2: Schematic of the diffusion region surrounding a reconnection site, where MHD approach breaks down [Kuznetsova et al., 2007].

The non-gyrotropic correction to the MHD solution is obtained by calculating the non-gytropic electric field component, and adding it as a source term to the magnetic induction equation in BATS-R-US. The remaining MHD equations are unchanged. This process is described in detail in the next section.

Implementation for the Magnetosphere: Kuznetsova et al. 2007

The methods of Kuznetsova et al. [2007], which bridge the gap between small scale modeling and large-scale dynamics and were applied to the magnetosphere. The application of this approach to the solar corona will be done in future work. [Kuznetsova et al., 2007] included the effect of pressure due to non-gyrotropic motion (described in detail below) in BATS-R-US, and ran it in the Global Magnetosphere component of the SWMF. They demonstrated that non-gyrotropic correction significantly altered the magnetosphere evolution by generating periodic motion of the reconnection site down the magnetotail, which had been observed but never reproduced in an MHD simulation.

The setup for the magnetosphere uses a symmetric case, in which the equatorial plane of Earth which is the X-Y plane, and the -X axis is the direction of the tail. The main tail current direction is in the Y direction. Recreating such symmetry in a CME simulation will not be possible. This challenge will be discussed later.

The process of incorporating the non-gyrotropic correction into the MHD simulation can be broken up into three major actions:

Step 1: Reconnection Site Search

The first step is to locate a reconnection site within the simulation. The criteria imposed in the magnetosphere case was that two components to the magnetic field, B_x and B_z, reverse direction. The block-based structure and parallel nature of BATS-R-US makes such a search computationally efficient. The user specifies the number of cells per block (for example, $4 \times 4 \times 4$). We specify each cell to be a cube, each side of length Δl. The region in which the search occurs is specified by the user. In the symmetric case, the search occurs for $|Y| < Y_{max}$ and $|Z| < Z_{max}$, and $X_{min} < X < X_{max}$. Each $Y = Y(n)$ plane is searched separately, where the index n is equal to 1 for the plane $Y = Y_{min}$ and $n = \frac{2Y_{max}}{\Delta l} + 1$ for the plane $Y = Y_{max}$. Intermediate planes are named as $Y(n) = Y_{min} + \Delta l\,(n-1)$. Each block first checks whether it is inside the search region and intersects the $Y = Y(n)$ plane. Blocks that pass this test then search in arrays of $X(n)$ and $Z(n)$ for cells (i, j_n, k) in which both B_x and B_z change direction by the following criteria (for the symmetric magnetosphere: $B_z(i-1, j_n, k) < 0$, $B_z(i+1, j_n, k) > 0$, $B_x(i, j_n, k-1) < 0$, $B_x(i, j_n, k+1) > 0$.

The blocks then exchange information using MPI library calls and sort the reconnection sites by their distance to the Earth, and store the locations to arrays $X_m(n)$, $Z_m(n)$, where the index $m = 0$ for the site closest to the Earth.

Step 2: Calculate Non-gyrotrpic Correction

Once all reconnection sites have been located, the next step is to calculate the size of each diffusion region - where the ions decouple from the magnetic field and ideal MHD breaks down. The boundary of this region is estimated from the gyrotropic orbit threshold condition, where the ion gyroradius is equal to the distance to the reconnection site:

$$d_x = \left(\frac{2m_iT}{e^2\frac{dB_z}{dx}}\right)^{1/4}, \quad d_z = \left(\frac{2m_iT}{e^2\frac{dB_x}{dz}}\right)^{1/4} \tag{6.4}$$

where m_i is the ion (proton) mass, T is the temperature, and e is the electron charge. These values are taken from the MHD solution at the reconnection site.

The total non-gyrotropic electric field at each location is a sum of the electric fields due to each reconnection site, multiplied by a cut-off function:

$$E_y^{ng}(i,j,k) = \sum E_0^{ng}(m,n)\left[cosh^{-1}\left(\frac{x(i,j,k)-x_m(n)}{d_x(m,n)/2}\right)cosh^{-1}\left(\frac{z(i,j,k)-z_m(n)}{d_z(m,n)/2}\right)\right] \tag{6.5}$$

$$E^n g_0 = \frac{1}{e}\sqrt{2m_iT}\frac{\partial v_z}{\partial x} \tag{6.6}$$

The term in square brackets is a cut-off function applied to ensure that the contribution goes to zero outside of the diffusion region, chosen to match with kinetic simulations [Kuznetsova et al., 2007]. The above expressions use MHD solution at each reconnection site $X_m(n)$, $Z_m(n)$.

Step 3: Connection to MHD

The final step is to insert the reconnection electric field into Faraday's law,

$$\frac{\partial \mathbf{B}}{\partial t} = -\nabla \times (-\mathbf{v}\times\mathbf{B} + \mathbf{E^{ng}y}) \tag{6.7}$$

The curl of E^{ng} is taken analytically. Steps (1)-(3) repeat at each iteration.

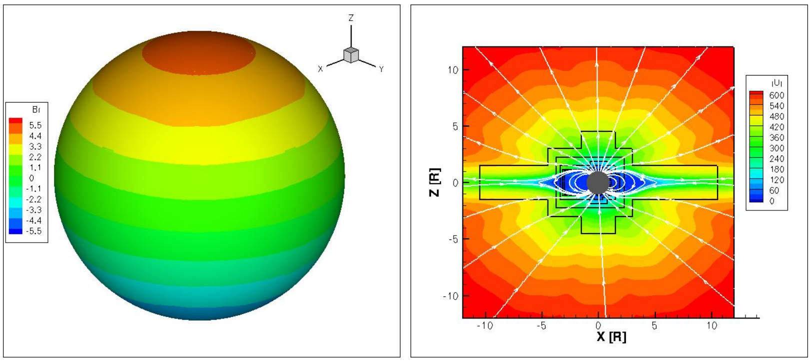

Figure 6.3: Magnetic field on the solar surface, and solar wind velocity in a meridional plane for an artificial symmetric solar wind.

Implementation in the Solar Corona

The success of the above procedure in simulations of the magnetosphere with the SWMF motivated us to apply the same method in a simulation of a CME in the lower corona. Some differences between the cases are that a CME both expands and propagates through the solar wind, whereas the magnetosphere is (essentially) a stationary obstacle for the solar wind. The Earth's orbital speed is roughly 30 km/s, which is much smaller compared to the solar wind speed at 1 AU of 400-700 km/s, whereas a CME can travel hundreds to thousands of km/s in a region where the solar wind speed is much lower. An additional complication with the CME case is the difficulty in producing a symmetric geometry (as was done in the magnetosphere). We have started tackling this daunting task by creating a simple geometry for the solar wind and the flux rope for the implementation of the nongyrotropic reconnection.

The first step was to create a simple background solar wind. The simplest configuration is a dipolar magnetic field. We achieved this by producing an artificial magnetogram file, containing the radial component of the magnetic field of a dipole ($B = B_0\sqrt{3\cos^2\theta + 1}$). A free-standing module in the SWMF will read in the radial component of the magnetic field and output coefficients to the spherical harmonics expansion used by the Potential Field Source Surface model for the initial condition of the magnetic field. The user can specify

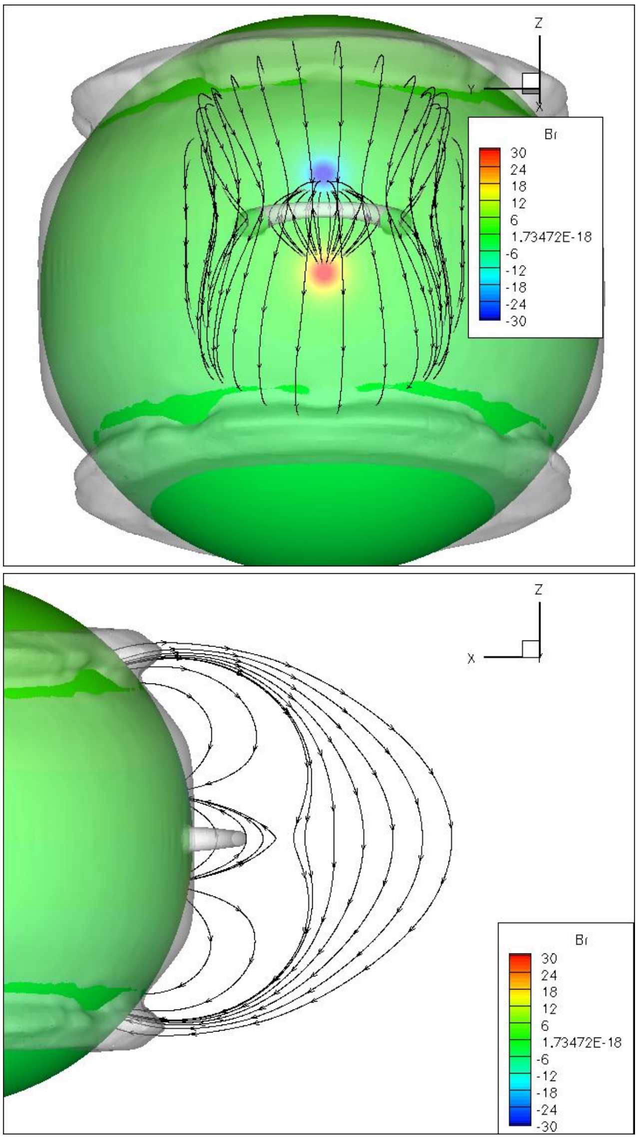

Figure 6.4: the initial geometry of the flux rope is shown. We use a modified TD flux rope, including only subphotospheric magnetic charges to generate a simple field for the eruption (see Appendix A).

the number of order of spherical harmonics. For a pure dipole, every term except the second order should be zero, and so we had the choice to create a harmonics file by hand with all terms zero except the second order (and scale the factor to get the desired magnetic field strength), or to create one using the B_r values calculated. We tried both and achieved the most symmetric solar wind with the second option. The magnetic field strength at the poles was 4.8G, and 2.4G at the equator (typical quiet Sun field values). The solar wind speed reached 300 km/s in the equator, and 600 km/s in the poles. Fig. 6.3 shows the magnetic field on the solar surface, and the resulting solar wind speed in a meridional slice.

The second step is to create the most symmetric eruption. As the global dipolar field of the Sun was from North-South, we set up an ejecta field that was dipolar but oppositely oriented, from South-North. This set up reconnection at the top initially, and reconnection at the back occurred later. The flux rope model Titov-Demoulin was used, but without the line current, and only magnetic charges below the photosphere. The CME propagates down the -X axis, and the major current is in the Y-direction (as in the magnetospheric case). The setup can be seen in Fig. 6.4.

We will now discuss the results of the simulation with numerical resistivity only. As shown in Fig. 6.5, we find that the fields are stretched, and between 32-34 minutes after flux rope insertion, the field reconnects behind the ejecta, producing a plasma blob. The blob travels outward along the post-CME current sheet at a few 100 km/s. These blobs are seen in observations and other MHD simulations.

The velocity profile of the CME, Fig. 6.6, shows that there is a later stage of acceleration after the reconnection behind the CME (after the reconnection event behind the CME).

Although we have configured the simulation as symmetrically as we could, the CME rotates as it propagates outward (as discussed in Section 4.3), and therefore the current sheet rotates out of the equatorial plane. Fig. 6.7 shows the current sheet after 40 minutes. Therefore, the implementation of the reconnection search will need to go further away from the equatorial plane than in the magnetospheric case.

We look to answer the following questions:

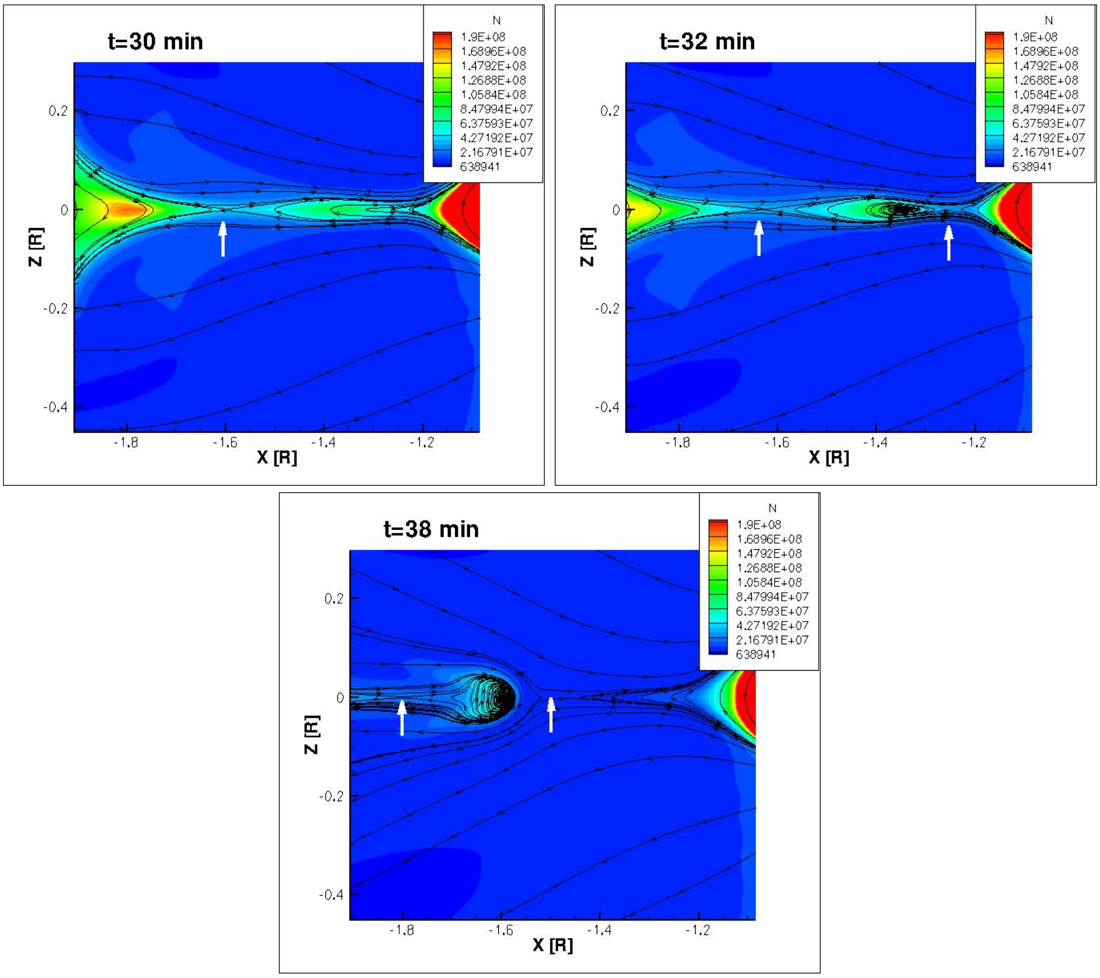

Figure 6.5: Density and magnetic field evolution in a CME simulation with numerical resistivity only. The white arrows mark reconnection sites.

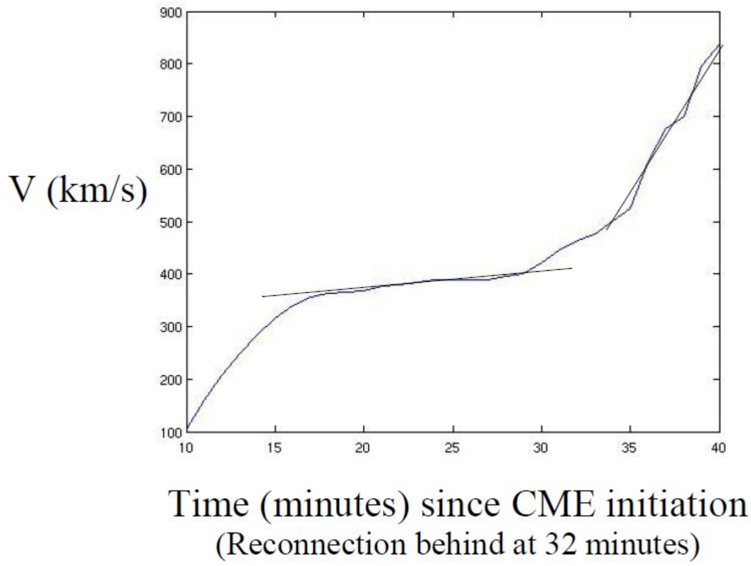

Figure 6.6: Velocity profile of the CME leading edge with time. After an initial fast rise, there is a period of almost constant velocity. After the reconnection occurs behind the CME, the CME leading edge is accelerated.

Question 1) How will the reconnection events (both in front and behind the CME) be modified?

Question 2) What will be the effect on the dynamics of the CME?

Question 3) How will the energy budget of the CME change?

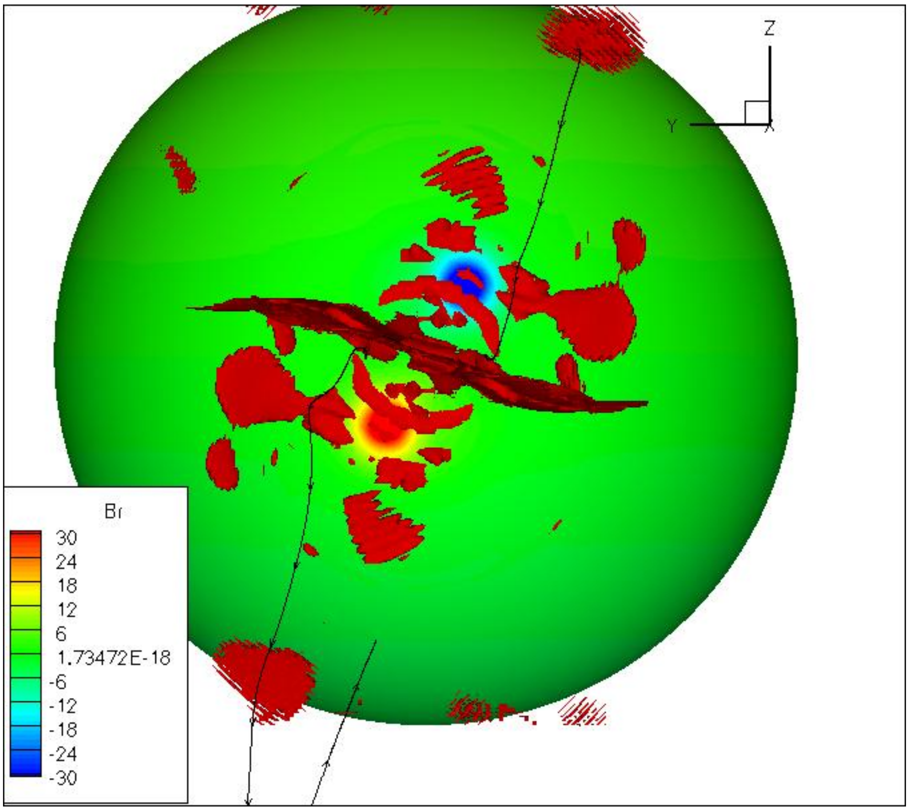

Figure 6.7: Current sheet (red isosurface) rotation out of the equatorial plane, 40 minutes after the flux rope was inserted. The blue and red dots on the solar surface are magnetic flux due to the subphotospheric charges used to generate the eruption.

Chapter 7: Summary

In this thesis, we demonstrated the importance of a realistic solar wind for properly modeling CME evolution in the lower corona (1-10 $R_\odot$). We showed that ad hoc approaches to modeling the physical processes which drive coronal heating and solar wind acceleration had repercussions for CME evolution. We do not model the initiation process, but launch out-of-equilibrium flux ropes to model a CME. First, we study CME propagation in a polytropic solar wind background, and found that the CME's thermal energy dominated in the lower corona [Loesch et al., 2011]. This result is not consistent with observations in the lower corona [Lee et al., 2009] and in situ temperature profiles in the heliosphere [Zhang et al., 2007]. Also, the shock strength (compression ratio) was larger than what is typically observed [Kozarev et al., 2011, Ontiveros and Vourlidas, 2009]. We also conducted a survey several global MHD models of the solar wind in the lower corona [Evans et al., 2008]. We found that ad hoc approaches to coronal heating resulted in low, flat Alfvén speed profiles, which would allow a slow disturbance to drive a strong shock - in contrast with statistical studies of particle acceleration in the low corona. However, local (one-dimensional) MHD models with physically motivated Alfvén wave dissipation as a source of coronal heating resulted in a steepened Alfvén speed profile, more aligned with observations.

Motivated by these results, and observations which suggest that Alfvén waves in the lower solar atmosphere may have enough energy to drive the solar wind [De Pontieu et al., 2007], we studied the process of surface Alfvén wave (SAW) dissipation in the corona. An initial estimate found that SAW damping is sufficient to heat the corona at the boundary between open and closed magnetic field lines and in the subpolar open field regions [Evans et al., 2009]. We then implemented SAW damping into a solar corona model in which Alfvén wave energy transport is self-consistently coupled to the MHD equations [van der

Holst et al., 2010]. The model included wave dissipation to mimic turbulence along open magnetic field lines. We showed that including SAW dissipation in the model improved agreement with observations of coronal temperature both near the Sun and in the inner heliosphere by comparing with STEREO and Ulysses data [Evans et al., 2011b]. Also, the inclusion of SAW dissipation steepened the Alfvén speed profile in the lower corona, aligning the Alfvén profile better with observational constraints of shock formation.

Next, we modeled a CME in this new solar wind model [Evans et al., 2011c]. As with our previous CME simulation [Das et al., 2011, Evans et al., 2011a, Loesch et al., 2011], we did not model the initiation process. An eruption was generated by inserting an out-of-equilibrium flux rope at the base of the corona [Lugaz et al., 2007, Roussev et al., 2003b, Titov and Démoulin, 1999]. Because the flux rope traveled faster than the local magnetosonic speed, it acted as a piston and drove a shock wave ahead of it. A new result of this work was that the CME-driven shock had a strong impact on the solar wind environment through which it propagates. The CME alters the wave energy by concentrating it in the sheath through advection, and also increasing its value through momentum transfer. We demonstrated how Alfvén waves are focused into the sheaths of ICMEs. The wave energy is then dissipated at the shock due to surface Alfvén wave damping. The shock heating accounted for 10% of the total change in thermal energy of the CME. The resulting temperature distribution of the CME is more realistic than from a CME modeled in a polytropic solar wind.

In this thesis we explored CME features in the lower corona as well. In [Evans et al., 2011a], we studied the role of the flux rope magnetic field direction on the evolution of the CME in the lower corona. We found that observables such as the CME speed, the leading edge size and shape, and the angle between the shock normal and the magnetic field all varied when we varied the direction of the flux rope magnetic field with respect to the global coronal magnetic field. The shock normal angle is a crucial factor in the efficiency of partile acceleration by the shock. We determined that the different flux rope experienced different reconnection events with the active region and global coronal fields, and this resulted in different rotations of the ejecta during propagation in the lower corona. Additionally, we calculated the nonradial CME sheath flows, and found that their values at the back of the sheath varied with the ejecta field. In another work using the same simulation, we estimated how much solar wind material would be swept up by the ejecta as it expanded and propagated in the lower corona [Das et al., 2011]. We found that this compression at the back of the sheath was strong, and could play a role in accelerating particles in the lower corona.

In the future, the new steady state solar wind model presented in this thesis should be further validated and expanded upon (for example, by including waves in closed field regions, treating a spectrum of waves, and including additional wave dissipation mechanisms). As shown in this thesis, the solar wind background is extremely important to studying CME evolution. We know that CMEs place a crucial role in accelerating particles near and far from the Sun, and that their interaction with the Earth's magnetosphere has consequences for society which range from economical to public health. Therefore, in order to minimize their negative impact on society, it is crucial to the space weather community to understand how these eruptions evolve from eruption to 1 AU.

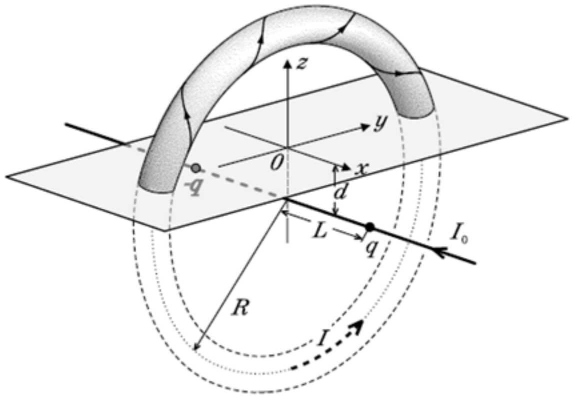

Figure A.1: The Titov-Demoulin flux rope model is an analytic solution for a stable flux system [Titov and Démoulin, 1999]. See text for details.

Appendix A: Titov-Demoulin Flux Rope Model

The TD model [Titov and Démoulin, 1999] is a complete analytic solution for a stable magnetic flux system, created from three sources, as in Fig. A.1. The first is a line current I running through a torus, which generates poloidal magnetic field. The torus, of major radius R and minor radius a, is placed with its axis parallel to and a distance d below the surface of the photosphere. The second is a set of opposite magnetic charges q, lying on the torus axis, mirrored a distance $2L$ from each other. These charges create an arcade field (B_q) to strap the torus. The final source is a subphotspheric line charge I_0 along the torus axis, which creates the axial (toroidal) field. The torus contains a mass M.

There are only two forces to consider: the Lorentz force between I and B_q, and the hoop curvature force. Both are directed normal to the axis, and can be written as:

$$F_L = -\frac{2qLI}{(R^2 + L^2)^{3/2}}, \tag{A.1}$$

$$F_C = \frac{\mu_0 I^2}{4\pi R} \left(ln(R/a) + ln8 - 3/2 + l_i/2 \right) \tag{A.2}$$

where l_i is the internal inductance per unit length, and is usually on the order of one [Titov and Démoulin, 1999].

The flux rope is then stable against eruption with a current:

$$I = \frac{8\pi qLR\left(R^2 + L^2\right)^{-3/2}}{\mu_0\left[ln\left(8R/a\right) - 3/2 + l_i/2\right]} \tag{A.3}$$

This analytic solution was implemented into the SWMF, and its eruptive properties were studied. Roussev et al. [2003b] found that an eruption could not be achieved with I_0 included, and so this current was removed (the resulting set up is referred to as a *modified TD flux rope*. By removing the field due to I_0, the flux rope becomes highly twisted (tens to hundreds of turns), in contrast to observations, which limit the number of twists to be only 1 or 2 [Gaizauskas, 1979]. However, the twisted flux rope inserted out of equilibrium was not guaranteed to result in an eruption. Roussev et al. [2003b] found that an eruption could be achieved when $R > \sqrt{2}L$.

Appendix B: Surface Alfvén Wave Damping

B.1 Theory

Here we show the derivation for the dissipation rate of surface Alfvén wave damping, used in Chapter 4. An alternate derivation to the one presented here (which results in the same expression) can be found in Lee and Roberts [1986].

We start by considering a cold[1] non-uniform plasma, and waves in the low frequency regime (frequencies much less than electron and ion cyclotron frequency). In this limit, the dielectric tensor for multiple ion species (labeled by α, with charge ϵ) derived using the Vlasov equation of distributions is found to be [Cramer, 2001]

$$K_{ij} = \begin{bmatrix} S & -iD & 0 \\ iD & S & 0 \\ 0 & 0 & P \end{bmatrix} \tag{B.1}$$

where

$$\begin{aligned} P &= 1 - \sum \tfrac{\omega_{p\alpha}^2}{\omega^2} \\ S &= \tfrac{1}{2}\left(R_+ + R_-\right) \\ D &= \tfrac{1}{2}\left(R_+ - R_-\right) \\ R_\pm &= 1 - \sum \tfrac{\omega_{p\alpha}^2}{\omega^2} \tfrac{\omega}{\omega \pm \epsilon_\alpha \Omega_\alpha}. \end{aligned} \tag{B.2}$$

The plasma frequency $\omega_{p\alpha}$ and gyrofrequency ω_α are defined as

$$\begin{aligned} \omega_{p\alpha}^2 &= \tfrac{n_\alpha e^2}{\epsilon_0 m_\alpha} \\ \Omega_\alpha &= \tfrac{Be}{m_\alpha}. \end{aligned} \tag{B.3}$$

[1]In the cold plasma limit, the pressure approaches zero (so sound speed and plasma beta are zero).

Now let us recast the dielectric tensor in components u_i which have dimensions of wave number squared:

$$K_{ij} = \frac{c^2}{\omega^2} \begin{bmatrix} u_1 & iu_2 & 0 \\ -iu_2 & u_1 & 0 \\ 0 & 0 & u_3 \end{bmatrix} \tag{B.4}$$

where

$$\begin{aligned} u_1 &= \tfrac{\omega^2}{c^2} S \\ u_2 &= \tfrac{\omega^2}{c^2} D \\ u_3 &= \tfrac{\omega^2}{c^2} P. \end{aligned} \tag{B.5}$$

The dispersion relation for a wave in the x-z plane and with $k_y = 0$ in the low frequency, large $|P|$ limit is

$$\begin{aligned} k^2 - k_z^2 &= k_x^2 \\ k_x^2 &= \tfrac{G^2 - H^2}{G} \\ G &= u_1 - k_z^2 \\ H &= u_2. \end{aligned} \tag{B.6}$$

In the very low frequency limit ω is much less than the magnitude of Ω_e, and so S and D become:

$$\begin{aligned} S &= 1 + \sum \tfrac{\omega_{p\alpha}^2}{\Omega_\alpha^2 - \omega^2} \\ G &= \sum \tfrac{\epsilon_\alpha \omega_{p\alpha}^2 \omega}{\Omega_\alpha (\Omega_\alpha^2 - \omega^2)}. \end{aligned} \tag{B.7}$$

We are in the regime where the Alfvén speed is much less than c, and this allows us to write the Alfvén speed as

$$\sum \frac{\omega_{p\alpha}^2}{\Omega^2} = \frac{c^2}{v_A^2} \tag{B.8}$$

and so the low frequency limit, D goes to 0 and S goes to

$$S = 1 + \frac{c^2}{v_A^2}. \tag{B.9}$$

Surface waves will exist in a region where there is an inhomogeneity in plasma parameters such as density or magnetic field either as a discontinuity or a finite layer. Assume a uniform magnetic field $B_0\mathbf{z}$, and a transition region of width a between two regions with densities ρ_{01} and ρ_{02}. The surface for the wave is the y-z plane. The transition region thickness ϵ must be narrow,

$$\epsilon = |k_z a| << 1 \tag{B.10}$$

The fields of the resulting surface wave are assumed to have imaginary k_x in the surrounding uniform plasmas, and therefore decay like $exp(-k_x x)$ away from the surface. This creates a wave that is localized in space on the surface, and therefore is called a surface wave.

We already found dispersion relation in the low frequency region for $k_y = 0$ which can be generalized to include nonzero k_y:

$$\begin{aligned} k^2 - k_z^2 - -k_y^2 &= k_x^2 \\ k_x^2 &= -k_y^2 + \tfrac{G^2 - H^2}{G}. \end{aligned} \tag{B.11}$$

Notice that this allows for one value of k_x^2, so as a consequence there is no mode conversion to magnetosonic modes. The boundary conditions on the electric and magnetic fields are that the components tangent to the y-z plane must be continuous at $x = 0$ and $x = -a$:

$$\begin{aligned} E_{y1} &= E_{y2} \\ B_{z1} &= B_{z2}. \end{aligned} \tag{B.12}$$

To use these conditions we must first derive some differential equations for the wave fields, as always in the low frequency limit. Assume the plasma density is a function of x only. We begin with Maxwell's equations, and take the curl of both sides of Faraday's Law, then taking the partial time derivative of both sides of Ampere's Law and substituting the results into Faraday's Law yields the wave equation for the electric field [Cramer, 2001]:

$$\nabla \times \nabla \times \mathbf{E} = -\frac{\mathbf{1}}{\mathbf{c^2}}\frac{\partial^{\mathbf{2}}\mathbf{E}}{\partial \mathbf{t^2}} - \mu_{\mathbf{0}}\frac{\partial \mathbf{J}}{\partial \mathbf{t}} \tag{B.13}$$

We Fourier transform this equation by saying the fields go like $exp(ik \cdot r - i\omega t)$, which means the following operations transform like

$$\begin{aligned} \nabla &= ik \\ \tfrac{d}{dt} &= -i\omega \end{aligned} \tag{B.14}$$

to obtain:

$$\mathbf{k} \times \mathbf{k} \times \mathbf{E} = -\frac{\omega^{\mathbf{2}}}{\mathbf{c^2}}\mathbf{E} - \mathbf{i}\omega\mu_{\mathbf{0}}\mathbf{J} \tag{B.15}$$

The Fourier transform of J induced by E using kinetic theory (meaning not treating the ions and electrons as a single fluid, as in MHD) is given by [Cramer, 2001]:

$$J_i\left(\omega, k\right) = \sigma_{ij}\left(\omega, k\right) E_j\left(\omega, k\right). \tag{B.16}$$

This J is expressed in terms of the conductivity tensor, which can be related to the dielectric tensor like

$$K_{ij} = \delta_{ij} + \frac{i}{\epsilon_0 \omega}\sigma_{ij}. \tag{B.17}$$

The Fourier transform from above can now be written as:

$$\begin{aligned} k^2 E_j &= \tfrac{\omega^2}{c^2} E_j - i\omega\mu_0\sigma_{ij} E_j \\ k^2 E_j &= \tfrac{\omega^2}{c^2} E_j - i\omega\mu_0 \tfrac{\epsilon_0\omega}{i}\left(K_{ij} + \delta_{ij}\right) E_j \\ \tfrac{c^2}{\omega^2}\left(k_i k_j - k^2\delta_{ij} + K_{ij}\right) E_j &= 0. \end{aligned} \tag{B.18}$$

The above expression gives the dispersion equation when you seek the nontrivial solution of this equation (E_j nonzero) by setting the determinant of the brackets to zero.

We can write differential equations for E_y and B_z (assuming constant ω, k_y and k_z):

$$\begin{aligned} \tfrac{dE_y}{dx} - \tfrac{k_y H}{G} E_y &= i\omega \tfrac{G - ik_y^2}{G} B_z \\ \tfrac{dB_z}{dx} + \tfrac{k_y H}{G} B_z &= \tfrac{i}{\omega} \tfrac{G^2 - H^2}{G} E_y. \end{aligned} \tag{B.19}$$

Note that in the above equations, G and H are functions of x.

In the uniform plasma region on either side of the surface, the waves are damped which we guarantee by requiring k_x^2 is less than zero. This means that our fields are going like $exp(i|k_x|x)$, so in the first differential equation above,

$$\frac{dE_y}{dx} = i|k_x|E_y. \tag{B.20}$$

The equations above can be rewritten as:

$$\begin{aligned} i\omega B_z &= \tfrac{i|k_x|G - k_y H}{G - k_y^2} E_y \\ \tfrac{i}{\omega} E_y &= \tfrac{i|k_x|G + k_y G}{G^2 - H^2} B_z. \end{aligned} \tag{B.21}$$

These are the fields inside the plasma. These solutions must match the solution inside the transition region, which for us is a surface of width a. We solve for the fields inside by utilizing perturbation theory. We assume that all wavelengths we consider in the surface plane are much longer than a, so we can expand the fields to first order in the small parameter $\epsilon = |k_z a|$ (exactly the parameter discussed when first describing the transition region.)

The zero order terms in the expansion are what we would have if it we were treating a discontinuity: a infinitely sharp jump from one plasma density to another. The first order terms are the corrections for our finite width a of our transition. The field expansions are:

$$\begin{aligned} E_y &= E_0 + \epsilon E_1 \\ B_z &= k_z(\psi_0 + \epsilon\psi_1). \end{aligned} \tag{B.22}$$

where the ψ_ns are the magnetic field explicitly as a wave vector.

Introducing the normalized variable $\bar{x} = \frac{x}{a}$, the equations can be recast like:

$$\begin{aligned} \frac{dE_0}{d\bar{x}} &= 0 \\ \frac{dE_1}{d\bar{x}} - \frac{k_y H}{k_z G} E_0 &= i\omega \frac{G - k_y^2}{G} \psi_0 \\ \frac{k\psi_0}{d\bar{x}} &= 0 \\ \frac{d\psi_1}{d\bar{x}} + \frac{k_y H}{k_z G} \psi_0 &= \frac{i}{\omega} \frac{G^2 - H^2}{k_z^2 G^2} E_0. \end{aligned} \tag{B.23}$$

Recast these differential equations as integrals with limit from zero to $\bar{x}$ to see where the damping enters:

$$\begin{aligned} E_1(\bar{x}) &= \frac{1}{k_z} \int d\bar{x} \left(\frac{k_y H}{G} E_0 + i\omega \frac{G - k_y^2}{G} \psi_0 \right) \\ \psi_1(\bar{x}) &= \frac{1}{k_z^2} \int d\bar{x} \left(\frac{i}{\omega} \frac{G^2 - H^2}{G^2} E_0 - \frac{k_z k_y H}{G} \psi_0 \right). \end{aligned} \tag{B.24}$$

The attenuation of the waves is apparent here as the zero of G will contribute to the integral as the residues of the poles. The residues will give imaginary components to E_1 and ψ_1. The zero G is the same as the Alfvén resonance condition, and so the damping is a resonance absorption of the wave. Here we have not considered the mechanism for dissipating the energy.

Now we must satisfy the boundary conditions by matching the solutions at $x = 0$, $x = -a$. When we do so, we find

$$\begin{aligned} E_p \exp -k_p a &= E_{y0} + \epsilon E_{y1}(-1) \\ B_p \exp -k_p a &= k_z \left(\psi_0 + \epsilon \psi_1(-1)\right). \end{aligned} \tag{B.25}$$

These conditions will yield the dispersion relation:

$$\begin{aligned} D\left(\omega - i\gamma\right) &= D_0\left(\omega - i\gamma\right) \epsilon D_1\left(\omega - i\gamma\right) \\ D\left(\omega - i\gamma\right) &= \tfrac{k_p G_p - k_y H_p}{G_p - k_y^2} + \tfrac{k_z^2}{k_v} \end{aligned} \tag{B.26}$$
$$+\epsilon\left(\tfrac{k_z}{a}\int dx \tfrac{1}{G}\left[-2\tfrac{k_y}{k_v}H + \tfrac{G^2 - H^2}{k_z^2} + \tfrac{k_z^2}{k_v^2}(G - k_v^2)\right]\right).$$

Now, we can write the damping rate of the surface wave to first order in as an expansion around the real components of the frequency, evaluated at the surface wave frequency (where $D_0 = 0$):

$$\gamma = \epsilon \frac{Im\left(D_1(\omega)\right)}{\frac{\partial D_0}{\partial \omega}} \tag{B.27}$$

This damping rate is found, as previously discussed, by evaluating the contribution of the residue of the pole,

$$\gamma = -\epsilon\pi \frac{\left(H + k_z^2 k_y / k_v\right)^2}{k_z \frac{\partial D_0}{\partial \omega} \frac{dG}{d\bar{x}}} \tag{B.28}$$

In the low frequency regime, we found that D goes to zero and S can be rewritten, which means that:

$$\begin{aligned} G &= \tfrac{\omega^2}{v_A^2} - k_z^2 \\ H &= 0 \end{aligned} \tag{B.29}$$

which means that the dispersion relation is

$$D_0\left(\omega\right) = \frac{k_z^2 - \omega^2/v_A^2}{k_p} + \frac{k_z^2}{k_v}. \tag{B.30}$$

Setting this expression equal to zero and solving for the Alfvén surface wave frequency gives:

$$\omega_s^2 = v_A^2 k_z^2 \left(\frac{2k_y^2 + k_z^2}{k_y^2 + k_z^2}\right) \tag{B.31}$$

In the limit that k_y is much larger than k_z, we find:

$$\omega_s = \sqrt{2} v_A k_z. \tag{B.32}$$

We finally arrive at the damping rate

$$\gamma = \frac{\pi}{8}\left(k_y a\right)\omega_s \tag{B.33}$$

By considering a rapidly expanding flux tube of width a, Alfvén waves [Lee and Roberts, 1986] arrived at a damping rate of

$$\Gamma_{SW} = \pi(\bar{k}a)\left(\frac{\omega_2^2 - \omega_1^2}{8\omega}\right) \tag{B.34}$$

where $\bar{k}$ is the average wave number, ω is the frequency and ω_1 and ω_2 are the frequency on either side of the flux tube (1 representing inside and 2 outside.)

The surface Alfvén wave damping length can be written as the Alfvén speed $v_A = \sqrt{\frac{B^2}{4\pi\rho}}$ divided by the damping rate. Following Jatenco-Pereira and Opher [1989], we assume: the width of the flux tube to be much smaller than the radius ($\bar{k}a = 0.1$), a strong gradient in

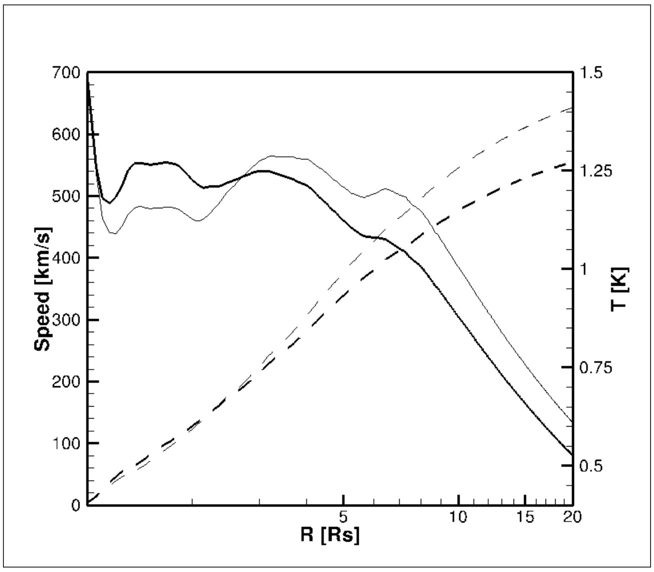

Figure B.1: Investigation of the effect of the free parameter. The solar wind speed (dashed) and temperature (solid) are plotted as a function of radial distance, extracted along a radial line at 60° latitude. The thick lines corresponds to a simulation with stronger wave dissipation [Evans et al., 2011b].

density (ω_1 much larger than ω_2), and that the frequency is constant with height. Utilizing the relation that $a \propto A(r)^{\frac{1}{2}} \propto r^{\frac{S}{2}}$ (where S is the superradial expansion factor of the field line), Jatenco-Pereira and Opher [1989] found the damping length to be:

$$L_{SW} = L_0 \left(\frac{r_0}{r}\right)^{\frac{S}{2}} \left(\frac{v_A}{v_{A0}}\right)^2 (1 + M_A) \tag{B.35}$$

where $M_A = \frac{u_{SW}}{v_A}$ is the Alfvén Mach Number. The subscript 0 indicates the variable is to be evaluated at the reference height. The damping length at the lower boundary is $L_0 = 18\frac{v_{A0}}{\omega}$.

B.2 Free Parameter of Surface Alfvén Wave Dissipation

In the formalism presented in this thesis, wave dissipation by surface Alfvén wave damping contains a free parameter (C_{SW}). This parameter is used to gauge the strength of the dissipation. In this section, we investigate of the effect of changing this quantity.

In Fig. B.1, the temperature (solid line) and solar wind speed (dashed line) are plotted as a function of heliocentric distance, extracted along a radial line at 60° latitude. We chose this location because surface Alfvén wave dissipation is strong in this region. The black line corresponds to a simulation with stronger wave dissipation ($C_{SW} = 8$) and weaker dissipation in the gray line ($C_{SW} = 10$).

The effect of increasing the strength of SAW damping on the solar wind speed was to increase its value near the Sun, and reduce its terminal value. This behavior is in agreement with the expected behavior of depositing energy in a stellar wind below the sonic point [Hartmann and MacGregor, 1980]. We find that the temperature is also larger close to and smaller far from the Sun when the dissipation rate is increased.

Appendix C: Comparison of Solar Wind Model to Observations

C.1 Ulysses Data

Ulysses data indirectly supports the presence of low (subpolar) latitude heating. Following Goldstein et al. [1996], we scaled 1-hour averaged Solar Wind over the Sun (SWOOPS) ion radial temperature data (from the first fast latitude scan, 1994-1995) by performing a power law fit to data for which $v > 700km/s$ and $r = 1.55 - 3.03$ AU, separately in each hemisphere. We found a temperature falloff of $r^{-0.921}$ and $r^{-1.083}$ in the south and north poles, respectively. (The values reported in Goldstein et al. [1996] were $r^{-0.81}$ and $r^{-1.03}$). The Ulysses data, scaled to 1 AU, is shown as the solid black line in panel a of Fig. C.1. We applied a linear fit (yellow lines) to the scaled Ulysses data to determine whether the latitudinal temperature profile in the fast solar wind, from the poles towards the equator, decreased (as would be expected if heating is strongest at the poles) or increased (as would be expected if heating occurs at mid and low latitudes). We found that in both the northern and southern hemisphere, the temperature is almost constant with latitude, except for a slight increase towards the boundary. This suggests that something special is happening at the boundary of fast and slow solar wind, which we propose is due to both SAW dissipation close to the Sun (as calculated in this paper).

The fitting we performed is different than what was originally presented in [McComas et al., 2000]. The value reported there was the average latitudinal temperature, computed over 8 segments of Ulysses's orbit, from 1992 February - 1997 December. The value reported for protons was an average of $2.7 \times 10^5 K$ at $60°$, with a latitudinal dependence of $+223$ K per degree in latitude (i. e., increasing towards the poles). For alpha particles, however, the temperature increased from the pole to the equator: the value reported was an average of $1.4 \times 10^5 K$ at $60°$, with a latitudinal dependence of -871 K per degree in latitude.

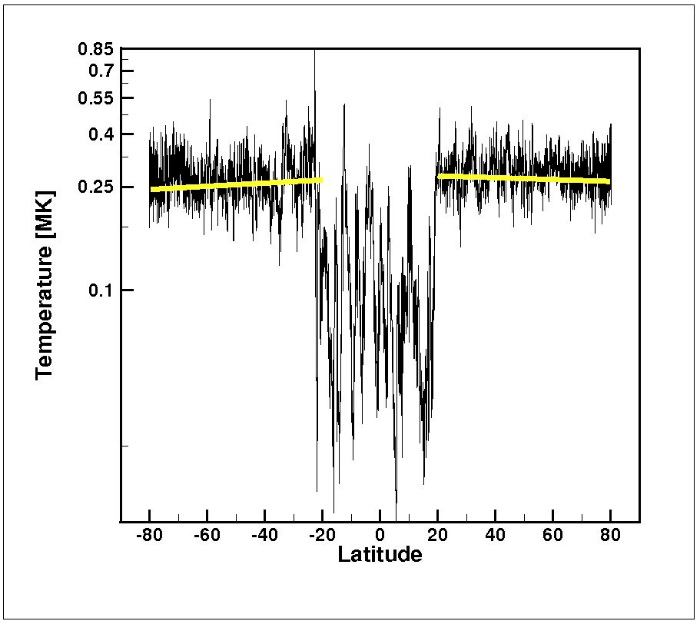

Figure C.1: Ion temperature measurements from the Ulysses first fast latitude scan. We have scaled the data to 1 AU, and performed linear fits to the fast wind in each hemisphere. The yellow line shows the resulting fits, which both have positive slopes in the pole to equator direction [Evans et al., 2011b].

Although the temperature at $R = 0.1AU$ has not been measured in situ, we can make an estimate of the temperature in the fast solar wind by assuming that the radial behavior we calculated at 1 AU can be used to scale the temperature to 0.1 AU. The result is $T = 2.8MK$. This large value (the maximum temperature in the entire simulation is $T = 2.9MK$) suggests that the radial scaling is not valid close in. In the simulation which includes surface Alfven wave and turbulent dissipation, the temperature at 0.1 AU at 60° latitude is 0.6 MK.

C.2 Semiempirical Model

In Chapter 4, we compare the Alfven speed profile from our model with a semiempirical model (herein MAN03). MAN03 defines a profile of Alfven speed near an active region as a function of distance, r, above the surface, in units of solar radii [Mann et al., 2003]. The magnetic field strength is expressed analytically as an active region field superimposed on quiet Sun dipole:

$$|B| = B_1 * (1-r)^{-3} + B_2 * r^{-2} \tag{C.1}$$

where $B_1 = 0.005$ to match the strength of the active region in CR2077: 40 Gauss (G). The second term was set $B_2 = 2.2G$, a typical value for the quiet Sun field. Above $R = 1.8R_\odot$, the quiet Sun field dominates.

The density in MAN03 is modeled as a one-fold Newkirk model [Newkirk, 1961] for $R < 1.8R_\odot$,

$$N(r) = 1.92 * 4.2 \times 10^4 \left(10^{4.32 * r^{-1}}\right) \tag{C.2}$$

above which they use the empirical form of Mann et al. [1999],

$$N(r) = 1.92 * 5.14 \times 10^9 \exp(13.8 * (r^{-1} - 1)). \tag{C.3}$$

Bibliography

Bibliography

V. Airapetian, K. G. Carpenter, and L. Ofman. Winds from Luminous Late-type Stars. II. Broadband Frequency Distribution of Alfvén Waves. *Astrophys. J.,*, 723:1210–1218, November 2010. doi: 10.1088/0004-637X/723/2/1210.

V. Airapetian, L. Ofman, E. C. Sittler, and M. Kramar. Probing the Thermodynamics and Kinematics of Solar Coronal Streamers. *Astrophys. J.,*, 728:67–+, February 2011. doi: 10.1088/0004-637X/728/1/67.

M. D. Altschuler and G. Newkirk. Magnetic Fields and the Structure of the Solar Corona. I: Methods of Calculating Coronal Fields. *Solar Phys.,*, 9:131–149, September 1969. doi: 10.1007/BF00145734.

S. K. Antiochos, C. R. DeVore, and J. A. Klimchuk. A Model for Solar Coronal Mass Ejections. *Astrophys. J.,*, 510:485–493, January 1999. doi: 10.1086/306563.

C. N. Arge and V. J. Pizzo. Improvement in the prediction of solar wind conditions using near-real time solar magnetic field updates. *J. Geophys. Res.,*, 105:10465–10480, May 2000. doi: 10.1029/1999JA900262.

C. N. Arge, D. Odstrcil, V. J. Pizzo, and L. R. Mayer. Improved Method for Specifying Solar Wind Speed Near the Sun. In M. Velli, R. Bruno, F. Malara, & B. Bucci, editor, *Solar Wind Ten*, volume 679 of *American Institute of Physics Conference Series*, pages 190–193, September 2003. doi: 10.1063/1.1618574.

M. J. Aschwanden, R. W. Nightingale, J. Andries, M. Goossens, and T. Van Doorsselaere.

Observational Tests of Damping by Resonant Absorption in Coronal Loop Oscillations. *Astrophys. J.,*, 598:1375–1386, December 2003. doi: 10.1086/379104.

M. Banaszkiewicz, W. I. Axford, and J. F. McKenzie. An analytic solar magnetic field model. *Astron. Astrophys.,*, 337:940–944, September 1998.

J. W. Belcher. ALFVÉNIC Wave Pressures and the Solar Wind. *Astrophys. J.,*, 1971.

J. W. Belcher and L. Davis, Jr. Large-amplitude Alfvén waves in the interplanetary medium, 2. *J. Geophys. Res.,*, 1971.

L. Biermann. Kometenschweife und solare Korpuskularstrahlung. *Zeitschrift fuer Astrophysik,*, 29:274–+, 1951.

M. M. Bisi, B. V. Jackson, P. P. Hick, A. Buffington, J. M. Clover, M. Tokumaru, and K. Fujiki. Three-dimensional Reconstructions and Mass Determination of the 2008 June 2 LASCO Coronal Mass Ejection Using STELab Interplanetary Scintillation Observations. *Astrophys. J.,*, 715:L104–L108, June 2010a. doi: 10.1088/2041-8205/715/2/L104.

M. M. Bisi, A. R. Breen, B. V. Jackson, R. A. Fallows, A. P. Walsh, Z. Mikić, P. Riley, C. J. Owen, A. Gonzalez-Esparza, E. Aguilar-Rodriguez, H. Morgan, E. A. Jensen, A. G. Wood, M. J. Owens, M. Tokumaru, P. K. Manoharan, I. V. Chashei, A. S. Giunta, J. A. Linker, V. I. Shishov, S. A. Tyul'Bashev, G. Agalya, S. K. Glubokova, M. S. Hamilton, K. Fujiki, P. P. Hick, J. M. Clover, and B. Pintér. From the Sun to the Earth: The 13 May 2005 Coronal Mass Ejection. *Solar Phys.,*, 265:49–127, August 2010b. doi: 10.1007/s11207-010-9602-8.

V. Bothmer and R. Schwenn. The structure and origin of magnetic clouds in the solar wind. *Annales Geophysicae*, 16:1–24, January 1998. doi: 10.1007/s00585-997-0001-x.

D. H. Brooks and H. P. Warren. Establishing a Connection Between Active Region Outflows and the Solar Wind: Abundance Measurements with EIS/Hinode. *Astrophys. J.,*, 727: L13+, January 2011. doi: 10.1088/2041-8205/727/1/L13.

L. Burlaga, E. Sittler, F. Mariani, and R. Schwenn. Magnetic loop behind an interplanetary shock - Voyager, Helios, and IMP 8 observations. *J. Geophys. Res.,*, 86:6673–6684, August 1981. doi: 10.1029/JA086iA08p06673.

L. F. Burlaga. Magnetic clouds and force-free fields with constant alpha. *J. Geophys. Res.,*, 93:7217–7224, July 1988. doi: 10.1029/JA093iA07p07217.

J. P. Byrne, S. A. Maloney, R. T. J. McAteer, J. M. Refojo, and P. T. Gallagher. Propagation of an Earth-directed coronal mass ejection in three dimensions. *Nature Communications*, 1, September 2010. doi: 10.1038/ncomms1077.

H. V. Cane and W. C. Erickson. Solar Type II Radio Bursts and IP Type II Events. *Astrophys. J.,*, 623:1180–1194, April 2005. doi: 10.1086/428820.

S. Casalbuoni, L. Del Zanna, S. R. Habbal, and M. Velli. Coronal plumes and the expansion of pressure-balanced structures in the fast solar wind. *J. Geophys. Res.,*, 104:9947–9962, May 1999. doi: 10.1029/1999JA900047.

A. W. Case, H. E. Spence, M. J. Owens, P. Riley, and D. Odstrcil. Ambient solar wind's effect on ICME transit times. *Geophys. Res. Lett.,*, 35:L15105, August 2008. doi: 10.1029/2008GL034493.

B. D. G. Chandran and J. V. Hollweg. Alfvén Wave Reflection and Turbulent Heating in the Solar Wind from 1 Solar Radius to 1 AU: An Analytical Treatment. *Astrophys. J.,*, 707:1659–1667, December 2009. doi: 10.1088/0004-637X/707/2/1659.

B. D. G. Chandran, P. Pongkitiwanichakul, P. A. Isenberg, M. A. Lee, S. A. Markovskii, J. V. Hollweg, and B. J. Vasquez. Resonant Interactions Between Protons and Oblique Alfvén/Ion-cyclotron Waves in the Solar Corona and Solar Flares. *Astrophys. J.,*, 722: 710–720, October 2010. doi: 10.1088/0004-637X/722/1/710.

J. Chen. Effects of toroidal forces in current loops embedded in a background plasma. *Astrophys. J.,*, 338:453–470, March 1989. doi: 10.1086/167211.

J. W. Cirtain, L. Golub, L. Lundquist, A. van Ballegooijen, A. Savcheva, M. Shimojo, E. DeLuca, S. Tsuneta, T. Sakao, K. Reeves, M. Weber, R. Kano, N. Narukage, and K. Shibasaki. Evidence for Alfvén Waves in Solar X-ray Jets. *Science*, 318:1580–, December 2007. doi: 10.1126/science.1147050.

H. T. Claßen and H. Aurass. On the association between type II radio bursts and CMEs. *Astron. Astrophys.,*, 384:1098–1106, March 2002. doi: 10.1051/0004-6361:20020092.

E. W. Cliver, D. F. Webb, and R. A. Howard. On the origin of solar metric type II bursts. *Solar Phys.,*, 187:89–114, June 1999.

O. Cohen, I. V. Sokolov, I. I. Roussev, C. N. Arge, W. B. Manchester, T. I. Gombosi, R. A. Frazin, H. Park, M. D. Butala, F. Kamalabadi, and M. Velli. A Semiempirical Magnetohydrodynamical Model of the Solar Wind. *Astrophys. J.,*, 654:L163–L166, January 2007. doi: 10.1086/511154.

O. Cohen, I. V. Sokolov, I. I. Roussev, and T. I. Gombosi. Validation of a synoptic solar wind model. *Journal of Geophysical Research (Space Physics)*, 113:3104–+, March 2008. doi: 10.1029/2007JA012797.

O. Cohen, G. D. R. Attrill, N. A. Schwadron, N. U. Crooker, M. J. Owens, C. Downs, and T. I. Gombosi. Numerical Simulation of the May 12, 1997 CME Event - the Role of Magnetic Reconnection. *ArXiv e-prints*, June 2010.

R. C. Colaninno and A. Vourlidas. First Determination of the True Mass of Coronal Mass Ejections: A Novel Approach to Using the Two STEREO Viewpoints. *Astrophys. J.,*, 698:852–858, June 2009. doi: 10.1088/0004-637X/698/1/852.

N. F. Cramer. *The Physics of Alfvén Waves.* December 2001.

S. R. Cranmer. An Efficient Approximation of the Coronal Heating Rate for use in Global Sun-Heliosphere Simulations. *Astrophys. J.,*, 710:676–688, February 2010. doi: 10.1088/0004-637X/710/1/676.

S. R. Cranmer and A. A. van Ballegooijen. On the Generation, Propagation, and Reflection of Alfvén Waves from the Solar Photosphere to the Distant Heliosphere. *Astrophys. Space Sci.,*, 156:265–293, February 2005. doi: 10.1086/426507.

S. R. Cranmer, G. B. Field, and J. L. Kohl. Spectroscopic Constraints on Models of Ion Cyclotron Resonance Heating in the Polar Solar Corona and High-Speed Solar Wind. *Astrophys. J.,*, 518:937–947, June 1999. doi: 10.1086/307330.

S. R. Cranmer, A. A. van Ballegooijen, and R. J. Edgar. Self-consistent Coronal Heating and Solar Wind Acceleration from Anisotropic Magnetohydrodynamic Turbulence. *Astrophys. Space Sci.,*, 171:520–551, August 2007. doi: 10.1086/518001.

A. Dal Lago, R. Schwenn, and W. D. Gonzalez. Relation between the radial speed and theexpansion speed of coronal mass ejections. *Advances in Space Research*, 32:2637–2640, 2003. doi: 10.1016/j.asr.2003.03.012.

I. Das, M. Opher, R. Evans, C. Loesch, and T. I. Gombosi. Evolution of Piled-up Compressions in Modeled Coronal Mass Ejection Sheaths and the Resulting Sheath Structures. *Astrophys. J.,*, 729:112–+, March 2011. doi: 10.1088/0004-637X/729/2/112.

S. Dasso, M. S. Nakwacki, P. Démoulin, and C. H. Mandrini. Progressive Transformation of a Flux Rope to an ICME. Comparative Analysis Using the Direct and Fitted Expansion Methods. *Solar Phys.,*, 244:115–137, August 2007. doi: 10.1007/s11207-007-9034-2.

M. A. Dayeh, M. I. Desai, J. R. Dwyer, H. K. Rassoul, G. M. Mason, and J. E. Mazur. Composition and Spectral Properties of the 1 AU Quiet-Time Suprathermal Ion Population During Solar Cycle 23. *Astrophys. J.,*, 693:1588–1600, March 2009. doi: 10.1088/0004-637X/693/2/1588.

B. De Pontieu, P. C. H. Martens, and H. S. Hudson. Chromospheric Damping of Alfvén Waves. *Astrophys. J.,*, 558:859–871, September 2001. doi: 10.1086/322408.

B. De Pontieu, S. W. McIntosh, M. Carlsson, V. H. Hansteen, T. D. Tarbell, C. J. Schrijver, A. M. Title, R. A. Shine, S. Tsuneta, Y. Katsukawa, K. Ichimoto, Y. Suematsu, T. Shimizu, and S. Nagata. Chromospheric Alfvénic Waves Strong Enough to Power the Solar Wind. *Science*, 318:1574–, December 2007. doi: 10.1126/science.1151747.

P. Démoulin and S. Dasso. Causes and consequences of magnetic cloud expansion. *Astron. Astrophys.*,, 498:551–566, May 2009. doi: 10.1051/0004-6361/200810971.

M. I. Desai, G. M. Mason, J. R. Dwyer, J. E. Mazur, R. E. Gold, S. M. Krimigis, C. W. Smith, and R. M. Skoug. Evidence for a Suprathermal Seed Population of Heavy Ions Accelerated by Interplanetary Shocks near 1 AU. *Astrophys. J.*,, 588:1149–1162, May 2003. doi: 10.1086/374310.

R. L. Dewar. Interaction between Hydromagnetic Waves and a Time-Dependent, Inhomogeneous Medium. *Physics of Fluids*, 13:2710–2720, November 1970. doi: 10.1063/1.1692854.

D. Dobrzycka, S. R. Cranmer, A. V. Panasyuk, L. Strachan, and J. L. Kohl. Study of the latitudinal dependence of H I Lyman α and O VI emission in the solar corona: Evidence for the superradial geometry of the outflow in the polar coronal holes. *J. Geophys. Res.*,, 104:9791–9800, May 1999. doi: 10.1029/1998JA900129.

C. Downs, I. I. Roussev, B. van der Holst, N. Lugaz, I. V. Sokolov, and T. I. Gombosi. Toward a Realistic Thermodynamic Magnetohydrodynamic Model of the Global Solar Corona. *Astrophys. J.*,, 712:1219–1231, April 2010. doi: 10.1088/0004-637X/712/2/1219.

M. Dryer, S. T. Wu, R. S. Steinolfson, and R. M. Wilson. Magnetohydrodynamic models of coronal transients in the meridional plane. II - Simulation of the coronal transient of 1973 August 21. *Astrophys. J.*,, 227:1059–1071, February 1979. doi: 10.1086/156813.

J. K. Edmondson. On the Role of Interchange Reconnection in the Generation of the Slow Solar Wind. *Space Sci. Rev.*,, pages 38–+, March 2011. doi: 10.1007/s11214-011-9767-y.

R. Esser, S. Fineschi, D. Dobrzycka, S. R. Habbal, R. J. Edgar, J. C. Raymond, J. L. Kohl, and M. Guhathakurta. Plasma Properties in Coronal Holes Derived from Measurements of Minor Ion Spectral Lines and Polarized White Light Intensity. *Astrophys. J.,*, 510: L63–L67, January 1999. doi: 10.1086/311786.

R. M. Evans, M. Opher, W. B. Manchester, IV, and T. I. Gombosi. Alfvén Profile in the Lower Corona: Implications for Shock Formation. *Astrophys. J.,*, 687:1355–1362, November 2008. doi: 10.1086/592016.

R. M. Evans, M. Opher, V. Jatenco-Pereira, and T. I. Gombosi. Surface Alfvén Wave Damping in a Three-Dimensional Simulation of the Solar Wind. *Astrophys. J.,*, 703: 179–186, September 2009. doi: 10.1088/0004-637X/703/1/179.

R. M. Evans, M. Opher, and T. I. Gombosi. Learning from the Outer Heliosphere: Interplanetary Coronal Mass Ejection Sheath Flows and the Ejecta Orientation in the Lower Corona. *Astrophys. J.,*, 728:41–+, February 2011a. doi: 10.1088/0004-637X/728/1/41.

R. M. Evans, M. Opher, R. Oran, B. van der Holst, I. Sokolov, R. A. Frazin, and T. I. Gombosi. Coronal Heating by Surface Alfven Wave Damping: Implementation in MHD Modeling and Connection to Observations. *in prep* , 2011b.

R. M. Evans, M. Opher, and B. van der Holst. Interaction of a Coronal Mass Ejection-Driven Shock with an Alfven Wave Driven Solar Wind in the Lower Corona. *in prep* , 2011c.

F. Fang, W. Manchester, W. P. Abbett, and B. van der Holst. Simulation of Flux Emergence from the Convection Zone to the Corona. *Astrophys. J.,*, 714:1649–1657, May 2010. doi: 10.1088/0004-637X/714/2/1649.

T. G. Forbes. A review on the genesis of coronal mass ejections. *J. Geophys. Res.,*, 105: 23153–23166, October 2000. doi: 10.1029/2000JA000005.

T. G. Forbes, J. A. Linker, J. Chen, C. Cid, J. Kóta, M. A. Lee, G. Mann, Z. Mikić, M. S. Potgieter, J. M. Schmidt, G. L. Siscoe, R. Vainio, S. K. Antiochos, and P. Riley. CME

Theory and Models. *Space Sci. Rev.,*, 123:251–302, March 2006. doi: 10.1007/s11214-006-9019-8.

V. Gaizauskas. Braided structures observed in flare-associated H alpha filaments. In E. Jensen, P. Maltby, & F. Q. Orrall, editor, *IAU Colloq. 44: Physics of Solar Prominences*, pages 272–275, 1979.

J. Giacalone. The Efficient Acceleration of Thermal Protons by Perpendicular Shocks. *Astrophys. J.,*, 628:L37–L40, July 2005. doi: 10.1086/432510.

S. E. Gibson and B. C. Low. A Time-Dependent Three-Dimensional Magnetohydrodynamic Model of the Coronal Mass Ejection. *Astrophys. J.,*, 493:460–+, January 1998. doi: 10.1086/305107.

S. E. Gibson, L. Fletcher, G. Del Zanna, C. D. Pike, H. E. Mason, C. H. Mandrini, P. Démoulin, H. Gilbert, J. Burkepile, T. Holzer, D. Alexander, Y. Liu, N. Nitta, J. Qiu, B. Schmieder, and B. J. Thompson. The Structure and Evolution of a Sigmoidal Active Region. *Astrophys. J.,*, 574:1021–1038, August 2002. doi: 10.1086/341090.

B. E. Goldstein, M. Neugebauer, J. L. Phillips, S. Bame, J. T. Gosling, D. McComas, Y.-M. Wang, N. R. Sheeley, and S. T. Suess. ULYSSES plasma parameters: latitudinal, radial, and temporal variations. *Astron. Astrophys.,*, 316:296–303, December 1996.

H. Goldstein. On the field configuration in magnetic clouds. In *NASA Conference Publication*, volume 228 of *NASA Conference Publication*, pages 731–733, November 1983.

T. I. Gombosi, editor. *Physics of the space environment*, 1998.

N. Gopalswamy and M. L. Kaiser. Solar eruptions and long wavelength radio bursts: The 1997 May 12 event. *Advances in Space Research*, 29:307–312, 2002. doi: 10.1016/S0273-1177(01)00589-0.

N. Gopalswamy and S. Yashiro. The Strength and Radial Profile of the Coronal Magnetic

Field from the Standoff Distance of a Coronal Mass Ejection-driven Shock. *Astrophys. J.,*, 736:L17+, July 2011. doi: 10.1088/2041-8205/736/1/L17.

N. Gopalswamy, A. Lara, R. P. Lepping, M. L. Kaiser, D. Berdichevsky, and O. C. St. Cyr. Interplanetary acceleration of coronal mass ejections. *Geophys. Res. Lett.,*, 27:145–148, 2000. doi: 10.1029/1999GL003639.

N. Gopalswamy, A. Lara, M. L. Kaiser, and J.-L. Bougeret. Near-Sun and near-Earth manifestations of solar eruptions. *J. Geophys. Res.,*, 106:25261–25278, November 2001. doi: 10.1029/2000JA004025.

N. Gopalswamy, E. Aguilar-Rodriguez, S. Yashiro, S. Nunes, M. L. Kaiser, and R. A. Howard. Type II radio bursts and energetic solar eruptions. *Journal of Geophysical Research (Space Physics)*, 110:12–+, October 2005. doi: 10.1029/2005JA011158.

J. T. Gosling, E. Hildner, R. M. MacQueen, R. H. Munro, A. I. Poland, and C. L. Ross. Mass ejections from the sun - A view from SKYLAB. *J. Geophys. Res.,*, 79:4581–4587, November 1974. doi: 10.1029/JA079i031p04581.

J. T. Gosling, P. Riley, D. J. McComas, and V. J. Pizzo. Overexpanding coronal mass ejections at high heliographic latitudes - Observations and simulations. *J. Geophys. Res.,*, 103:1941–+, February 1998. doi: 10.1029/97JA01304.

J. T. Gosling, W.-L. Teh, and S. Eriksson. A Torsional Alfvén Wave Embedded Within a Small Magnetic Flux Rope in the Solar Wind. *Astrophys. J.,*, 719:L36–L40, August 2010. doi: 10.1088/2041-8205/719/1/L36.

R. R. Grall, W. A. Coles, M. T. Klinglesmith, A. R. Breen, P. J. S. Williams, J. Markkanen, and R. Esser. Rapid acceleration of the polar solar wind. *Nature,*, 379:429–432, February 1996. doi: 10.1038/379429a0.

C. P. T. Groth, D. L. De Zeeuw, T. I. Gombosi, and K. G. Powell. Global three-dimensional MHD simulation of a space weather event: CME formation, interplanetary propagation, and interaction with the magnetosphere. *J. Geophys. Res.,*, 105:25053–25078, November 2000. doi: 10.1029/2000JA900093.

M. Guhathakurta, E. C. Sittler, and L. Ofman. Semiempirically derived heating function of the corona heliosphere during the Whole Sun Month. *Journal of Geophysical Research (Space Physics)*, 111:11215–+, November 2006. doi: 10.1029/2006JA011931.

D. K. Haggerty and E. C. Roelof. Impulsive Near-relativistic Solar Electron Events: Delayed Injection with Respect to Solar Electromagnetic Emission. *Astrophys. J.,*, 579:841–853, November 2002. doi: 10.1086/342870.

L. Hartmann and K. B. MacGregor. Momentum and energy deposition in late-type stellar atmospheres and winds. *Astrophys. J.,*, 242:260–282, November 1980. doi: 10.1086/158461.

A. Hasegawa and C. Uberoi. *The Alfvén wave.* 1982.

D. M. Hassler, I. E. Dammasch, P. Lemaire, P. Brekke, W. Curdt, H. E. Mason, J.-C. Vial, and K. Wilhelm. Solar Wind Outflow and the Chromospheric Magnetic Network. *Science*, 283:810–+, February 1999. doi: 10.1126/science.283.5403.810.

J. Heyvaerts and E. R. Priest. Coronal heating by phase-mixed shear Alfven waves. *Astron. Astrophys.,*, 117:220–234, January 1983.

J. V. Hollweg. Nonlinear Landau Damping of Alfvén Waves. *Physical Review Letters*, 27: 1349–1352, November 1971. doi: 10.1103/PhysRevLett.27.1349.

J. V. Hollweg. Transition region, corona, and solar wind in coronal holes. *J. Geophys. Res.,*, 91:4111–4125, April 1986. doi: 10.1029/JA091iA04p04111.

J. V. Hollweg. Resonance absorption of magnetohydrodynamic surface waves Physical discussion. *Astrophys. J.,*, 312:880–885, January 1987. doi: 10.1086/164934.

J. V. Hollweg, S. Jackson, and D. Galloway. Alfven waves in the solar atmosphere. III - Nonlinear waves on open flux tubes. *Solar Phys.,*, 75:35–61, January 1982. doi: 10.1007/BF00153458.

A. J. Hundhausen and R. A. Gentry. Numerical simulation of flare-generated disturbances in the solar wind. *J. Geophys. Res.,*, 74:2908–2918, 1969. doi: 10.1029/JA074i011p02908.

J. A. Ionson. Resonant absorption of Alfvenic surface waves and the heating of solar coronal loops. *Astrophys. J.,*, 226:650–673, December 1978. doi: 10.1086/156648.

P. A. Isenberg and T. G. Forbes. A Three-dimensional Line-tied Magnetic Field Model for Solar Eruptions. *Astrophys. J.,*, 670:1453–1466, December 2007. doi: 10.1086/522025.

P. A. Isenberg, M. A. Lee, and J. V. Hollweg. The kinetic shell model of coronal heating and acceleration by ion cyclotron waves: 1. Outward propagating waves. *J. Geophys. Res.,*, 106:5649–5660, April 2001. doi: 10.1029/2000JA000099.

C. Jacobs, I. I. Roussev, N. Lugaz, and S. Poedts. The Internal Structure of Coronal Mass Ejections: Are all Regular Magnetic Clouds Flux Ropes? *Astrophys. J.,*, 695:L171–L175, April 2009. doi: 10.1088/0004-637X/695/2/L171.

S. A. Jacques. Momentum and energy transport by waves in the solar atmosphere and solar wind. *Astrophys. J.,*, 215:942–951, August 1977. doi: 10.1086/155430.

V. Jatenco-Pereira and R. Opher. Effect of diverging magnetic fields on mass loss in late-type giant stars. *Astron. Astrophys.,*, 209:327–336, January 1989.

V. Jatenco-Pereira, R. Opher, and L. C. Yamamoto. The power density spectrum break in an Alfven wave-driven solar wind. *Astrophys. J.,*, 432:409–416, September 1994. doi: 10.1086/174579.

D. B. Jess, M. Mathioudakis, R. Erdélyi, P. J. Crockett, F. P. Keenan, and D. J. Christian. Alfvén Waves in the Lower Solar Atmosphere. *Science*, 323:1582–, March 2009. doi: 10.1126/science.1168680.

A. Klassen, V. Bothmer, G. Mann, M. J. Reiner, S. Krucker, A. Vourlidas, and H. Kunow. Solar energetic electron events and coronal shocks. *Astron. Astrophys.,*, 385:1078–1088, April 2002. doi: 10.1051/0004-6361:20020205.

J. A. Klimchuk. On Solving the Coronal Heating Problem. *Solar Phys.,*, 234:41–77, March 2006. doi: 10.1007/s11207-006-0055-z.

J. L. Kohl, G. Noci, E. Antonucci, G. Tondello, M. C. E. Huber, S. R. Cranmer, L. Strachan, A. V. Panasyuk, L. D. Gardner, M. Romoli, S. Fineschi, D. Dobrzycka, J. C. Raymond, P. Nicolosi, O. H. W. Siegmund, D. Spadaro, C. Benna, A. Ciaravella, S. Giordano, S. R. Habbal, M. Karovska, X. Li, R. Martin, J. G. Michels, A. Modigliani, G. Naletto, R. H. O'Neal, C. Pernechele, G. Poletto, P. L. Smith, and R. M. Suleiman. UVCS/SOHO Empirical Determinations of Anisotropic Velocity Distributions in the Solar Corona. *Astrophys. J.,*, 501:L127+, July 1998. doi: 10.1086/311434.

J. Kóta, W. B. Manchester, J. R. Jokipii, D. L. de Zeeuw, and T. I. Gombosi. Simulation of SEP Acceleration and Transport at CME-driven Shocks. In G. Li, G. P. Zank, & C. T. Russell, editor, *The Physics of Collisionless Shocks: 4th Annual IGPP International Astrophysics Conference*, volume 781 of *American Institute of Physics Conference Series*, pages 201–206, August 2005. doi: 10.1063/1.2032697.

K. A. Kozarev, K. E. Korreck, V. V. Lobzin, M. A. Weber, and N. A. Schwadron. Off-limb Solar Coronal Wavefronts from SDO/AIA Extreme-ultraviolet Observations: Implications for Particle Production. *Astrophys. J.,*, 733:L25+, June 2011. doi: 10.1088/2041-8205/733/2/L25.

M. M. Kuznetsova, M. Hesse, and D. Winske. Toward a transport model of collisionless magnetic reconnection. *J. Geophys. Res.,*, 105:7601–7616, April 2000. doi: 10.1029/1999JA900396.

M. M. Kuznetsova, M. Hesse, L. Rasatter, A. Taktakishvili, G. Toth, D. L. De Zeeuw,

A. Ridley, and T. I. Gombosi. Multiscale modeling of magnetospheric reconnection. *JGR*, 112(A10):A10210, 2007.

E. Landi, J. C. Raymond, M. P. Miralles, and H. Hara. Physical Conditions in a Coronal Mass Ejection from Hinode, Stereo, and SOHO Observations. *Astrophys. J.,*, 711:75–98, March 2010. doi: 10.1088/0004-637X/711/1/75.

J. E. Leake, T. D. Arber, and M. L. Khodachenko. Collisional dissipation of Alfvén waves in a partially ionised solar chromosphere. *Astron. Astrophys.,*, 442:1091–1098, November 2005. doi: 10.1051/0004-6361:20053427.

J.-Y. Lee, J. C. Raymond, Y.-K. Ko, and K.-S. Kim. Three-Dimensional Structure and Energy Balance of a Coronal Mass Ejection. *Astrophys. J.,*, 692:1271–1286, February 2009. doi: 10.1088/0004-637X/692/2/1271.

M. A. Lee and B. Roberts. On the behavior of hydromagnetic surface waves. *Astrophys. J.,*, 301:430–439, February 1986. doi: 10.1086/163911.

J. A. Linker, Z. Mikić, R. Lionello, P. Riley, T. Amari, and D. Odstrcil. Flux cancellation and coronal mass ejections. *Physics of Plasmas*, 10:1971–1978, May 2003. doi: 10.1063/1.1563668.

R. Lionello, J. A. Linker, and Z. Mikić. Multispectral Emission of the Sun During the First Whole Sun Month: Magnetohydrodynamic Simulations. *Astrophys. J.,*, 690:902–912, January 2009. doi: 10.1088/0004-637X/690/1/902.

Y. Liu, J. D. Richardson, J. W. Belcher, J. C. Kasper, and H. A. Elliott. Thermodynamic structure of collision-dominated expanding plasma: Heating of interplanetary coronal mass ejections. *Journal of Geophysical Research (Space Physics)*, 111:A01102, January 2006a. doi: 10.1029/2005JA011329.

Y. Liu, J. D. Richardson, J. W. Belcher, C. Wang, Q. Hu, and J. C. Kasper. Constraints on the global structure of magnetic clouds: Transverse size and curvature.

Journal of Geophysical Research (Space Physics), 111:A12S03, November 2006b. doi: 10.1029/2006JA011890.

Y. Liu, W. B. Manchester, J. D. Richardson, J. G. Luhmann, R. P. Lin, and S. D. Bale. Deflection flows ahead of ICMEs as an indicator of curvature and geoeffectiveness. *Journal of Geophysical Research (Space Physics)*, 113:A00B03, July 2008a. doi: 10.1029/2007JA012996.

Y. C.-M. Liu, M. Opher, O. Cohen, P. C. Liewer, and T. I. Gombosi. A Simulation of a Coronal Mass Ejection Propagation and Shock Evolution in the Lower Solar Corona. *Astrophys. J.,*, 680:757–763, June 2008b. doi: 10.1086/587867.

C. Loesch, M. Opher, M. V. Alves, R. M. Evans, and W. B. Manchester. Signatures of two distinct driving mechanisms in the evolution of coronal mass ejections in the lower corona. *Journal of Geophysical Research (Space Physics)*, 116:A04106, April 2011. doi: 10.1029/2010JA015582.

N. Lugaz, W. B. Manchester, IV, and T. I. Gombosi. Numerical Simulation of the Interaction of Two Coronal Mass Ejections from Sun to Earth. *Astrophys. J.,*, 634:651–662, November 2005. doi: 10.1086/491782.

N. Lugaz, W. B. Manchester, IV, I. I. Roussev, G. Tóth, and T. I. Gombosi. Numerical Investigation of the Homologous Coronal Mass Ejection Events from Active Region 9236. *Astrophys. J.,*, 659:788–800, April 2007. doi: 10.1086/512005.

N. Lugaz, A. Vourlidas, I. I. Roussev, C. Jacobs, W. B. Manchester, IV, and O. Cohen. The Brightness of Density Structures at Large Solar Elongation Angles: What Is Being Observed by STEREO SECCHI? *Astrophys. J.,*, 684:L111–L114, September 2008. doi: 10.1086/592217.

N. Lugaz, C. Downs, K. Shibata, I. I. Roussev, A. Asai, and T. Gombosi. Numerical Investigation of a Coronal Mass Ejection from an Anemone Active Region: Reconnection and Deflection of the 2005 August 22 Eruption. *ArXiv e-prints*, June 2011.

B. J. Lynch, S. K. Antiochos, P. J. MacNeice, T. H. Zurbuchen, and L. A. Fisk. Observable Properties of the Breakout Model for Coronal Mass Ejections. *Astrophys. J.,*, 617: 589–599, December 2004. doi: 10.1086/424564.

B. J. Lynch, S. K. Antiochos, C. R. DeVore, J. G. Luhmann, and T. H. Zurbuchen. Topological Evolution of a Fast Magnetic Breakout CME in Three Dimensions. *Astrophys. J.,*, 683:1192–1206, August 2008. doi: 10.1086/589738.

B. J. Lynch, S. K. Antiochos, Y. Li, J. G. Luhmann, and C. R. DeVore. Rotation of Coronal Mass Ejections during Eruption. *Astrophys. J.,*, 697:1918–1927, June 2009. doi: 10.1088/0004-637X/697/2/1918.

W. B. Manchester, T. I. Gombosi, I. Roussev, A. Ridley, D. L. De Zeeuw, I. V. Sokolov, K. G. Powell, and G. Tóth. Modeling a space weather event from the Sun to the Earth: CME generation and interplanetary propagation. *Journal of Geophysical Research (Space Physics)*, 109:2107–+, February 2004. doi: 10.1029/2003JA010150.

W. B. Manchester, IV, T. I. Gombosi, D. L. De Zeeuw, I. V. Sokolov, I. I. Roussev, K. G. Powell, J. Kóta, G. Tóth, and T. H. Zurbuchen. Coronal Mass Ejection Shock and Sheath Structures Relevant to Particle Acceleration. *Astrophys. J.,*, 622:1225–1239, April 2005. doi: 10.1086/427768.

W. B. Manchester, IV, A. Vourlidas, G. Tóth, N. Lugaz, I. I. Roussev, I. V. Sokolov, T. I. Gombosi, D. L. De Zeeuw, and M. Opher. Three-dimensional MHD Simulation of the 2003 October 28 Coronal Mass Ejection: Comparison with LASCO Coronagraph Observations. *Astrophys. J.,*, 684:1448–1460, September 2008. doi: 10.1086/590231.

G. Mann, F. Jansen, R. J. MacDowall, M. L. Kaiser, and R. G. Stone. A heliospheric density model and type III radio bursts. *Astron. Astrophys.,*, 348:614–620, August 1999.

G. Mann, A. Klassen, H. Aurass, and H.-T. Classen. Formation and development of shock waves in the solar corona and the near-Sun interplanetary space. *Astron. Astrophys.,*, 400:329–336, March 2003. doi: 10.1051/0004-6361:20021593.

W. H. Matthaeus, G. P. Zank, S. Oughton, D. J. Mullan, and P. Dmitruk. Coronal Heating by Magnetohydrodynamic Turbulence Driven by Reflected Low-Frequency Waves. *Astrophys. J.,*, 523:L93–L96, September 1999. doi: 10.1086/312259.

D. J. McComas, B. L. Barraclough, H. O. Funsten, J. T. Gosling, E. Santiago-Muñoz, R. M. Skoug, B. E. Goldstein, M. Neugebauer, P. Riley, and A. Balogh. Solar wind observations over Ulysses' first full polar orbit. *J. Geophys. Res.,*, 105:10419–10434, May 2000. doi: 10.1029/1999JA000383.

R. A. Mewaldt, C. M. S. Cohen, D. K. Haggerty, R. E. Gold, S. M. Krimigis, R. A. Leske, R. C. Ogliore, E. C. Roelof, E. C. Stone, T. T. von Rosenvinge, and M. E. Wiedenbeck. Heavy Ion and Electron Release Times in Solar Particle Events. In *International Cosmic Ray Conference*, volume 6 of *International Cosmic Ray Conference*, pages 3313–+, July 2003.

Z. Mikić, J. A. Linker, D. D. Schnack, R. Lionello, and A. Tarditi. Magnetohydrodynamic modeling of the global solar corona. *Physics of Plasmas*, 6:2217–2224, May 1999. doi: 10.1063/1.873474.

R. L. Moore, S. T. Suess, Z. E. Musielak, and C.-H. An. Alfven wave trapping, network microflaring, and heating in solar coronal holes. *Astrophys. J.,*, 378:347–359, September 1991. doi: 10.1086/170435.

C. Möstl, C. J. Farrugia, M. Temmer, C. Miklenic, A. M. Veronig, A. B. Galvin, M. Leitner, and H. K. Biernat. Linking Remote Imagery of a Coronal Mass Ejection to Its In Situ Signatures at 1 AU. *Astrophys. J.,*, 705:L180–L185, November 2009. doi: 10.1088/0004-637X/705/2/L180.

U. Narain and R. K. Sharma. Nonlinear Viscous Damping of Surface AlfvÉn Waves in Polar Coronal Holes. *Solar Phys.,*, 181:287–287, August 1998.

U. Narain and P. Ulmschneider. Chromospheric and Coronal Heating Mechanisms II. *Space Sci. Rev.,*, 75:453–509, February 1996. doi: 10.1007/BF00833341.

M. Neugebauer and C. W. Snyder. Solar Plasma Experiment. *Science*, 138:1095–1097, December 1962. doi: 10.1126/science.138.3545.1095-a.

G. Newkirk, Jr. The Solar Corona in Active Regions and the Thermal Origin of the Slowly Varying Component of Solar Radio Radiation. *Astrophys. J.,*, 133:983–+, May 1961. doi: 10.1086/147104.

L. Ofman. Three-fluid model of the heating and acceleration of the fast solar wind. *Journal of Geophysical Research (Space Physics)*, 109:7102–+, July 2004. doi: 10.1029/2003JA010221.

L. Ofman. Wave Modeling of the Solar Wind. *Living Reviews in Solar Physics*, 7:4–+, October 2010.

L. Ofman and J. M. Davila. Solar wind acceleration by large-amplitude nonlinear waves: Parametric study. *J. Geophys. Res.,*, 103:23677–23690, October 1998. doi: 10.1029/98JA01996.

T. J. Okamoto, S. Tsuneta, T. E. Berger, K. Ichimoto, Y. Katsukawa, B. W. Lites, S. Nagata, K. Shibata, T. Shimizu, R. A. Shine, Y. Suematsu, T. D. Tarbell, and A. M. Title. Coronal Transverse Magnetohydrodynamic Waves in a Solar Prominence. *Science*, 318: 1577–, December 2007. doi: 10.1126/science.1145447.

V. Ontiveros and A. Vourlidas. Quantitative Measurements of Coronal Mass Ejection-Driven Shocks from LASCO Observations. *Astrophys. J.,*, 693:267–275, March 2009. doi: 10.1088/0004-637X/693/1/267.

M. Opher. *Shocks in heliophysics*, pages 193–+. Cambridge University Press, 2010.

M. Opher, E. C. Stone, and T. I. Gombosi. The Orientation of the Local Interstellar Magnetic Field. *Science*, 316:875–, May 2007. doi: 10.1126/science.1139480.

M. Opher, F. Alouani Bibi, G. Toth, J. D. Richardson, V. V. Izmodenov, and T. I. Gombosi.

A strong, highly-tilted interstellar magnetic field near the solar system. *Nature*, 462:1039, 2009.

R. Oran, I. V. Sokolov, I. I. Roussev, B. van der Holst, W. B. Manchester, and T. I. Gombosi. 4D Model for the Solar Environment. In N. V. Pogorelov, E. Audit, & G. P. Zank, editor, *Numerical Modeling of Space Plasma Flows, Astronum-2009*, volume 429 of *Astronomical Society of the Pacific Conference Series*, pages 207–+, September 2010.

M. Owens and P. Cargill. Non-radial solar wind flows induced by the motion of interplanetary coronal mass ejections. *Annales Geophysicae*, 22:4397–4406, December 2004.

E. N. Parker. Dynamics of the Interplanetary Gas and Magnetic Fields. *Astrophys. J.,*, 128:664–+, November 1958. doi: 10.1086/146579.

E. N. Parker. *Interplanetary dynamical processes.* 1963.

E. N. Parker. Dynamical Theory of the Solar Wind. *Space Sci. Rev.,*, 4:666–708, September 1965. doi: 10.1007/BF00216273.

E. N. Parker. Nanoflares and the solar X-ray corona. *Astrophys. J.,*, 330:474–479, July 1988. doi: 10.1086/166485.

E. N. Parker. The phase mixing of Alfven waves, coordinated modes, and coronal heating. *Astrophys. J.,*, 376:355–363, July 1991. doi: 10.1086/170285.

G. W. Pneuman and R. A. Kopp. Gas-Magnetic Field Interactions in the Solar Corona. *Solar Phys.,*, 18:258–270, June 1971. doi: 10.1007/BF00145940.

W. Poomvises, J. Zhang, and O. Olmedo. Coronal Mass Ejection Propagation and Expansion in Three-dimensional Space in the Heliosphere Based on Stereo/SECCHI Observations. *Astrophys. J.,*, 717:L159–L163, July 2010. doi: 10.1088/2041-8205/717/2/L159.

A. F. Rappazzo, M. Velli, G. Einaudi, and R. B. Dahlburg. Coronal Heating, Weak MHD Turbulence, and Scaling Laws. *Astrophys. J.,*, 657:L47–L51, March 2007. doi: 10.1086/512975.

P. Riley, R. Lionello, J. A. Linker, Z. Mikic, J. Luhmann, and J. Wijaya. Global MHD Modeling of the Solar Corona and Inner Heliosphere for the Whole Heliosphere Interval. *Solar Phys.,*, pages 13–+, February 2011. doi: 10.1007/s11207-010-9698-x.

E. Robbrecht, S. Patsourakos, and A. Vourlidas. No Trace Left Behind: STEREO Observation of a Coronal Mass Ejection Without Low Coronal Signatures. *Astrophys. J.,*, 701: 283–291, August 2009. doi: 10.1088/0004-637X/701/1/283.

I. I. Roussev, T. I. Gombosi, I. V. Sokolov, M. Velli, W. Manchester, IV, D. L. DeZeeuw, P. Liewer, G. Tóth, and J. Luhmann. A Three-dimensional Model of the Solar Wind Incorporating Solar Magnetogram Observations. *Astrophys. J.,*, 595:L57–L61, September 2003. doi: 10.1086/378878.

I. I. Roussev, T. G. Forbes, T. I. Gombosi, I. V. Sokolov, D. L. DeZeeuw, and J. Birn. A Three-dimensional Flux Rope Model for Coronal Mass Ejections Based on a Loss of Equilibrium. *Astrophys. J.,*, 588:L45–L48, May 2003b. doi: 10.1086/375442.

I. I. Roussev, I. V. Sokolov, T. G. Forbes, T. I. Gombosi, M. A. Lee, and J. I. Sakai. A Numerical Model of a Coronal Mass Ejection: Shock Development with Implications for the Acceleration of GeV Protons. *Astrophys. J.,*, 605:L73–L76, April 2004. doi: 10.1086/392504.

M. S. Ruderman. Nonlinear dissipation of surface Alfven waves in the solar corona. *Astrophys. J.,*, 399:724–732, November 1992. doi: 10.1086/171965.

M. S. Ruderman, M. L. Goldstein, D. A. Roberts, A. Deane, and L. Ofman. Alfvén wave phase mixing driven by velocity shear in two-dimensional open magnetic configurations. *J. Geophys. Res.,*, 104:17057–17068, August 1999. doi: 10.1029/1999JA900144.

J.-I. Sakai, A. Takahata, and I. V. Sokolov. Heating of Coronal Loop Footpoints by Magnetic Reconnection Resulting from Surface Alfvén Waves and Colliding Plasma Flows in Chromospheric Current Sheets. *Astrophys. J.,*, 556:905–911, August 2001. doi: 10.1086/321622.

N. A. Schwadron, L. Townsend, K. Kozarev, M. A. Dayeh, F. Cucinotta, M. Desai, M. Golightly, D. Hassler, R. Hatcher, M.-Y. Kim, A. Posner, M. PourArsalan, H. E. Spence, and R. K. Squier. Earth-Moon-Mars Radiation Environment Module framework. *Space Weather*, 8:S00E02, January 2010. doi: 10.1029/2009SW000523.

N. R. Sheeley, Jr., R. A. Howard, D. J. Michels, M. J. Koomen, R. Schwenn, K. H. Muehlhaeuser, and H. Rosenbauer. Coronal mass ejections and interplanetary shocks. *J. Geophys. Res.,*, 90:163–175, January 1985. doi: 10.1029/JA090iA01p00163.

D. Shiota, K. Kusano, T. Miyoshi, and K. Shibata. Magnetohydrodynamic Modeling for a Formation Process of Coronal Mass Ejections: Interaction Between an Ejecting Flux Rope and an Ambient Field. *Astrophys. J.,*, 718:1305–1314, August 2010. doi: 10.1088/0004-637X/718/2/1305.

G. Siscoe and D. Odstrcil. Ways in which ICME sheaths differ from magnetosheaths. *Journal of Geophysical Research (Space Physics)*, 113:A00B07, December 2008. doi: 10.1029/2008JA013142.

E. C. Sittler, Jr. and M. Guhathakurta. Semiempirical Two-dimensional MagnetoHydrodynamic Model of the Solar Corona and Interplanetary Medium. *Astrophys. J.,*, 523: 812–826, October 1999. doi: 10.1086/307742.

I. V. Sokolov, I. I. Roussev, M. Skender, T. I. Gombosi, and A. V. Usmanov. Transport Equation for MHD Turbulence: Application to Particle Acceleration at Interplanetary Shocks. *Astrophys. J.,*, 696:261–267, May 2009. doi: 10.1088/0004-637X/696/1/261.

A. C. Sterling, H. S. Hudson, B. J. Thompson, and D. M. Zarro. Yohkoh SXT and SOHO EIT Observations of Sigmoid-to-Arcade Evolution of Structures Associated with Halo Coronal Mass Ejections. *Astrophys. J.,*, 532:628–647, March 2000. doi: 10.1086/308554.

E. C. Stone. The Heliosheath and Interstellar Medium: What the Voyagers Can Tell Us (Invited). *AGU Fall Meeting Abstracts*, pages A1+, December 2010.

E. C. Stone, A. C. Cummings, F. B. McDonald, B. C. Heikkila, N. Lal, and W. R. Webber. Voyager 1 Explores the Termination Shock Region and the Heliosheath Beyond. *Science*, 309:2017–2020, September 2005. doi: 10.1126/science.1117684.

E. C. Stone, A. C. Cummings, F. B. McDonald, B. C. Heikkila, N. Lal, and W. R. Webber. An asymmetric solar wind termination shock. *Nature,*, 454:71–74, July 2008. doi: 10.1038/nature07022.

T. K. Suzuki and S.-i. Inutsuka. Solar winds driven by nonlinear low-frequency Alfvén waves from the photosphere: Parametric study for fast/slow winds and disappearance of solar winds. *Journal of Geophysical Research (Space Physics)*, 111:6101–+, June 2006. doi: 10.1029/2005JA011502.

J. Terradas, M. Goossens, and G. Verth. Selective spatial damping of propagating kink waves due to resonant absorption. *Astron. Astrophys.,*, 524:A23+, December 2010. doi: 10.1051/0004-6361/201014845.

B. J. Thompson, S. P. Plunkett, J. B. Gurman, J. S. Newmark, O. C. St. Cyr, and D. J. Michels. SOHO/EIT observations of an Earth-directed coronal mass ejection on May 12, 1997. *Geophys. Res. Lett.,*, 25:2465–2468, 1998. doi: 10.1029/98GL50429.

V. S. Titov and P. Démoulin. Basic topology of twisted magnetic configurations in solar flares. *Astron. Astrophys.,*, 351:707–720, November 1999.

S. Tomczyk and S. W. McIntosh. Time-Distance Seismology of the Solar Corona with CoMP. *Astrophys. J.,*, 697:1384–1391, June 2009. doi: 10.1088/0004-637X/697/2/1384.

S. Tomczyk, S. W. McIntosh, S. L. Keil, P. G. Judge, T. Schad, D. H. Seeley, and J. Edmondson. Alfvén Waves in the Solar Corona. *Science*, 317:1192–, August 2007. doi: 10.1126/science.1143304.

Gabor Toth, Bart van der Holst, Igor V. Sokolov, Darren L. De Zeeuw, Tamas I. Gombosi, Fang Fang, Ward B. Manchester, Xing Meng, Dalal Najib, Kenneth G. Powell, Quentin F.

Stout, Alex Glocer, Ying-Juan Ma, and Merav Opher. Adaptive numerical algorithms in space weather modeling. *Journal of Computational Physics*, In Press, Corrected Proof:–, 2011. ISSN 0021-9991. doi: DOI: 10.1016/j.jcp.2011.02.006.

T. L. Totten, J. W. Freeman, and S. Arya. An empirical determination of the polytropic index for the free-streaming solar wind using HELIOS 1 data. *J. Geophys. Res.,*, 100: 13–17, January 1995. doi: 10.1029/94JA02420.

C.-Y. Tu, E. Marsch, and H. Rosenbauer. The dependence of MHD turbulence spectra on the inner solar wind stream structure near solar minimum. *Geophys. Res. Lett.,*, 17: 283–286, March 1990. doi: 10.1029/GL017i003p00283.

A. J. Tylka, C. M. S. Cohen, W. F. Dietrich, S. Krucker, R. E. McGuire, R. A. Mewaldt, C. K. Ng, D. V. Reames, and G. H. Share. Onsets and Release Times in Solar Particle Events. In *International Cosmic Ray Conference*, volume 6 of *International Cosmic Ray Conference*, pages 3305–+, July 2003.

A. J. Tylka, C. M. S. Cohen, W. F. Dietrich, M. A. Lee, C. G. Maclennan, R. A. Mewaldt, C. K. Ng, and D. V. Reames. Shock Geometry, Seed Populations, and the Origin of Variable Elemental Composition at High Energies in Large Gradual Solar Particle Events. *Astrophys. J.,*, 625:474–495, May 2005. doi: 10.1086/429384.

A. V. Usmanov and M. L. Goldstein. A tilted-dipole MHD model of the solar corona and solar wind. *Journal of Geophysical Research (Space Physics)*, 108:1354–+, September 2003. doi: 10.1029/2002JA009777.

A. V. Usmanov and M. L. Goldstein. A three-dimensional MHD solar wind model with pickup protons. *Journal of Geophysical Research (Space Physics)*, 111:7101–+, July 2006. doi: 10.1029/2005JA011533.

A. V. Usmanov, W. H. Matthaeus, B. A. Breech, and M. L. Goldstein. Solar Wind Modeling with Turbulence Transport and Heating. *Astrophys. J.,*, 727:84–+, February 2011. doi: 10.1088/0004-637X/727/2/84.

B. van der Holst, W. B. Manchester, IV, R. A. Frazin, A. M. Vásquez, G. Tóth, and T. I. Gombosi. A Data-driven, Two-temperature Solar Wind Model with Alfvén Waves. *Astrophys. J.,*, 725:1373–1383, December 2010. doi: 10.1088/0004-637X/725/1/1373.

A. M. Vásquez, R. A. Frazin, and W. B. Manchester. The Solar Minimum Corona from Differential Emission Measure Tomography. *Astrophys. J.,*, 715:1352–1365, June 2010. doi: 10.1088/0004-637X/715/2/1352.

A. M. Vásquez, Z. Huang, W. B. Manchester, and R. A. Frazin. The WHI Corona from Differential Emission Measure Tomography. *Solar Phys.,*, pages 16–+, February 2011. doi: 10.1007/s11207-010-9706-1.

M. Velli. Alfven waves in the solar corona and solar wind. *Advances in Space Research*, 14: 123–, April 1994. doi: 10.1016/0273-1177(94)90171-6.

A. Verdini and M. Velli. Alfvén Waves and Turbulence in the Solar Atmosphere and Solar Wind. *Astrophys. J.,*, 662:669–676, June 2007. doi: 10.1086/510710.

G. Verth, J. Terradas, and M. Goossens. Observational Evidence of Resonantly Damped Propagating Kink Waves in the Solar Corona. *Astrophys. J.,*, 718:L102–L105, August 2010. doi: 10.1088/2041-8205/718/2/L102.

A. Vourlidas, S. T. Wu, A. H. Wang, P. Subramanian, and R. A. Howard. Direct Detection of a Coronal Mass Ejection-Associated Shock in Large Angle and Spectrometric Coronagraph Experiment White-Light Images. *Astrophys. J.,*, 598:1392–1402, December 2003. doi: 10.1086/379098.

A. Vourlidas, R. A. Howard, E. Esfandiari, S. Patsourakos, S. Yashiro, and G. Michalek. Comprehensive Analysis of Coronal Mass Ejection Mass and Energy Properties Over a Full Solar Cycle. *Astrophys. J.,*, 722:1522–1538, October 2010. doi: 10.1088/0004-637X/722/2/1522.

A. Vourlidas, R. Colaninno, T. Nieves-Chinchilla, and G. Stenborg. The First Observation of a Rapidly Rotating Coronal Mass Ejection in the Middle Corona. *Astrophys. J.,*, 733: L23+, June 2011. doi: 10.1088/2041-8205/733/2/L23.

Y. Wang and J. Zhang. A Statistical Study of Solar Active Regions That Produce Extremely Fast Coronal Mass Ejections. *Astrophys. J.,*, 680:1516–1522, June 2008. doi: 10.1086/587619.

D. G. Wentzel. Hydromagnetic surface waves. *Astrophys. J.,*, 227:319–322, January 1979. doi: 10.1086/156732.

D. G. Wentzel. Magnetohydrodynamic wave conversion and solar-wind acceleration in coronal holes. *Astrophys. J.,*, 336:1073–1077, January 1989. doi: 10.1086/167076.

B. E. Wood and R. A. Howard. An Empirical Reconstruction of the 2008 April 26 Coronal Mass Ejection. *Astrophys. J.,*, 702:901–910, September 2009. doi: 10.1088/0004-637X/702/2/901.

S. Yao, E. Marsch, C.-Y. Tu, and R. Schwenn. Identification of prominence ejecta by the proton distribution function and magnetic fine structure in interplanetary coronal mass ejections in the inner heliosphere. *Journal of Geophysical Research (Space Physics)*, 115: A05103, May 2010. doi: 10.1029/2009JA014914.

S. Yashiro, N. Gopalswamy, G. Michalek, O. C. St. Cyr, S. P. Plunkett, N. B. Rich, and R. A. Howard. A catalog of white light coronal mass ejections observed by the SOHO spacecraft. *Journal of Geophysical Research (Space Physics)*, 109:A07105, July 2004. doi: 10.1029/2003JA010282.

V. Yurchyshyn, Q. Hu, R. P. Lepping, B. J. Lynch, and J. Krall. Orientations of LASCO Halo CMEs and their connection to the flux rope structure of interplanetary CMEs. *Advances in Space Research*, 40:1821–1826, 2007. doi: 10.1016/j.asr.2007.01.059.

L. Zangrilli, P. Nicolosi, G. Poletto, G. Noci, M. Romoli, and J. L. Kohl. Latitudinal properties of the Lyman alpha and O VI profiles in the extended solar corona. *Astron. Astrophys.*,, 342:592–600, February 1999.

J. Zhang and K. P. Dere. A Statistical Study of Main and Residual Accelerations of Coronal Mass Ejections. *Astrophys. J.*,, 649:1100–1109, October 2006. doi: 10.1086/506903.

J. Zhang, I. G. Richardson, D. F. Webb, N. Gopalswamy, E. Huttunen, J. C. Kasper, N. V. Nitta, W. Poomvises, B. J. Thompson, C.-C. Wu, S. Yashiro, and A. N. Zhukov. Solar and interplanetary sources of major geomagnetic storms (Dst less than -100 nT) during 1996-2005. *Journal of Geophysical Research (Space Physics)*, 112:A10102, October 2007. doi: 10.1029/2007JA012321.

X. P. Zhao and J. T. Hoeksema. Central axial field direction in magnetic clouds and its relation to southward interplanetary magnetic field events and dependence on disappearing solar filaments. *J. Geophys. Res.*,, 103:2077–+, February 1998. doi: 10.1029/97JA03234.

Curriculum Vitae

Rebekah Minnel Evans Frolov
George Mason University, Physics and Astronomy Department
4400 University Drive, MSN 3F3, Fairfax, VA 22030
revansa@masonlive.gmu.edu

Education

MS, Applied Physics and Engineering George Mason University, 2008
BS, Physics with a concentration in Astrophysics University of Delaware, 2006

Academic Positions

Graduate Teaching Assistant George Mason University Aug. 2006 May 2007
Graduate Research Assistant George Mason University Aug. 2006 Jan 2011
Research Fellow Boston University, Jan-Aug. 2011
NASA Postdoctoral Fellow (ORAU) Goddard Space Flight Center, Sept 2011

Refereed Journal Publications

1. Evans, R. M., Opher, M., Manchester, W. B., IV and Gombosi, T. I. Alfvn Profile in the Lower Corona: Implications for Shock Formation. 2008, The Astrophysical Journal, Vol. 687
2. Evans, R. M., Opher, M., Jatenco-Pereira, V. and Gombosi, T. I. Surface Alfvn Wave Damping in a Three-Dimensional Simulation of the Solar Wind. 2009, The Astrophysical Journal, Vol . 703
3. Evans, R. M., Opher, M. and Gombosi, T. I. Learning from the Outer Heliosphere: Interplanetary Coronal Mass Ejection Sheath Flows and the Ejecta Orientation in the Lower Corona 2011, The Astrophysical Journal, Vol. 728
4. Das, I., Opher, M., Evans, R. M. and Gombosi, T. I. Pile-up Compression in the Evolution of CMEs in the Lower Corona. 2011, The Astrophysical Journal, Vol. 729
5. Loesch, C., Opher, M., Alves, M., Evans, R. M. and Manchester, W. B., IV. Signatures of Two Distinct Driving Mechanisms in the Evolution of CMEs in the Lower Corona., 2011, Journal of Geophysical Research, Vol. 116, A04106

Presentations

1. Evans. R. M. Alfvn Profile in the Lower Corona. Space Sciences Seminar, George Mason University, Nov. 2007
2. Evans, R. M., Opher, M., Manchester, W. B., IV, Velli, M. and Gombosi, T. I. Alfvn Profile in the Lower Corona: Implications for Shock Formation. Poster, Fall AGU Meeting, Dec. 2007
3. Evans, R. M., Opher, M., Manchester, W. B., IV, and Gombosi, T. I. Alfvn Profile in the Lower Corona: Implications for Shock Formation. Poster, SHINE Conference, Aug. 2008
4. Evans, R. M. Research in Space Weather. Invited, Physics Department Seminar, James Madison University, Sept. 2008

5. Evans, R. M., Opher, M., Jatenco-Pereira, V. and Gombosi, T. I. Surface Alfvn Wave Damping. Poster, NRL/GMU Research Conference, Oct. 2008

6. Evans, R. M., Opher, M., Jatenco-Pereira, V. and Gombosi, T. I. Surface Alfvn Wave Damping. Poster, AGU Chapman Conference on Universal Processes, Nov. 2008

7. Evans, R. M., Opher, M., Jatenco-Pereira, V. and Gombosi, T. I. Surface Alfvn Wave Damping in a 3D Simulation of the Solar Wind. Poster, Fall AGU Meeting, Dec. 2008

8. Evans, R. M. Space Weather Modeling. Student Day Tutorial, SHINE Conference, July 2009

9. Evans, R. M., Opher, M., Jatenco-Pereira, V. and Gombosi, T. I. Surface Alfvn Wave Damping in a 3D Simulation of the Solar Wind. Poster, SHINE Conference, July 2009

10. Evans, R. M., Opher, M., Kuznetsova, M. M. and Gombosi, T. I. Multiscale Modeling of Reconnection: Effect on CME Dynamics. Poster, SHINE Conference, July 2009

11. Evans, R. M., Opher, M., Oran, R. and Sokolov, I. V. Surface Alfvn Wave Damping in a Solar Wind Simulation Driven by Alfven Waves. Poster, Fall AGU Meeting, Dec. 2009

12. Evans, R. M., Opher, M. and Gombosi, T. I. Relationship between Flow and Magnetic Field in Coronal Mass Ejections. Oral Presentation, AAS Winter Meeting, Jan. 2010

13. Evans, R. M., Opher, M., Oran, R., Sokolov, I. V. and van der Holst, B. Surface Alfvn Wave Contribution to Coronal Heating in a Wave-Driven Solar Wind Model. Poster, Spring SPD Meeting, May 2010

14. Opher, M. and Evans, R. M. Sheath Flows and Reconnection in the Lower Corona: New Diagnostics for the Initial Orientation of the Ejecta of Coronal Mass Ejections. Poster, Spring SPD Meeting, May 2010

15. Evans, R. M., Opher, M., Oran, R., van der Holst, B. and Sokolov, I. V. Surface Alfvn Wave Contribution to Coronal Heating in a Wave-Driven Solar Wind Model. Poster and Oral Presentation, SHINE Conference, July 2010

16. Evans, R. M., Opher, M. and Zhang, J. Prediction of Secondary Acceleration of Coronal Mass Ejections due to Reconnection of the Flux Rope with the Overlying Coronal Field. Oral Presentation (Given by M. Opher), Spring AGU Meeting, Aug. 2010

17. Evans, R. M., Opher, M., Jatenco-Pereira, V. and Gombosi, T. I. Damping of Surface Alfvn Waves in a 3D Simulation of the Solar Wind Poster Presentation (given by V. Jatenco-Pereira), Cool Stars 16 Meeting, Sept. 2010

18. Evans, R. M., Opher, M., van der Holst, B., Oran, R., Sokolov, I. V, Frazin, R Gombosi, T. I. Coronal Heating by Surface Alfven Wave Damping: Implementation in MHD Modeling and Connection to Observations Oral Presentation, Fall AGU Meeting, Dec. 2010

Workshops and Schools

International School for Space Simulations (ISSS-8), Feb. 2007
University of Arizonas Solar Physics Summer School, June 2007
STEREO SECCHI Workshop, NRL, Nov. 2008
EMMREM-CRaTER Workshop, University of New Hampshire, August 2010

Leadership

Student Representative, AGU Space Physics Aeronomy (SPA) (2007-2010)
Student Representative, SHINE Conference (2009-2011)
President, University of Delaware Society of Physics Students (2005-2006)

Teaching Experience

Recitation Instructor for University Physics I and II, College Physics II and Undergraduate Thermodynamics (PHYS 243, 245, 260 and 262) - Excellence in teaching ranking, 2007
Fill-in lecturer for Introduction to Astronomy (Spring 2007); Electromagnetic Theory (Fall 2008 2010)
Professional Society Memberships
American Geophysical Union
Solar Physics Division of the American Astronomical Society